TRACING THE SOLAR WIND TO ITS ORIGIN: NEW INSIGHTS FROM ACE/SWICS DATA AND SO/HIS PERFORMANCE PREDICTIONS

By

Mark Stakhiv

A dissertation submitted in partial fulfillment
of the requirements of the degree of
Doctor of Philosophy
(Atmospheric, Oceanic, and Space Sciences)
in the University of Michigan
2016

Doctoral Committee:

Professor Susan T. Lepri, Co-Chair
Professor Enrico Landi, Co-Chair
Professor Zhong He
Research Scientist Jim M. Raines

ACKNOWLEDGEMENTS

There are a large number of people who deserve recognition and I would like to thank for supporting me in the PhD process. I would like to thank everyone who gave me wisdom, hope, advice, and friendship. The road to a PhD is long and requires the support of countless individuals.

First, and foremost, I would like to thank my advisors, Susan Lepri and Enrico Landi. Their guidance, wisdom, and patience provided me with the right environment to succeed. I would also like to thank the rest of my committee, Jim Raines and Zhong He, who helped shape this thesis into what it is today.

Second, I would like to thank Jim Raines for his mentorship. I appreciate all of the long talks over the years, and the great life advice that was given. Your constant support and presence allowed me to grow as a student and a scientist.

Third, I would like to thank my fellow student (and current Doctor) Aleida Higginson. Five years ago we came into this research group and struggled together through classes (most notably Jackson physics) and quals. The endless hours of studying forged a friendship that cannot be broken. I would also like to thank the former and current students of the Solar and Heliophysics Research Group for being incredible officemates and good friends (Jacob Gruesbeck, Dan Gershman, Gina DiBraccio, Micah Weberg, Pat Tracy, Manan Kochler). I would like to acknowledge the rest of the Solar and Heliophysics Research Group who were invaluable resources (Len Fisk, Justin Kasper, Jason Gilbert, Jon Thomas, Thomas Zurbuchen, Liang Zhao) and often provided me with sound science (and life) advice.

Finally, I would like to thank my family (Mira Stakhiv, Jerry Stakhiv, Daniel Stakhiv, and Stephen Stakhiv) who from a very young age instilled in me a curiosity which drove me to learn. I would also like to thank my girlfriend Diana Thatcher who put up with all of the long nights and always encouraged me to keep going.

TABLE OF CONTENTS

LIST OF FIGURES

LIST OF TABLES

LIST OF ACRONYMS

ACE	Advance Composition Explorer
AU	Astronomical Unit
AWSoM	Alfvén Wave Solar Model
CIR	Co-rotating Interaction Region
CME	Coronal Mass Ejection
CS	Current Sheet
DOY	Day of Year
EA-IS	Electrostatic Analyzer with Ion Steering
E/q	Energy per Charge
ESA	Electrostatic Analyzer
FIP	First Ionization Potential
FWHM	Full Width Half Maximum
HCS	Heliospheric Current Sheet
HIS	Heavy Ion Sensor
ICME	Interplanetary Coronal Mass Ejection
IMF	Interplanetary Magnetic Field
L1	First Lagrangian Point
MCP	Microchannel Plate
NASA	National Aeronautics and Space Administration
SEP	Solar Energetic Particles
SSD	Solid State Detector
SI	Stream Interface
SIR	Stream Interaction Region
SO	Solar Orbiter
STD	Standard Deviation
SWEPAM	Solar Wind Electron, Proton, and Alpha Monitor
SWICS	Solar Wind Ion Composition Spectrometer
SWOOPS	Solar Wind Observations Over the Poles of the Sun
TOF	Time of Flight
VHM	Vector Helium Magnetometer

ABSTRACT

Tracing the Solar Wind to its Origin: New Insights from ACE/SWICS Data and SO/HIS Performance Predictions

by

Mark Stakhiv

Co-Chairs: Susan T. Lepri and Enrico Landi

The solar wind is a hot tenuous plasma that continuously streams off of the Sun into the heliosphere. The solar wind is the medium through which coronal mass ejections (CMEs) travel from the Sun to the Earth, where they can disrupt vital space-based technologies and wreak havoc on terrestrial infrastructure. Understanding the solar wind can lead to improved predications of CME arrival time as well as their geoeffectiveness. The solar wind is studied in this thesis through in situ measurements of heavy ions. Several outstanding questions about the solar wind are addressed in this thesis: What is the origin of the solar wind? How is the solar wind heated and accelerated?

The charge state distribution and abundance of heavy ions in the solar wind record information about their source location and heating mechanism. This information is largely unchanged from the Sun to the Earth, where it is collected in situ with spacecraft. In this thesis we use data from the Solar Wind Ion Composition Spectrometer (SWICS) that flew on two spacecraft: Ulysses (1990 - 2009) and ACE (1998 - present). We analyze the kinetic and compositional properties of the solar wind with heavy ion data and lay out a unified wind scenario, which states that the solar wind originates from two different sources and regardless of its release mechanism the solar wind is then accelerated by waves. The data from these instruments are the best available to date but still lack the measurement cadence and distribution resolution to fully answer all of the solar wind questions. To address these issues a new heavy ion sensor is being developed to be the next generation of in situ heavy ion measurements. This thesis supports the development of this instrument through the analysis of the sensors measurement properties and the characterization of its geometric factor and efficiencies.

CHAPTER I

Introduction and Scientific Background

1.1. Brief Introduction to the Solar Wind

The solar wind is a hot tenuous plasma streaming off of the Sun into the heliosphere. Studying and understanding the solar wind is critical for two main reasons. First, the solar wind fills the heliosphere, influencing planets and all other solar system bodies. It is the medium through which coronal mass ejections (CMEs) are carried to the far reaches of the solar system, where the CMEs can interact with planetary magnetospheres. When conditions are right, CMEs can interact with the Earth's magnetosphere; compressing it, injecting highly energetic particles into it, and inducing currents in the ionosphere and on the ground. The CMEs can then disrupt vital space-based technologies utilized for things such as global positioning and communication. Furthermore, if a CME is strong enough it can wreak havoc on terrestrial infrastructure with the currents that are induced, e.g., disrupting electrical power grids, potentially causing billions of dollars in damage. Developing a more complete understanding of the solar wind, both of its origin and acceleration, will allow us to improve arrival time prediction of CMEs, as well as their geoeffectiveness. The second reason why solar wind research is important is because it allows us to study space plasma in situ, in great detail, in a unique environment that cannot be recreated in the laboratory due to the scales and densities involved. Understanding the physical processes occurring in the highly dynamic, magnetized, very low density solar wind plasma can lead to breakthroughs in understanding the nuances of plasma physics and lead to the development of new technologies. Despite decades of intensive research and the launch of numerous spacecraft missions, we are still unable to answer the two most basic and fundamental questions about the solar wind: What is the source region of the solar wind? How is it heated and accelerated? These questions form the basis of the motivations for this thesis.

1.1.1. Solar wind history

The solar wind was first theorized in the late 19th century when it was observed that there were fluctuation in the Earth's magnetic field and a brightening of the aurora that coincided with features on the Sun. The theory of the solar wind was confirmed years later when direct evidence of its existence was provided by Ludwig Biermann (1951). Biermann observed that a nearby comet had two tails, one of which was always pointing away from the Sun. He concluded that this tail was being pushed by "corpuscular radiation" which later became known as the solar wind. From here numerous theories and models were developed to explain how this solar wind was occurring and what its properties were. The two leading competing theories that existed were a slow stationary extension of the solar corona by Sydney Chapman (1957) and a fast solar wind by Eugene Parker (1958). Parker proposed that the solar wind pressure in the corona causes it to extend into the heliosphere. He then showed that in order to have the pressure at infinity match the interstellar medium's pressure, the solar wind needs to be accelerated to supersonic speeds. In the end, Parker's theory that the solar wind was not only moving away from the Sun, but doing so at supersonic speeds was proven by observations from the Mariner 2 spacecraft in 1962 (Neugebauer & Snyder 1962). Following this discovery many spacecraft missions were developed to study the origin and acceleration of the solar wind.

1.1.2. Solar wind classification

The solar wind is typically classified into two subsets: the fast solar wind and the slow solar wind. Traditionally the fast solar wind is described as the solar wind with a velocity greater than 500 km s^{-1}, and the slow solar wind as the wind with a velocity less than 500 km s^{-1} (Schwenn & Marsch 1990). Aside from the velocity of the solar wind, there are many other properties that are different between these two types of solar wind. Table 1 lists general differences that have been discovered between the two types of solar wind. The fast solar wind is cooler, having lower electron temperatures at the source (Geiss et al. 1995), occurs at higher latitudes (Schwenn & Marsch 1990), and has a composition that matches observed photospheric values (von Steiger et al. 2000). The source of the fast solar wind is generally accepted to be from coronal holes (Krieger et al. 1973). The slow solar wind is hotter, having higher electron temperatures at the source (von Steiger et al. 1997), concentrated at lower latitudes (Zhao et al. 2009), and has a highly variable and metal rich composition (Zurbuchen et al. 2006). The source of the slow solar wind is still debated and forms a central theme of this thesis (see section 1.3 for further discussion).

Table 1.1: Basic Solar Wind Properties

	Fast Solar Wind	**Slow Solar Wind**
Speed	~700-800 km/s	~250-500 km/s
Temperature at source	<1 MK	> 1.2 MK
Composition	Observed Photospheric Values	Highly Variable and Metal Rich
Location during Solar Minimum	Higher Latitudes: >30° N/S	Lower Latitudes: <30° N/S
Origin	Coronal Holes	Debated – See section 1.3

1.2. Basic Properties of the Solar Wind

The solar wind is made up of H^+ (95-98%), He^{2+} (2-5%), and other heavy ions (1%). The bulk properties (e.g., density, velocity) of the solar wind are largely governed by protons due to their abundance. The solar wind is also composed of an equal amount of electrons and ions, creating a quasi-neutral plasma. The Sun generates a strong magnetic field that is pulled into the heliosphere along with the solar wind (Parker 1958). Due to its conductivity, the solar wind is bound to the solar magnetic field because it is a frozen-in flux (Alfvén 1950). The base of the magnetic field, which is tied to the Sun, then rotates with the Sun creating the spiral magnetic field configuration in the heliosphere as seen in Figure 1.1. This spiral pattern was predicted by Parker (1958).

The Sun can be divided into two magnetic regions: an open magnetic field region and closed magnetic loops. In the open magnetic field region, concentrated in coronal holes, the magnetic field extends into the heliosphere. The closed field region has magnetic loops that close back on the Sun and only extend a few solar radii away from the sun. The largest of those closed loops is known as the streamer belt and the top of these loops are located at the base of the heliospheric current sheet, which is the boundary between the outward directed magnetic field and the inward directed magnetic field in the heliosphere. Figure 1.2 shows a simplified picture of the magnetic structure of the Sun observed from the side.

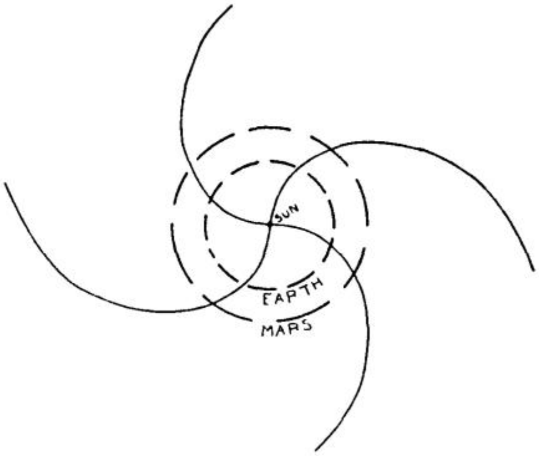

Figure 1.1: From Parker 1958. The original parker spiral configuration of the magnetic field as predicted by Eugene Parker.

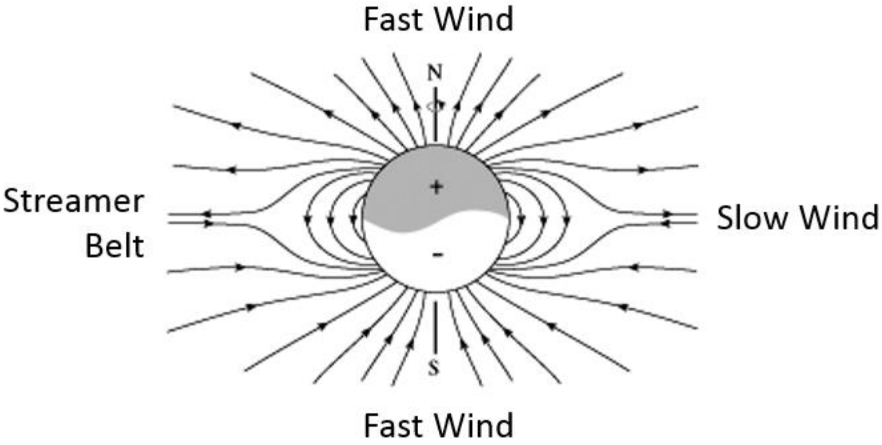

Figure 1.2: Diagram showing the magnetic configuration of the solar magnetic field. In this figure we can see magnetic loops near the equator and open magnetic field lines at the poles. From Dr. Lang, Tufts University (https://ase.tufts.edu/cosmos/view_picture.asp?id=101)

1.2.1. Heavy ions

One of the main focuses of this dissertation is the behavior of heavy ions in the solar wind and how their properties relate to its origin and heating. Although heavy ions compose only a small portion of the solar wind, their unique properties provide us with a way to probe the state of the plasma in the solar corona. As atoms and ions of heavy elements travel from the relatively cool photosphere (~5700 K, where they are mostly neutral) to the chromosphere they encounter higher temperatures (~10^4 K) where they undergo ionization and recombination.

Above the chromosphere, the plasma then enters the corona, where the temperature increases by orders of magnitude (to ~10^6 K) over a very small height (compared to the size of the chromosphere; less than 100 km thick – Lang 2006), in what is known as the transition region. In the hot corona the plasma undergoes ionization and recombination, with rates depending on the conditions in the local environment following eq. 1.1.

$$\frac{\delta y_m}{\delta t} = n_e \left(y_{m-1} C_{m-1}(T_e) - y_m \left(C_m(T_e) + R_{m-1}(T_e) \right) + y_{m+1} R_m(T_e) \right) \tag{1.1}$$

Where T_e is the electron temperature, n_e is the electron density, R_i and C_i are the total recombination and ionization rate coefficients, and y_m is the fraction of a given element in charge state m. In eq. 1.1 we can see that the fraction of a given charge state is proportional to the electron temperature and electron density of the plasma and the fraction of the plasma that is in nearby charge states. The plasma is being accelerated through the corona and doesn't always have time to reach an equilibrium between its ionization and recombination, unless confined to closed loops. However, once the electron density decreases enough the ionization and recombination rates of the ions drop to a point where they are much less than the expansion time of the plasma, becoming so infrequent that the ionization and recombination essentially stops. The point at which the plasma ionization level stops evolving is called the "freeze-in point" (e.g., Hundhausen et al. 1968).

Once "frozen-in", the distribution of charge states remains constant as the solar wind travels in the heliosphere. This freeze-in point is different for the various elements and solar wind conditions, but is usually less than 2 solar radii for most elements (Ko et al. 1997). Due to this process the final charge states of an element in the plasma measured in situ can be related back to the temperature, density, and bulk speed of the plasma in the corona. Hence, charge state composition measured anywhere in the heliosphere is a probe into the heating and acceleration processes that occurred in the solar corona.

1.2.2. Heavy ions in the solar wind

1.2.2.1. Measurements of Heavy Ions

The measurement of heavy ions – specifically the velocity (v), density (n), and temperature (T) of the individual charge states of ions – has revealed key differences in the fast and slow solar wind. These fundamental properties of ions are used to characterize the solar wind. In general, the speed distribution of the particles in the solar wind are approximated as Maxwell-Boltzmann distribution when assuming an isotropic distribution:

$$f_v = n\left(\frac{m}{2\pi kT}\right)^{\frac{3}{2}} e^{-\left(\frac{m(v-u)^2}{2kT}\right)} \tag{1.2}$$

Here f_v is the distribution function, n is the density, m is the mass, and k is the Boltzmann constant. Once integrated over all velocities, the velocity distribution function gives the total number density of the ion species. In this function the bulk velocity (u) and temperature characterize the peak and width of the distribution (i.e. higher temperatures lead to a wider distribution). This temperature is related to the thermal velocity of the distribution:

$$V_{th} = \sqrt{\frac{kT}{m}} \tag{1.3}$$

This temperature measurement should not be confused with the freeze-in temperature of the plasma derived from the charge state ratios. The temperature derived from the charge state is interpreted as the temperature of the free electrons at the freeze-in point. The thermal temperature of the solar wind is the measured in-situ thermal spread of the individual ion distribution function.

The velocity distribution function departs from a Maxwellian when the solar wind is measured closer to the sun, where full three-dimensional velocity distributions are necessary to resolve the solar wind properties (Marsch et al. 1982). The Helios plasma analyzer, an instrument that was flown on the Helios spacecraft that measured the solar wind in the inner heliosphere, was first able to provide these 3D velocity distributions for proton (H^+) and alpha (He^{2+}) data, and observed a variety of differently shaped distributions. One of the more prominent deviations from Maxwellian was shown to be a clear temperature anisotropy parallel and perpendicular to the magnetic field ($T_\perp > T_\parallel$) in the fast solar wind (Marsch et al. 1982). Unfortunately, present measurements of heavy ions are unable to obtain different temperatures for the parallel and perpendicular components in the inner heliosphere, but new instruments are in development to provide these measurements (see Chapter 4).

1.2.2.2. Science of Heavy Ions

The elemental composition of the solar wind is also a tracer of the solar wind type. The fast and the slow solar wind have different charge state ratios measured in situ that can be related back to their source. Geiss et al. (1995) were able to show that the fast solar wind had a low charge state composition when compared to the slow solar wind (e.g., O^{7+}/O^{6+} ratio was low in the fast solar wind and high in the slow solar wind). The measurements of these charge state ratios showed that the temperature at the freeze-in point for these plasmas was different because the final charge state ratios are determined by the temperature at the source (as seen in eq. 1.1). Along with the ionic charge state differences between the two types of wind there was also discovered to be compositional difference in the solar wind when in-situ measurements are compared to remote measurements of the solar wind in the photosphere. In particular the solar wind measured in-situ has an enhancement of heavy ions with low first ionization potential (FIP). The FIP of an element is a measure of how much energy it takes to strip the first electron away from an atom. As ions are created from neutrals in the corona they are preferentially selected and drawn into the corona. This selection process causes an enhancement of elements which are ionized first. This increase in low FIP elements in the solar wind is known as the FIP effect. The exact cause of the preferential selection of low FIP elements is still debated (e.g. Vauclair & Meyer 1985; von Steiger & Geiss 1989; Laming 2012). The FIP effect is best characterized when comparing a low FIP elements (< 10 eV) to a high FIP element (> 10 eV). Geiss et al. (1995) showed the abundance of a low FIP element (Mg) being enhanced over that of a high FIP element (O) in the slow solar wind but not the fast solar wind (seen in figure 1.3). In figure 1.3 we can see the Mg/O ratio and the velocity of the solar wind plotted as a function of time. Here we see an anti-correlation between the velocity of the solar wind and the Mg/O ratio.

This same effect was not seen in the fast solar wind. Having part of the solar wind enhanced in low FIP elements over high FIP elements means that there is a process at the source that is preferentially selecting those low FIP elements. This FIP enhancement is observed to most prominently occur in the slow solar wind, telling us that the mechanisms responsible for creating and releasing the slow solar wind is different than those of the fast solar wind. In other words, the slow and fast solar wind must originate from different sources. The ratio between a low FIP element and high FIP element can be used to identify the source region of the solar wind due to the fact that the fast solar wind does not have a large FIP enhancement. This FIP effect is used extensively in Chapters 2 and 3 as a way to identify the different source regions of the solar wind.

This FIP effect is also important because it can be used to separate the different types of wind in in situ measurements, based on origin and not on properties that can change in situ, such as velocity. The fast solar wind has a composition that is consistent with that observed in coronal holes, while the slow solar wind has a more varied composition, which prevents us from easily identifying the source region.

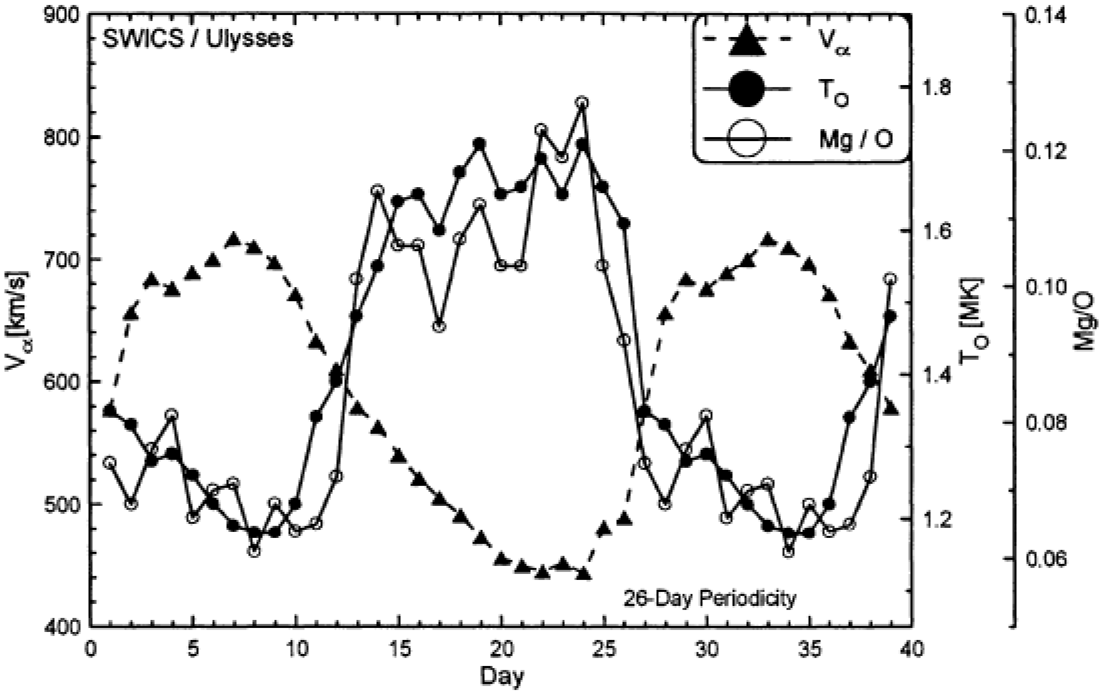

Figure 1.3: From Geiss et al. 2015. A superposed epoch plot of the Mg/O ratio showing a difference in this ratio for the fast solar wind and the slow solar wind.

The different speeds, temperatures, and composition of the slow and fast solar wind point to different origins on the Sun for each type. Remote sensing techniques in the early 1970's suggested that the fast solar wind originated from coronal holes (e.g., Krieger et al. 1973). Coronal holes are regions of low density plasma on the Sun that have open magnetic fields. Noci

(1973) furthered this argument by looking at the energy balance of coronal holes and concluding that they should have the largest solar wind energy fluxes on the Sun. The origin of the slow solar wind is still a debated subject in the field and several prominent theories exist to address this question (see section 1.3).

1.2.3. Solar cycle

The Sun has an 11 year cycle during which it evolves from a period of “solar minimum” to a period of “solar maximum” and has a magnetic field reversal. This cycle changes several important characteristics about the Sun and the solar wind. The elemental and ionic composition of heavy ions in the solar wind not only varies with the different types of wind but also over the solar cycle. When the Sun is close to solar minimum it tends to have a well-organized magnetic field and have very little solar activity. The solar activity of the Sun is related to the magnetic activity and drives the number of sunspots, flares, and CMEs produced by the Sun. Close to solar maximum the Sun’s magnetic field becomes more complex and there is increased solar activity. During solar minimum the slow solar wind is confined to a narrow band around the heliospheric current sheet and can only extend up to 30°- 40° (Antiochos et al. 2011). Figure 1.4 from McComas 2003 shows two measurements of the sun over the different parts of the solar cycle. This figure is split into 3 sections. The bottom subplot shows the sunspot number over the course of the whole solar cycle. The top two sections show the solar wind velocity during solar minimum (left) and solar maximum (right) on a polar plot. In the solar minimum subplot (upper left) we can see that the fast solar wind is confined to the poles of the sun, and that the magnetic field is mostly outward in the north and inward in the south (as seen by the color). In the solar maximum subplot (upper right) we see that there is no clear arrangement of the solar wind velocity with latitude on the sun, instead slow and fast solar wind are seen at all latitudes.

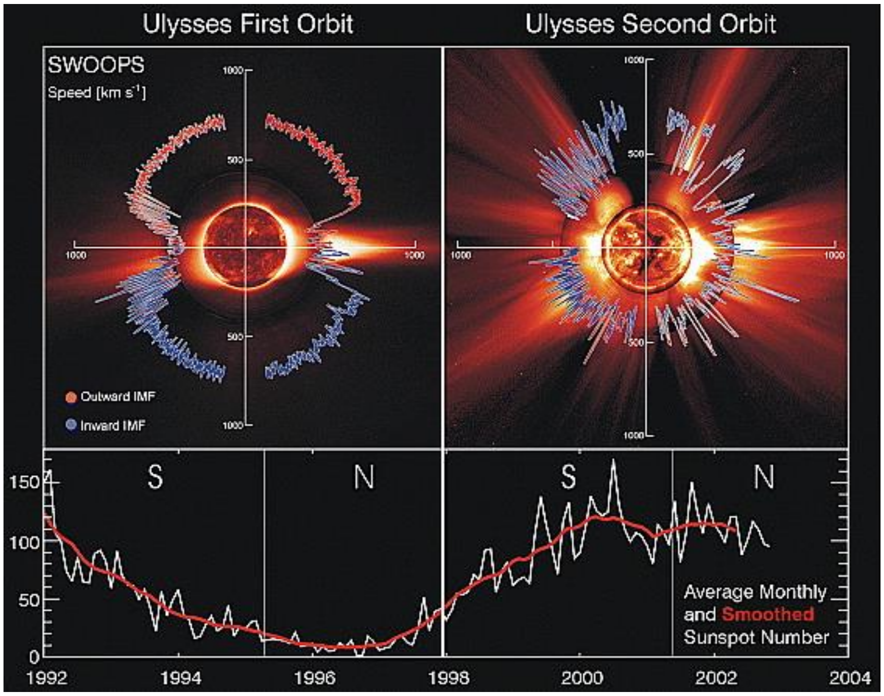

Figure 1.4: From McComas 2003. Two passes of the Ulysses spacecraft over different parts of the solar cycle show different configurations for the speed of the solar wind.

It has also been shown that throughout the solar cycle there are differences in the elemental composition streaming off of the Sun. Lepri et al. 2013 showed that there was a decrease in heavy ions relative to hydrogen during solar minimum when compared to solar maximum. They also showed that there was variability in the charge state ratios over the course of the solar cycle. Kasper et al. 2012 showed that the helium abundance varies over the solar cycle and depends on the solar wind velocity, as seen in Figure 1.5. In figure 1.5 the relative abundance of helium to hydrogen by number density is given ($A_{He} = 100\ x\ n_{He}/n_H$) for numerous velocity ranges indicated by color. Here we can see that during solar minimum at the left and right of the figure (which is approximated by the low sun spot number given with the black line) there is a decrease in the helium abundance for the slower velocity. This figure also shows that the higher velocity solar wind does not see as much of a decrease in the helium abundance over the solar cycle. Due to the variable nature of the sun (both in latitude and time), measurements taken in situ have to take into account both where and when the measurement were taken. Comparing measurements at different points in the solar cycle can lead to skewed conclusions about their differences, particularly for classification of the wind with charge state ratios.

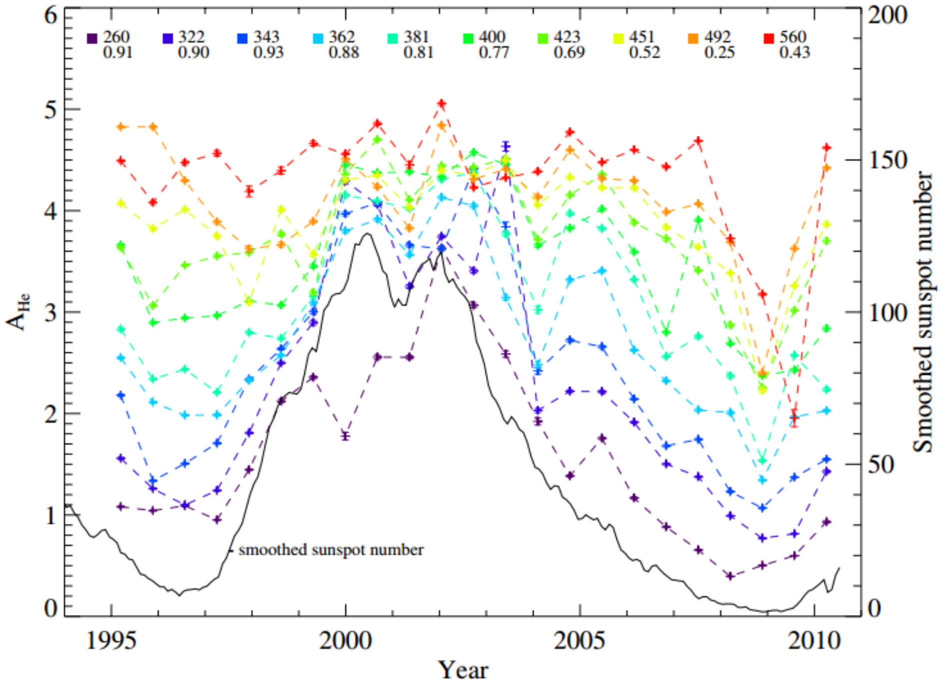

Figure 1.5: From Kasper et al. 2012. Solar cycle dependence of the He abundance separated by solar wind velocity

1.3. Theories on the Origin of the Solar Wind

Both the origin and heating of the solar wind are outstanding problems in heliophysics. Determining the origin of the slow solar wind can help us better understand the differences in source regions at the Sun and the factors that play into solar wind acceleration and heating. Four leading theories have been developed to explain the origin of slow solar wind; these are described in the following sections.

1.3.1. Expansion factor

The first set of theories considered are characterized by relating the expansion of the magnetic field to the solar wind velocity. This expansion factor is through to affect the energy available to accelerate the solar wind and argues that all of the solar wind originates from coronal holes, including the slow solar wind, which expands out from the edge of coronal holes into the heliosphere (e.g., Wang and Sheeley 1990, Cranmer et al. 2007). These theories observe a correlation between solar wind speed and the magnetic field divergence rate. Figure 1.6 shows a diagram of the expansion of the magnetic field lines demonstrating how field lines at the edge of coronal holes expand more than those as the enter of coronal holes. Proponents of the expansion factor model argue that the expansion can cause a reduction in the solar wind speed by mass conservation and by possibly limiting the acceleration of the wind, accounting for the velocity difference between the two types of solar winds (Wang and Sheeley 1991). The drawbacks to the expansion factor theory are that it does not account for differences in the composition and charge state of the solar wind, which will be addressed later in this section and in Chapters 2 and 3.

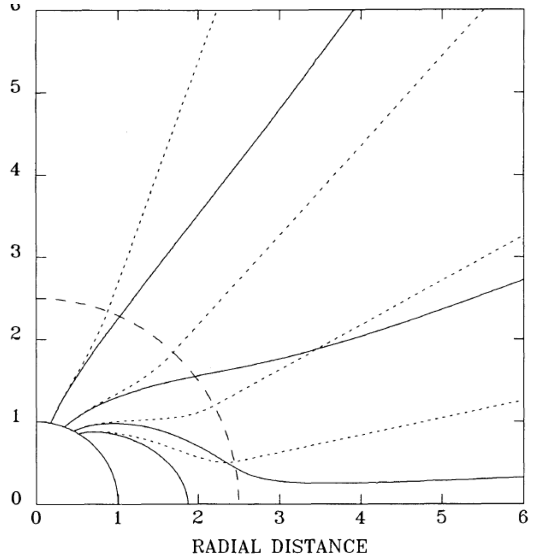

Figure 1.6: From Wang and Sheeley 1990. A diagram of magnetic field lines from the surface of the sun to 6 solar radii.

1.3.2. Interchange reconnection

Another theory suggested to explain the origin of the slow solar wind invokes interchange reconnection. This theory postulates that the open flux from coronal holes can reconnect with the closed flux of magnetic loops. When this reconnection occurs the plasma formerly trapped on the closed magnetic field lines is released into the heliosphere (Crooker et al. 2002, Fisk 2003). Figure 1.7 shows a diagram of this interchange reconnection. In this figure we can see an open field line and a closed field line reconnect from panel (c) to panel (d). Some of the main points that need to be explained with interchange reconnection models are how and where the reconnection occurs. In one formulation of this source mechanism, the open flux in coronal holes is driven into the closed flux region due to a diffusion process and convective motions on the solar surface (Fisk 1996, Fisk el al. 1999, Fisk 2001), where it can reconnect.

The physics of the interchange process can reproduce the lower speeds observed in the slow wind (Fisk 2003) as well as the fast speeds of the fast solar wind. The reconnection of loops allows for fast solar wind to be generated from short lived, small loops in coronal holes, and for slow solar wind to be generated from long lived, large loops. Plasma trapped on the large closed loops have a much higher temperature than the temperature of plasma measured at the same coronal height of open field lines. This higher temperature results in an increase in the ionization of the solar wind originating on these loops. This enhanced ionization is reflected in the compositional charge state difference in the slow solar wind (Fisk 2003). The FIP effect of the slow solar wind can also be explained with this theory. The longer that the plasma is confined to loops, the more it will be effected by the FIP effect (Widing & Feldman 2001). This leads to an enhancement of low FIP elements in the slow wind that was confined to large loops for a long time, while the fast wind generated from short lived small loops will not show this enhancement.

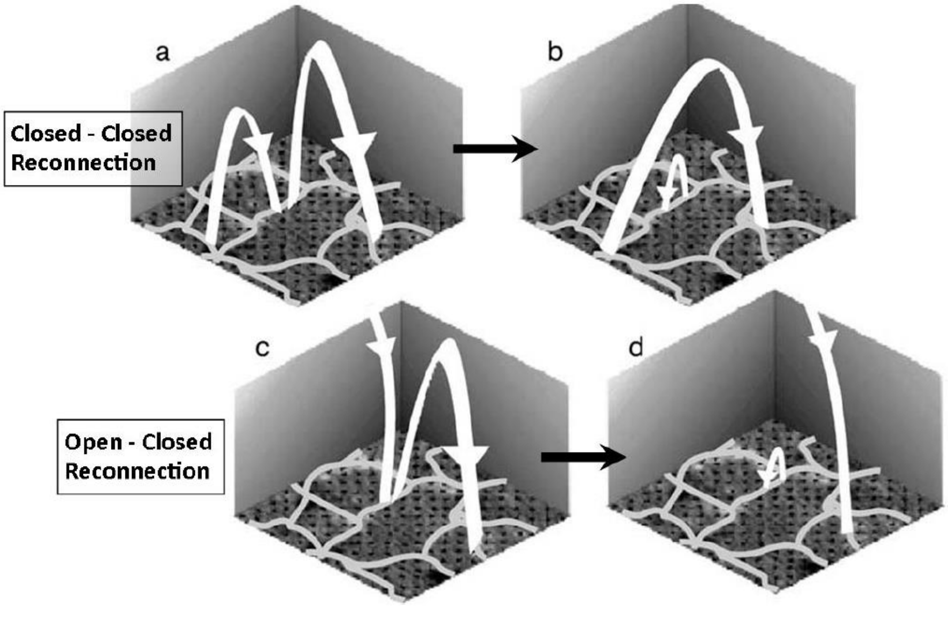

Figure 1.7: From Fisk 2003. A diagram of interchange reconnection in two scenarios. Closed-closed reconnection is shown in (a) and (b). Open-closed reconnection is shown in (c) and (d)

1.3.3. S-Web

The third theory, the S-web model, also argues that the source for the slow solar wind is interchange reconnection between the open and closed flux. However, in this model, open flux cannot be driven into the closed flux region as easily as in the interchange model described above

(Antiochos et al. 2011). Antiochos et al. (2007) argue that only one coronal hole per polarity can exist because additional coronal holes would violate the force-free assumption in the corona. Instead the open fields, at the edges of coronal holes, weave their way towards the closed field region via thin corridors of open flux. These corridors are the sites of continuous magnetic reconnection that frees the slow solar wind from the closed field lines (e.g., Antiochos et al. 2007, Antiochos et al. 2011). These thin corridors are not usually seen by remotes sensing instruments because they are less bright than the overarching closed field structure along the line of sight. It is argued that this extended region of reconnection between the open and closed field lines woven into the corridors can then be traced to higher latitudes away from the current sheet allowing for the slow solar wind to be observed as far out as 30° from the heliospheric current sheet, reproducing observations.

1.3.4. Streamer top model

Finally, there is a streamer top model, which suggests that the slow solar wind originates from the opening of closed loops at the top of the helmet streamers (e.g., Suess et al. 1996, Mikic et al. 1999, Endeve et al. 2004, Rappazzo et al. 2005). This model suggests that there exists a balance of plasma pressure and magnetic pressure within the closed loop. When the pressure of the plasma on the close loop exceeds the magnetic pressure the loop reconnects releasing the plasma into the heliosphere (Suess et al. 1996). Due to the nature of this model, solar wind that originates via the streamer top is predicted to be close to the heliospheric current sheet. Figure 1.8 shows a diagram of wind released via the streamer top model. In this figure the top of largest closed magnetic loop opens up to the heliosphere, releasing the slow solar wind, with the fast solar wind at its flanks.

This model has been criticized for not being able to explain how the slow wind fills a large portion of the heliosphere at times, and expands well beyond the angular width of helmet streamer (Wang et al. 1998).It is also argued that this type of solar wind release would occur even if one of the other theories accounts for the majority of the solar wind, leaving this theory to explain slow solar wind confined around the heliospheric current sheet.

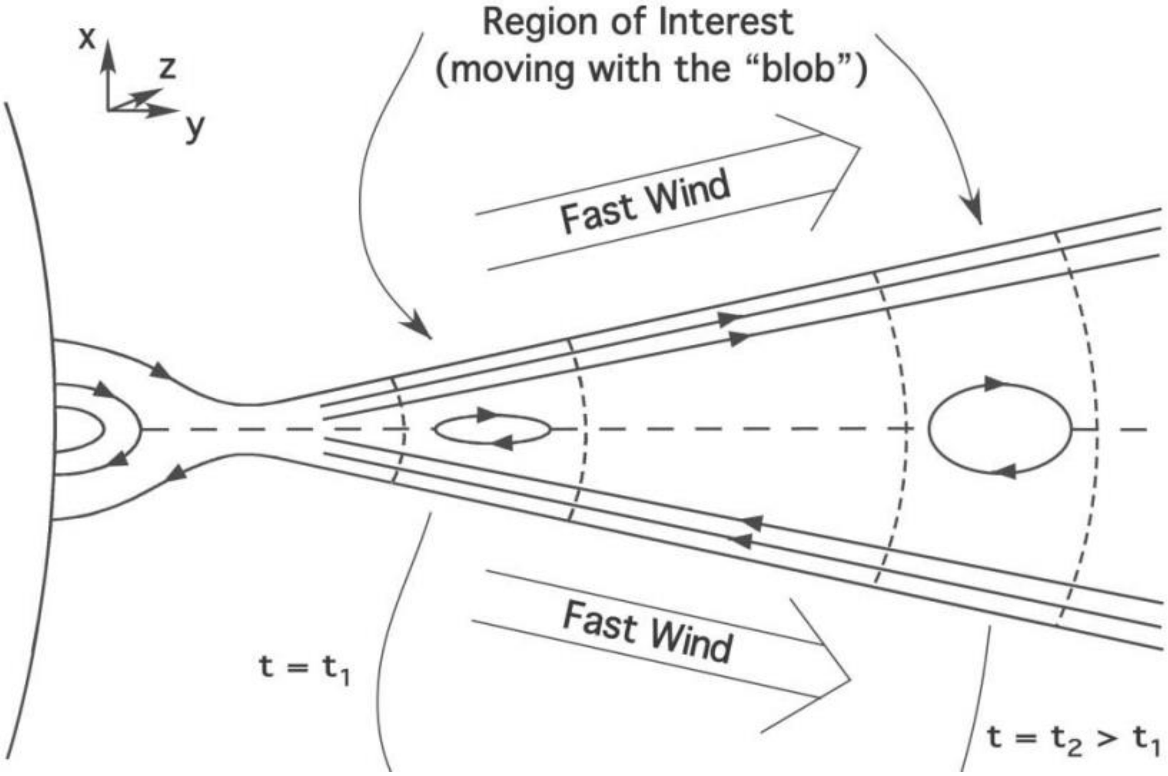

Figure 1.8: From Rappazzo et al. 2005. A diagram of streamer blobs and fast solar wind originated at streamer tops.

1.4. Theories on the Heating of the Solar Wind

Another major question still debated in the heliophysics community concerns the heating of the solar wind. In order to understand the solar wind we need to know not only where it originates, but also how it is created. It is known from remote sensing and in situ measurements that the solar wind is heated in the solar corona to kinetic temperatures exceeding 10^6 K. Several properties of the solar wind have been measured that are thought to relate to the heating processes that is occurring in the solar corona. (1) Observations show that in the fast solar wind there exists a large thermal temperature anisotropy ($T_\perp > T_\parallel$); (2) there is differential streaming between heavy ions and protons; and (3) there is a more than mass proportional temperature difference seen between heavy ions and protons ($T_j/m_j > T_i/m_i$) (McKenzie, Banaszkiewicz, and Axford 1995) in both the parallel and perpendicular directions (Tracy et al. 2015).

The heavy ion data used in this dissertation do not differentiate between parallel and perpendicular temperatures, instead the reported heavy ion temperature is the temperature in the radial direction. This is one of the main downfalls of the ion data from the SWICS instruments used in this dissertation (see section 1.5 for a discussion of SWICS and the data). The new Heavy Ion Sensor (HIS) will be able to overcome this deficiency in measurement by determining 3D velocity distribution functions and providing measurements of the parallel and perpendicular temperatures (see section 1.5.5 and chapter 4 for further details).

These properties of the solar wind provide us with clues about the specific heating mechanism. Several theories have been developed to answer this heating problem. In general most theories rely on some form of dissipation of waves to insert energy into the plasma at the corona, as described in the following sections.

1.4.1. Alfvén wave heating

One theory on the heating of the solar wind relies on dissipation of Alfvén waves in the corona (e.g., Belcher & Davis 1971). Alfvén waves are generated below the corona by magnetic field fluctuations due to the motion at the base of the magnetic field and propagate outward. These Alfvén waves then encounter gradients in the density that result in some of them being reflected back towards the Sun. This reflection process then results in counter-propagating waves (e.g., Cranmer 2010), which can cause a non-linear turbulent cascade, releasing energy into the plasma and heating the solar wind (Velli et al. 1989).

1.4.2. Ion cyclotron wave heating

Ion cyclotron wave heating is similar to Alfvén wave heating. The mechanism responsible for the heating is a resonance between left-hand polarized Alfvén waves and positive ions gyrating at a specific frequency (Cranmer 2000). It has been shown that this heating mechanism can recreate temperature anisotropies ($T_{\perp} > T_{\parallel}$) and more than mass-proportional ion temperatures as seen in the solar wind (McKenzie, Banaszkiewicz, and Axford 1995). All ions can interact with ion cyclotron waves to be heated, but ions with mass/charge greater than protons can also interact with counter-propagating waves, resulting in even more heating (Kasper et al. 2013).

The differences between ion cyclotron wave heating and Alfvén wave heating lie in the process through which the energy is exchanged between the waves and the particles and the direction of waves (ion cyclotron waves travel predominantly parallel to the magnetic field, while kinetic Alfvén waves travel perpendicular). The main drawback for ion-cyclotron heating is that it is not clear whether enough energy can be generated to accommodate all of the heating required to match observations (Chandran et al. 2013).

1.5. Measurement Techniques of Heavy Ions in the Solar Wind

Several methods exist for measuring the properties of heavy ions in the heliosphere. Measurements of heavy ions consist of two types: remote observations of heavy ions near the Sun, and in situ measurements in the heliosphere. Both measurements are very important in understanding where the solar wind originates and how it is heated and accelerated.

This dissertation focuses on the use of available in situ measurements of heavy ions. In Chapters 2 and 3 these heavy ion measurements are used to study the origin and acceleration of the solar wind. In Chapter 4 a new heavy ion instrument – heavy ion sensor (HIS) – is analyzed in great detail in order to fundamentally understand the inner workings of the instrument in preparation for calibration.

1.5.1. Early in situ measurements

Heavy ions were first measured in situ using an electrostatic analyzer on Mariner-2 (Snyder and Neugebauer 1962, Wuest 2007). These instruments were able to detect the presence of heavy ions but not identify what specific species they were. The measurement of heavy ions in situ was improved with the CHEM instrument, which combined the electrostatic analyzer with a time-of-flight section, both of which will be described in the following section (Gloeckler 1977). The addition of the time-of-flight section to the instrument allowed the CHEM instrument to separate individual charge states of ion.

After the CHEM instrument, Gloeckler and his team designed and launched the SWICS instrument, which improved upon the time-of-flight mass spectrometer design (Gloeckler et al. 1992). The SWICS instrument has been flown on several missions, including: Ulysses and Advance Composition Explorer (ACE). Data sets from both of these instrument are used extensively throughout this dissertation. To date, the data from the SWICS instrument is the best available measurements for heavy ions in the solar wind.

1.5.2. Time of flight mass spectrometers

Although several different types and variation of time-of-flight mass spectrometers exist, this dissertation will specifically address how linear triple-coincidence TOF mass spectrometers work (specifically the before mentioned SWICS and HIS instruments). Figure 1.9 is a diagram of the SWICS instrument and shows the flight of a particle going through the two main sections of the SWICS instrument: the Electrostatic Analyzer section (ESA), and the Time-of-Flight section (TOF).

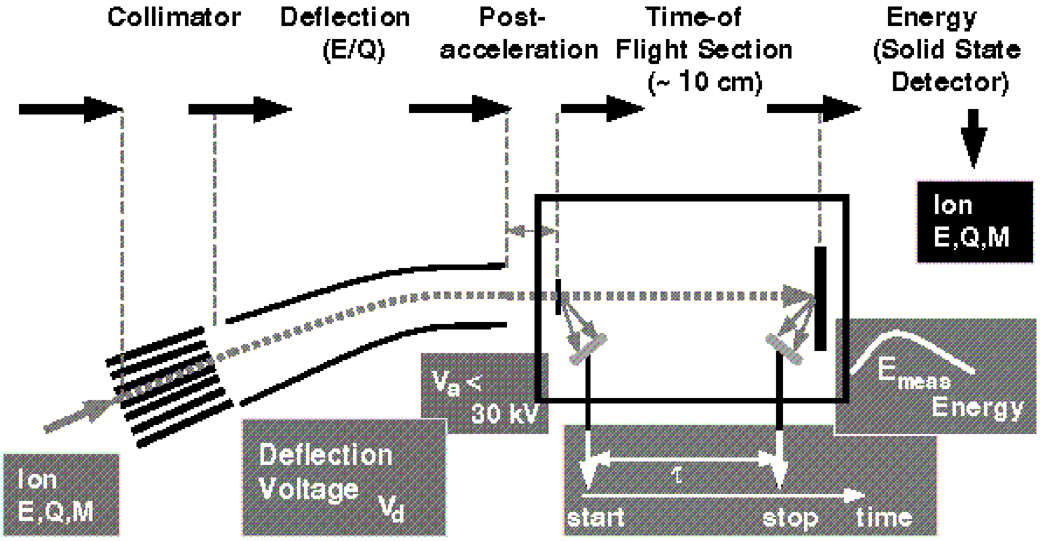

Figure 1.9: Diagram of the SWICS TOF Mass Spectrometer

The ESA uses electrostatic fields to deflect particles entering the instrument. Electric and magnetic fields can deflect a particle by imparting a force on it known as the Lorentz force (eq. 1.4)

$$\boldsymbol{F} = q\,(\overline{\boldsymbol{E}} + \boldsymbol{v} \times \boldsymbol{B}) \tag{1.4}$$

Where $\boldsymbol{F}$ is the force, q is the particle's charge, $\overline{\boldsymbol{E}}$ is the electric field, $\boldsymbol{v}$ is the velocity of the particle, and $\boldsymbol{B}$ is the magnetic field strength. The ESA section of the instrument applies this force to deflect the ion in a curved trajectory with an electric field. The final radius of the ion's flight path can be found by comparing the centripetal force (eq. 1.5) to the Lorentz force (eq. 1.4).

$$\boldsymbol{F_C} = m\boldsymbol{a} = \frac{m(v \sin\theta)^2}{r} \tag{1.5}$$

Where m is the mass, $\boldsymbol{a}$ is the acceleration, r is the radius of curvature, and θ is the angle between the ion's velocity and the force direction (in this case the electric field direction). We can then substitute eq. 1.5 into eq. 1.4 in the absence of a magnetic field and solve for r.

$$q\boldsymbol{e} = \frac{m(v \sin\theta)^2}{r} \tag{1.6}$$

$$r = \frac{mv^2 \sin^2\theta}{q\boldsymbol{e}} \tag{1.7}$$

$$r = \frac{E}{q}\frac{2 \sin^2\theta}{\boldsymbol{e}} \tag{1.8}$$

In the absence of a magnetic field (a correct assumption for the SWICS and HIS instruments), the force on the particle becomes proportional to its energy per charge (E/q). In the ESA section of the instrument several charged plates are used to create an electric field deflecting particles based on their E/q. Once a voltage is set, only ions within a certain range of E/q can fly through the ESA. Ions with too much energy or too little charge will not be deflected enough to make it past the ESA section and will collide with the wall of the instrument. The same applies to ions with too little energy or too high of a charge. Once an ion makes it past the ESA section of the instrument, the E/q of that ion is known and it proceeds to the TOF section. The TOF section in the mass spectrometer measures the time it takes for an ion to travel a known distance. The velocity can be calculated based on this time and distance. Finally, the SWICS and HIS instruments employ a solid state detector (SSD) at the back end of the instrument to measure the final energy (E_m) of the ion. The ions mass (m), charge (q), and initial energy (E_{int}) can then be calculated from the velocity (t/d), E/q, and $\boldsymbol{E}$ measurement (E_m) as shown in equations 1.9 – 1.12

$$\boldsymbol{E} = \frac{1}{2}m\boldsymbol{v}^2 \tag{1.9}$$

$$m = 2\left(\frac{t}{d}\right)^2\left(\frac{E_m}{\alpha}\right) \tag{1.10}$$

$$\frac{m}{q} = 2\left(\frac{t}{d}\right)^2\left(V_a + \frac{E_{int}}{q}\right) \tag{1.11}$$

$$q = \frac{\left(\frac{E_m}{\alpha}\right)}{\left(V_a + \frac{E_{int}}{q}\right)} \tag{1.12}$$

Here the instruments SSD detector efficiency (α) and post acceleration voltage (V_a) are taken into account. Ions that obtain a time of flight measurements (start and stop signal) and an energy measurement are reported as triple coincidence measurements. Further details into this derivation for the SWICS instrument can be seen in Gloeckler et al. 1992.

1.5.3. SWICS on Ulysses

The SWICS instrument was flown on two spacecraft over the course of 20 years. The first flight of the SWICS instrument happened on the Ulysses spacecraft. The Ulysses spacecraft was launched in 1990 and continued to collect data until it was decommissioned in 2009. The spacecraft was placed into a unique polar orbit allowing the SWICS instrument to observe the solar wind from different latitudes (every latitude between ±80°). The spacecraft also has an elliptical orbit ranging from 1.5 astronomical units (AU) to 5 AU. This allowed the SWICS instrument to study the solar wind at different distances. The instrument was capable of measuring the velocity, density, and thermal velocity of more than 40 different charge states of 9 heavy elements (He, C, N, O, Ne, Mg, Si, S, and Fe) between 0.16 KeV/e and 60 KeV/e, capturing the typical energy range for the bulk solar wind. The SWICS instrument on Ulysses had a cadence of 3 hours in order to measure enough ions to get a statistical sampling of the solar wind.

1.5.4. SWICS on ACE

After the SWICS instrument was already in flight on the Ulysses spacecraft for 6 years, the flight spare was repurposed and placed on the Advanced Composition Explorer (ACE) spacecraft. ACE was launched in 1998 and still operates today. The spacecraft was placed at the first Lagrangian (L1) point, resulting in a stable orbit between the Sun and the Earth at the point where the gravitation influence of both bodies are equal. This placement provides the SWICS instrument aboard the spacecraft with in-ecliptic observations of the solar wind. Due to its location between the Earth and the Sun, ACE acts as an upstream solar wind monitor to provide early warning of dangerous solar activity. The location of ACE also provides the spacecraft with an unobstructed view of the side of the Sun that most affects the Earth. The SWICS instrument on ACE provides the same data products as the SWICS instrument on Ulysses but at a faster cadence, and to a higher energy range of 100 KeV/e. The density, velocity, and thermal velocity of the heavy ions can be measured as fast as once every 12 minutes, but only during high flux. The most reliable and available data products have a cadence of 1 or 2 hours. The longer accumulation time allows for more ions measurements, which in turn allows for more precise determination of the density, velocity, and thermal velocity of each ion species.

1.5.5. HIS

The HIS instrument is a new TOF mass spectrometer set to launch on the Solar Orbiter (SO) spacecraft in 2018. Along with the E/q, E, and TOF measurements that are common in TOF mass spectrometers the HIS instrument will also resolve the azimuthal and elevation angle of ions. The density (n), velocity (v), and thermal temperature (T) are the final data products generated from in situ plasma instrument that are used to describe the distributions of ions. As discussed before in section 1.2.1 and equation 1.2 the density, velocity, and thermal temperature of the ion describes the distribution of particles. Due to interactions with the magnetic field the distribution of ions in the solar wind can deviate from the standard Maxwellian distribution (Marsh et al. 1982). These deviations from an isotropic distribution call for measurements in 3 spatial dimensions (i.e. 3D velocity distribution function). The HIS instrument improves upon previous heavy ion instruments by measure the elevation and azimuthal angle of each individual particle to create full 3D velocity distribution functions. These 3D distribution functions can then be coupled with magnetic field data also taken on the spacecraft to resolve the parallel and perpendicular distributions to the magnetic field.

The Solar Orbiter spacecraft will also have an elliptic orbit (periapsis of 0.3 AU, apoapsis of 0.7 AU) with a variable inclination over the course of its mission that starts at 0° and ends at 30°). This inclination and orbital distance will allow for the HIS instrument to examine the solar wind in a novel fashion. Due to the orbital radius, the flux hitting the instrument will be high enough to collect heavy ion data at an unprecedented 30 second cadence.

The fourth chapter in this thesis supports the development of this sensor through the analysis of the sensors measurement properties and the characterization of its geometric factor and efficiencies. Due to the complexity of the instrument, calculating an analytical solution to the electrostatic fields in the instrument is extremely difficult, if not impossible. To help understand how the ion behaves in the instrument an ion optical program called SIMION is used (SIMION 3D, version 8.1 (Dahl et al. 2000)). SIMION solves the Laplace equation using a finite difference method to calculate the electrostatic potential throughout the instrument numerically.

1.6. Dissertation Objective

1.6.1. Focus of the thesis

This dissertation consists of two parts. Part one (Chapters 2 and 3) is a study of the solar wind using available heavy ion data to better understand the origin and heating of the plasma. This was accomplished through investigating the kinetic and compositional properties of the fast and slow solar wind. The second part of the dissertation (Chapter 4) is a detailed study the HIS instrument using an ion optical model. Using Monte Carlo simulations of ions flown through the HIS instrument the geometric factor and TOF efficiencies are calculated, deepening our understanding of the inner working of the instrument. This analysis is done in preparation for the final calibration of the instrument.

Each chapter of this dissertation is meant to be a standalone section and does not require the knowledge gained in any other chapter. Both Chapters 2 and 3 have been published in the Astrophysical Journal (ApJ), a peer-reviewed journal.

1.6.2. Guiding science questions

In order to address the broader questions about the origin and heating of the solar wind we must ask and attempt to answer more specific science questions. What is the difference between fast and slow wind? What do the measurements of these winds in situ tell us about the acceleration process? Why are there distinct differences between different types of wind found in the heliosphere?

1.6.2.1. Is the fast solar wind seen at the poles different from the fast solar wind seen in the ecliptic?

Measurements of the solar wind have been taken at various latitude in the heliosphere over the last couple of decades. Several of the origin theories of the solar wind have different predictions for solar wind originating from different locations on the sun. For example, the expansion factor theory predicts a steady, smooth solar wind due to the fact the all of the solar wind originates from coronal holes. On the other hand, the interchange reconnection theory predicts that the solar wind would be patchy and that there would be little difference between the fast solar wind at the poles and the fast solar wind originating from the equator. Using heavy ion measurements from Ulysses and ACE we can determine the differences in the fast solar wind between the different latitude of origin, paying particular attention to the unchanging compositional parameters that tie the measured wind to its origin.

1.6.2.2. Are there multiple, separate populations of solar wind at the speeds which we use to define the slow solar wind?

One of the major differences between the fast and slow solar wind is the variability. The elemental composition and charge states ratios of the fast solar wind are steady, while extremely variable for the slow solar wind. Many theories explain this variability as a side effect of the release process from magnetic loops. The inclusion of several different populations of solar wind originating from various locations on the Sun could also help to explain the variability. If in fact, the fast solar wind is able to be slow down enough to have a velocity similar to that of an otherwise steady slow solar wind, at the same speed, the resulting wind will be highly variable in the composition. Using heavy ion data we can examine the slow solar wind's compositional and kinetic parameters and compare them to the fast solar wind.

1.6.2.3. Are the mechanisms responsible for the heating and acceleration of the fast solar wind the same as those responsible for the slow solar wind?

As mentioned above in section 1.3 there are numerous theories on the heating of the fast solar wind. Generally the heating and the acceleration of the solar wind is discussed in the context of the fast solar wind and does not mention the slow solar wind. Some believe that the mechanisms responsible for the creation and release of the slow solar wind might also be responsible for its heating (e.g., Fisk and Schwadron 2001, Suess 1996). The differential velocity and ion temperature ratios between protons and heavy ions can be used to examine the heating mechanisms of both the fast and slow solar wind. Comparing these parameters between the fast and slow solar wind can help us understand the heating mechanisms in the solar corona.

1.6.3. HIS motivation

Current in situ measurements of heavy ions in the solar wind are unable to provide full 3D velocity distribution functions in the inner heliosphere, and thus are unable to resolve the parallel and perpendicular temperatures. These parallel and perpendicular temperatures of heavy ions are needed to further investigate the heating and acceleration of the solar wind.

New heavy ion instruments are being developed to provide the necessary measurements to result the 3D distribution functions of the heavy ions. One such instrument, HIS, is discussed in Chapter 4 of this dissertation, focusing on the preparation for calibration and performance characterization. Once the HIS instrument is able to provide measurements of the solar wind, many of the outstanding questions regarding its heating and acceleration can be looked into in further detail using heavy ion data.

CHAPTER II

On the Origin of Mid-Latitude Fast Wind: Challenging the Two-State Solar Wind Paradigm

This chapter is taken from Mark Stakhiv, Enrico Landi, Susan T. Lepri, Rona Oran, and Thomas Zurbuchen (2015), On the Origin of Mid-Latitude Fast Wind: Challenging the Two-State Solar Wind Paradigm, *Astrophysical Journal, 801*, doi: 10.1088/0004-637X/801/2/100

2.1. Abstract

The bimodal paradigm of solar wind describes a slow solar wind situated near the heliospheric current sheet while a fast wind over-expands from the poles to fill in the remainder of the heliosphere. In this chapter, we challenge this paradigm and focus here on mid-latitude wind using three fast-latitude passes completed by the Ulysses spacecraft. Based on its composition and dynamic properties, we discuss how this wind differs from both the fast, polar coronal hole wind and the low latitude, streamer associated slow solar wind. Using a detailed analysis of ionic and elemental abundances, as well as solar wind dynamic properties, we conclude that there is a third quasi-stationary solar wind state, called the boundary wind. This boundary wind is characterized by a charge state distribution that is similar to slow wind, but with an elemental composition that is coronal-hole like. Based on these data, we present arguments for the location of the origin of this wind. We conclude that the boundary wind is a subset of the fast wind emanating from regions close to the boundaries of coronal holes, and is accelerated by a similar process.

2.2. Introduction

The solar wind observed in the heliosphere has traditionally been categorized into two quasi-stationary types based on its composition (e.g. Zurbuchen 2007 and references therein): fast, coronal hole associated wind and slow solar wind associated with streamers. This two-state phenomenon is most obvious in its observed charge state and elemental composition, which reflects both its origin as well as the wind's expansion history. Results from the Ulysses mission revealed that there was an inverse correlation between the charge state ratios (i.e., O^{7+}/O^{6+}) and solar wind speed (Geiss et al. 1995, Gloeckler et al. 2003). The solar wind charge states are determined by the electron temperature, density, and plasma flow velocity in the expanding corona before the freeze-in point (typically < 3-5 R_S) after which the ionic composition remains unchanged. The elevated charge states of oxygen in the slow solar wind indicate that there is an increase of electron temperature and/or density coupled with a relatively low velocity in the regions where it originates, allowing the ionic charge states to adapt more efficiently to the high temperatures of the inner corona. In contrast, the fast wind, associated with coronal holes, reflects an origin with lower electron temperature and density. A second characteristic difference between fast and slow solar wind is the elemental composition. Using mid- and high-latitude solar wind data measured onboard Ulysses, Geiss et al. (1995) found that the elemental composition of the wind is rather bimodal. The fast wind composition is approximately photospheric, while the slow wind is enhanced in elements with low first ionization potential (FIP), similar to the composition of the closed corona. A third characteristic distinguishing the solar wind types is the variability in both dynamic and compositional properties (Gosling 1997). The fast wind tends to have rather constant compositional signatures while the slow wind is more variable in nature (Zurbuchen & von Steiger 2006).

This bimodal picture of the solar wind has also been described using other heliospheric data-sets, especially in the inner heliosphere where the solar wind is more dynamically pristine and has yet to have its sharp transitions eroded due to momentum transfer between the fast and slow solar wind. For example, Schwenn et al. 1990 summarizes Helios data and suggests that there is a very sharp transition between a fast, rather steady solar wind and a slow, variable wind near the heliospheric current sheet. That nearly abrupt transition becomes increasingly evident the closer Helios observed near the Sun. Similarly, the inner state of the solar wind reflects this bimodal state: Fast wind velocity distribution functions exhibit distinctive deviations from a thermal equilibrium whereas slow wind streams are more Maxwellian (Marsch et al. 1982b, Marsch et al. 1991). Also, the turbulence exhibited in fast solar wind streams is indicative of outwards propagating Alfvén waves, whereas slow winds exhibit a more bi-directional turbulent spectrum (Marsch et al. 1991).

The physical processes that heat the open corona and the solar wind are still an ongoing topic of research. Several models and theories have been put forth to explain how the solar wind is heated and accelerated, which also link the acceleration process to the specific location of the source region of the wind. One such theory suggests that the solar wind is heated by wave dissipation and accelerated by gradients in the Alfvén wave pressure (e.g. Belcher & Davis 1971, Hollweg 1986, Cranmer 2007, van der Holst et al. 2014 and references therein). These theoretical models predict that the turbulent motions at the photosphere and chromosphere give rise to significant amounts of Alfvén waves and that the energy in these waves can be tapped through a variety of processes to accelerate the solar wind. Another model put forth by Lemaire and Scherer (1971) suggests that the ions are accelerated by a charge separation electric field. This electric field is set up by a larger escape flux of electrons than protons caused by the difference in their thermal velocities (Lemaire and Scherer 1973, Parker 2010). In both of these theories the acceleration occurs along open field lines associated with coronal holes.

Another method of acceleration that has been proposed is magnetic reconnection (e.g., Fisk 2003, or Crooker et al. 2002). These theories predict that the interchange reconnection between open and closed magnetic field lines can accelerate plasma previously captured on magnetic loops into the heliosphere, consistent with the compositional signatures of slow wind. Most recently, Antiochos et al. 2011 introduced the S-Web model, suggesting that magnetic reconnection along highly complex coronal holes boundaries is a source of the slow solar wind.

However, none of the proposed scenarios is able to account for all the properties of both types of the wind: acceleration and heating due to Alfvén waves may be steady, so by itself it cannot reproduce the patchiness and variability of the slow wind; wind acceleration along steady open field lines can only come from coronal holes, and thus should have near photospheric abundances, so it cannot account for the reported coronal element composition of the slow wind, which is typical of closed magnetic loops in the corona (e.g. Feldman et al. 2005). It is possible that multiple acceleration and heating theories are correct and that the fast and slow solar wind are heated and accelerated due to different processes, resulting in different signatures in the solar wind

The simple bimodal picture that the solar wind is made up of either fast or slow wind is not always accurate, especially near solar activity maximum. The limitation in classifying the wind into either fast or slow streams has previously been investigated by Zurbuchen et al. (2002), which reported that during solar minimum the velocity and O^{7+}/O^{6+} ratio appear bimodal, whereas during solar maximum this bimodal nature is replaced by a single peaked distribution covering a broader range of coronal temperatures and densities. Despite the continuum of dynamic states the elemental composition remains rather bimodal, with the lowest charge-state wind having near-photospheric composition and the higher charge-state wind exhibiting fractionated, coronal composition. Figure 2.1 shows a 14-day interval of Ulysses solar wind data gathered between 32 and 42 degrees latitude in 2007 that challenges the bimodal nature of the wind. This figure shows an observed transition from fast wind to slower wind and then another transition back to fast wind. Characteristics of these transitions can be seen in both the velocity (panel A) and the oxygen charge states (panel C). Panel D further shows that these fast-slow and slow-fast transitions occur in one and the same magnetic sector, without a transition through the heliospheric current sheet. The elemental composition (panel B), surprisingly, does not exhibit any transitions but stays rather constant, consistent with coronal hole associated wind. Most importantly, the wind that Ulysses observed between days 270 and 273 had elemental composition identical to the fast solar wind but had ion charge states and velocity that were typical of the slow solar wind. The aim of this chapter is to perform an analysis of solar wind data during the three fast latitude passes performed by Ulysses in order to analyze when and why cases such as in Figure 2.1 occur. We will place emphasis on looking for slow velocity solar wind that has photospheric abundances and comparing its composition and kinetic properties to the purely fast and slow solar wind.

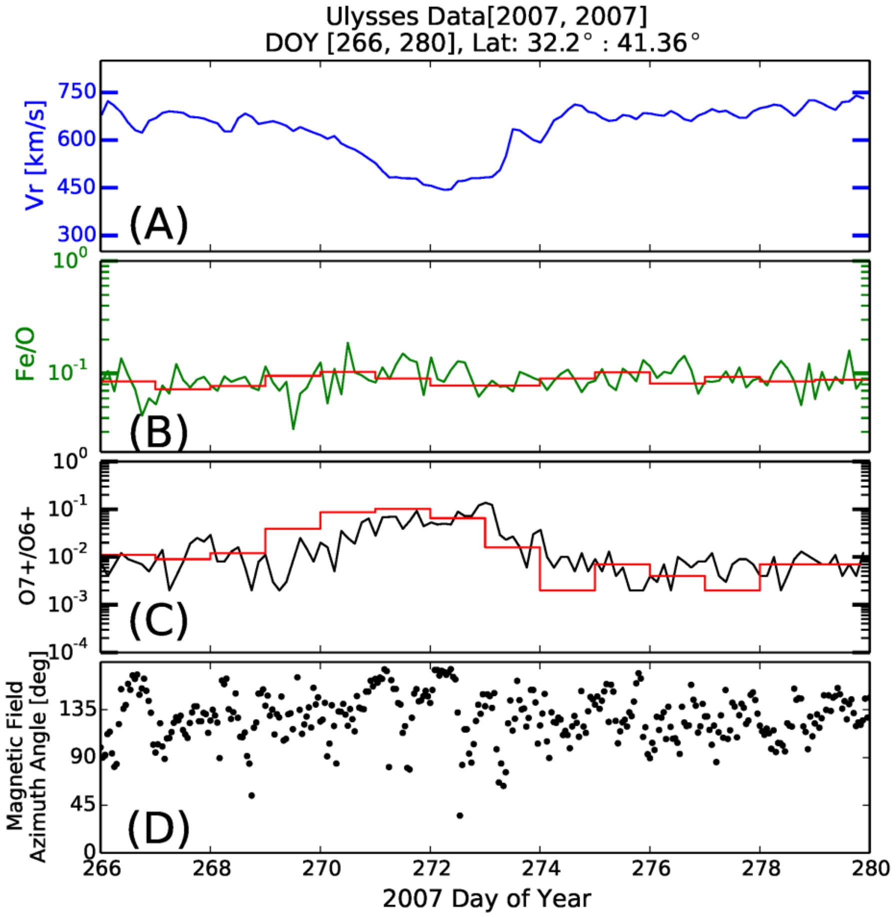

Figure 2.1: 14 day plot of solar wind using velocity, and compositional data. Panel A shows the proton velocity that shows a decrease from coronal hole values to a speed intermediate between slow and coronal hole wind. Panel D shows the azimuthal angle of the wind's magnetic field and indicates that the current sheet was not crossed. Panel B shows the wind's Fe/O ratio in three-hour intervals (green) and 24-hour intervals (red). Panel C shows O7+/O6+ ratios in three-hour intervals (black) and 24-hour intervals (red). The transition to slower wind is accompanied by an increase of the O7+/O6+ ratio to values typical of streamer-associated slow wind. The elemental composition does not change.

We will first introduce the data used in this study in Section 2, and then analyze the mid-latitude wind in Section 3 focused on three fast-latitude passes by Ulysses, measurements taken near the periapsis-passes of this mission. Section 4 will discuss the finding of this new type of solar wind and its implications in the overall picture of the solar wind.

2.3. Observations

Data used for this analysis were obtained from three different instruments providing measurements of solar wind composition, plasma characteristics and magnetic field.

Compositional data from Solar Wind Ion Composition Spectrometer (SWICS) were taken from the Ulysses archive and have 3 hour time resolution. Sometimes, 24 hour time resolution data were also used, especially to separate statistical variability from real compositional changes. The Fe/O, C^{6+}/C^{5+}, O^{7+}/O^{6+}, He^{2+} velocity, O^{6+} kinetic temperature, and O^{6+} velocity data products from the SWICS instrument were used in this analysis. For more details about the analysis procedure and the instrument refer to Gloeckler et al. 1992 and von Steiger et al. 2000. We used proton velocity, temperature, and density plasma data measured from the Solar Wind Observations Over the Poles of the Sun (SWOOPS, Bame et al. 1992). Finally, we used 1 hour magnetic field measurements from the Vector Helium Magnetometer (VHM, Balogh et al. 1992). All 3 data sets are available at the Ulysses archive at http://ufa.esac.esa.int/. This combination of data is uniquely suitable for this analysis for two principal reasons. First, the length of the Ulysses data set extends nearly 20 years covering almost a full magnetic cycle of the Sun. This length of time allows us to study the solar wind over the course of multiple solar minima. Second, the Ulysses spacecraft had a unique polar orbit that allowed for measurements away from the ecliptic plane, unlike the in-ecliptic measurements available from other instruments. This polar orbit allows analyzing the solar wind at all latitudes.

This chapter focused on three periapsis passes of Ulysses, the so-called “fast-latitude scans” that Ulysses performed during each polar pass. The three fast-latitude scans occurred approximately 6 years apart and consisted of a nearly full 180 degree latitude scan. These passes transverse the full range of latitudes in about a year, covering both the poles and the ecliptic plane and allowing us to study all types of solar wind on three different occasions: two of the passes occurred during solar minimum (centered around the years 1995 and 2007) separated by a pass which took place during solar maximum (centered around 2001), allowing us to see the changes in the solar wind during maximum and minimum and from solar cycle to solar cycle. To the best of our ability, time-periods of Interplanetary Coronal Mass Ejections (ICMES) have been filtered out of the data due to their well-documented anomalies and transient nature. The ICME list provided by Ebert et al. (2009) was used to eliminate ICME-associated data from this analysis.

2.4. Results

Figure 2.2 shows a scatter plot of the elemental composition and charge state data for pass 1 (1995), plotted against the proton speed. In this figure we show the Fe/O ratio (Panel A), carbon charge state ratio (C^{6+}/C^{5+}) (Panel B), and oxygen charge state ratio (O^{7+}/O^{6+}) (Panel C). Panels B and C show the that as the solar wind speed increases, the charge state ratios decrease, creating a strong anti-correlation. In this figure we see that Ulysses mostly observed the fast solar wind (~750 km s^{-1}) during this period due to the fact that it spends more time at higher latitudes. This solar wind has an average C^{6+}/C^{5+} ratio of around 0.177. There is an exponential relationship between the charge state ratios and the speed of the solar wind (as previously reported by Geiss et al. 1995). Panel A tells a different story. In this panel the Fe/O ratio is used as a proxy for the element fractionation in solar wind plasma because it is the abundance ratio between an element with first ionization potential (FIP) smaller than 10 eV, Iron, and one with FIP greater than 10 eV, Oxygen. The ratio between a low-FIP to a high-FIP element is a tracer of the FIP effect, namely the still not understood enhancement of the abundance ratio of low-FIP to high-FIP elements in the solar corona over the same ratio in the photosphere (e.g. Feldman & Laming 2000 and references therein). The degree of enhancement in the coronal low-FIP/high-FIP abundance ratio is called the "FIP bias" and typically ranges from 1, in the coronal holes, to 3-4 in closed field regions. These abundance anomalies are directly propagated into the solar wind plasma emanating from the corona, so that the ratio in panel A gives an indication of the source region of the wind itself. In panel A the reported photospheric values (log(Fe/O) = -1.33 – Grevesse et al 1998, log(Fe/O) = -1.16 – Asplund et al. 2009) are marked with dotted red lines, along with the reported coronal value (log(Fe/O) = -0.74 – Feldman et al. 1992) marked with a dotted black line. The value of the photospheric abundance ratio is marked by two lines to highlight the range of Fe/O ratio due to the uncertainties in the photospheric abundance of oxygen. We can see in these panels that the fast solar wind has elemental abundances just above photospheric values and that there is no correlation between Fe/O and velocity, as there was with O^{7+}/O^{6+} and C^{6+}/C^{5+}. As the velocity decreases from the fast solar wind value of approximately 750 km s^{-1}, the Fe/O ratio remains at near photospheric values until around 500 km s^{-1}. At this point the Fe/O ratio starts to increase to higher values. It is interesting to note that this is not a systematic increase as is seen in the ion charge states of oxygen and carbon. Although the mean Fe/O ratio does increase for speeds below 500 km s^{-1} there are still values with near photospheric abundances even at the lowest speeds. If we interpret the Fe/O ratio alone as a tracer of the source region, panel A shows that the wind with speeds greater than 500 km s^{-1} comes from the same source region even if its charge state ratios change systematically. On the contrary, the coexistence of Fe/O ratios spanning a factor of 3 in the wind with velocity less than 500 km s^{-1} indicates that this wind could come from multiple source regions that may include the same source region as the fast wind, as well as a multitude of other different sources with FIP bias ranging from 1 to around 3. The variability of the FIP bias in wind streams slower than 500 km s^{-1} could be due to the portion of this wind with Fe/O ratio larger than fast wind value coming from plasma initially confined in closed magnetic loops in the corona, which are opened up by reconnection (e.g. Fisk 2003 and Antiochos et al. 2011). This scenario is supported by two facts:

1. The FIP bias in the wind slower than 500 km s^{-1} is consistent with values routinely reported in spectroscopic measurements (Feldman & Laming 2000, Feldman et al. 2005).
2. The variability of this FIP bias is consistent with variability of this parameter in the corona, which has been suggested to be due to the varying age of coronal loops (Widing & Feldman 2001).

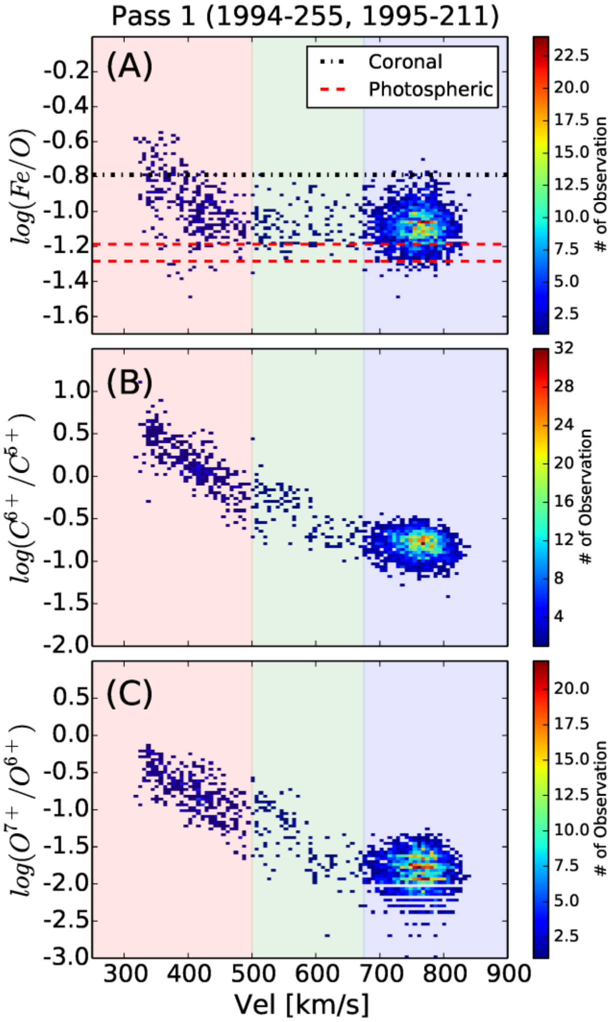

Figure 2.2: Compositional properties during the first Ulysses fast latitude scan. This pass occurred around the 1996 solar minimum. The highlighted colors in the background of the plots indicate the different types of solar wind: slow [red], boundary [green], fast [blue]. Panel A shows the winds Fe/O ratio. In this panel the red dotted lines indicates the measured photospheric values for this ratio and the black dotted line shows the observed coronal value. Panel B shows the C^{6+}/C^{5+} ratio and panel C shows the O^{7+}/O^{6+} ratio (The horizontal strips in the ratio are a data artifact caused by the number of significant digits reported and the logarithmic spacing of the histogram). As the velocity of the solar wind increases the charge state ratio decreases exponentially. The compositional ratio (Fe/O) only shows a divide in its behavior with respect to the proton speed at 500 km s^{-1}.

The wind streams with intermediate speeds between the fast and slow wind seen in this figure (500 km s^{-1} – 675 km s^{-1}, highlighted in green) cannot be characterized with the standard signatures as either fast or slow solar wind since they have a combination of the characteristics of both wind types. This wind has intermediate values of both velocity and charge states, slower and more ionized than fast solar wind, but has elemental composition similar to the fast wind. This indicates that this wind likely originates from the same plasma as the fast solar wind, but undergoes less acceleration, as well as more ionization leading to an increase in the charge state ratios. In this section we argue that this wind is a subset of the fast wind that originates from inside coronal holes, yet near the boundary, leading us to name it the boundary wind.

Figure 2.3 has identical panels as Figure 2.2 but is measured six years later during solar maximum. Here the statistics in the slow wind are enhanced because the slow wind is found at a much larger range of latitudes due to increased inclination and warping of the current sheet during solar maximum. In this figure we can see the same trends that were pointed out in Figure 2.2. Both of the charge state ratios (Panels B and C) show an exponential dependence on speed, while the elemental compositional parameter (Panel A) shows near photospheric values for speeds above 500 km s^{-1}. Figure 2.4 is again similar to Figures 2.2 and 2.3 but is measured six years later during the next solar minimum. This figure also shows the same trends as Figures 2.2 and 2.3, indicating that the main compositional properties of the solar wind and their dependence on wind speed do not change along the solar cycle.

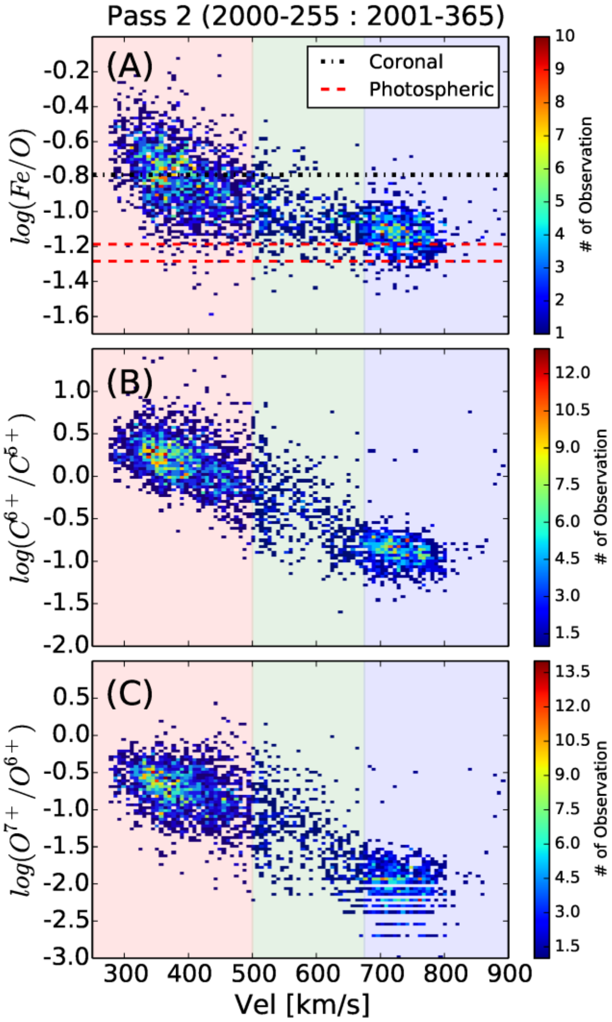

Figure 2.3: Compositional properties during the second Ulysses fast latitude scan. This figure is the same as Figure 2.2 but occurring 6 years later during the 2001 solar maximum. The same trends seen in Figure 2.2 are seen here.

From the results shown in panel A of Figures 2.2-2.4 we argue that the distribution of the Fe/O ratio for the wind between 500 km s^{-1} and 675 km s^{-1} is similar to that found in wind streams faster than 675 km s^{-1}. Figure 2.5 shows the distribution for Fe/O ratio for pass 2 (corresponding to panel A in Figure 2.3). This figure separates the data into 3 panels: the slow wind (panel A) corresponding to the Fe/O ratio below 500 km s^{-1} (red highlighted area in Figure 2.3), the fast wind (panel B) corresponding to the Fe/O ratio above 675 km s^{-1} (blue highlighted area in Figure 2.3), and the boundary wind (Panel C) corresponding to the Fe/O ratio between 500 km s^{-1} and 675 km s^{-1} (green highlighted area in Figure 2.3). The curves on these 3 panels (red) are Gaussian fits of the data. The red line indicates the mean in log space and the error bar shows one standard deviation from the mean in log space. In this figure we can see that the distribution of the data in panels B and C is very similar to each other and distinctly different than that of panel A. Although the mean of panels B and C are not identical this is not unexpected. Panel C has a slight tail at higher Fe/O ratio most likely caused by capturing some slow solar wind values in the 500 km s^{-1} to 675 km s^{-1} range. This speaks to the nature of this lower boundary (at 500 km s^{-1}) being highly dynamic. Without this variability of this boundary, the mean would shift even closer to the fast solar wind value seen in panel B.

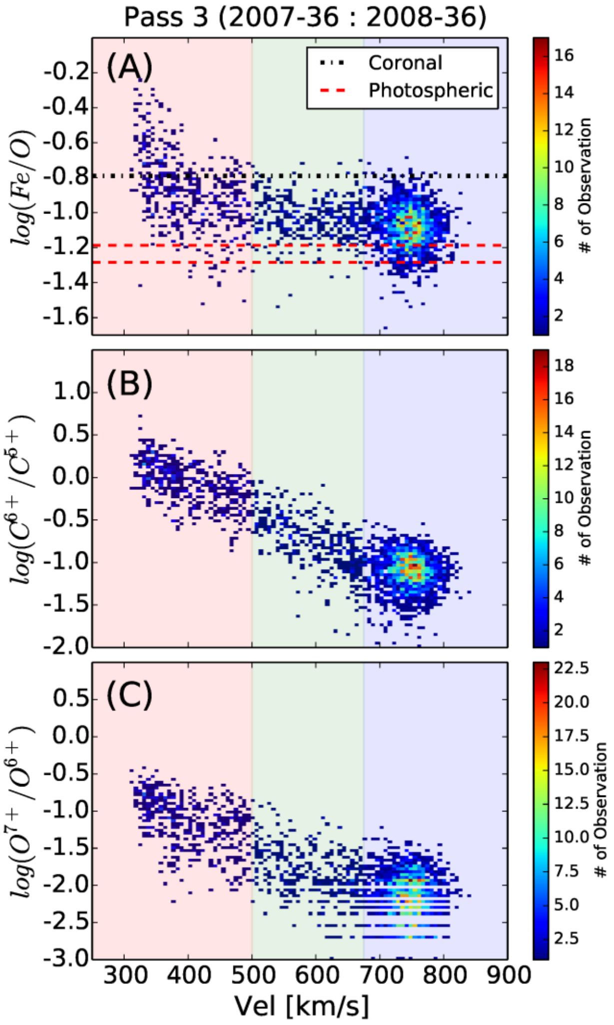

Figure 2.4: Compositional properties during the third Ulysses fast latitude scan. This figure is the same as Figure 2.2 but occurring 12 years later during the 2007 solar minimum. The same trends seen in Figure 2.2 are seen here, indicating that the properties seen in the figure are not solar cycle dependent.

The kinetic properties of the solar wind provide a wealth of information along with the element compositional properties. In order to further solidify the similarities between the boundary wind and the fast wind, the differential velocity, temperature ratio, and entropy of the passes were analyzed. All three of the fast latitude scan passes were summed to generate Figure 2.6. This was done to allow for sufficient statistics for both the fast and slow wind. In these panels the data has been filtered to only include intervals with nearly radial magnetic field, as differential velocity is most accurately estimated in this configuration (for details, refer to von Steiger and

Zurbuchen 2006). We require intervals to have a magnetic field persistent within 30 degrees of radial for over 66 % of the time. Panels A and C show the differential streaming of heavy ions in the solar wind, as indicated by the difference between the alpha and proton speeds and the difference between the O^{6+} and the proton speed, as a function of solar wind velocity. This differential velocity has been theorized to be a result of wave particle interaction (Isenberg and Hollweg 1983). As the solar wind is accelerated the heavier ions are accelerated preferentially up to an Alfvén speed faster than the protons (Marsch et al. 1982a). In these panels we can see that there is an average of a 20 km s^{-1} velocity difference between protons and alphas (Panel A) in the fast solar wind (highlighted in blue). This same velocity difference is seen between O^{6+} and protons (Panel C). In the slow solar wind (highlighted in red), the differential velocity is much smaller, indicating that the governing process in this wind is different from fast, coronal associated wind. The differential streaming of the boundary wind (highlighted in green) is nearly identical to that of the fast solar wind, consistent with the boundary wind and the fast wind both being heated and accelerated by the same process. Panel B in Figure 2.6 shows the O^{6+} to proton temperature ratio. This panel shows that for the fast solar wind (highlighted in blue) the temperature of the wind is near mass proportional, with the O^{6+} kinetic temperature being 16 times that of the proton kinetic temperature (the red dotted line indicates mass proportional temperature ratio). At speeds larger than 500 km s^{-1} the solar wind temperature ratio is nearly mass proportional, while below 500 km s^{-1} the ratio drops toward equal temperature. This change in the temperature ratio occurs at the same speed that the change in the elemental composition and differential velocity occur. The temperature ratio of the boundary wind (highlighted in green) is the same as the fast wind (highlighted in blue).

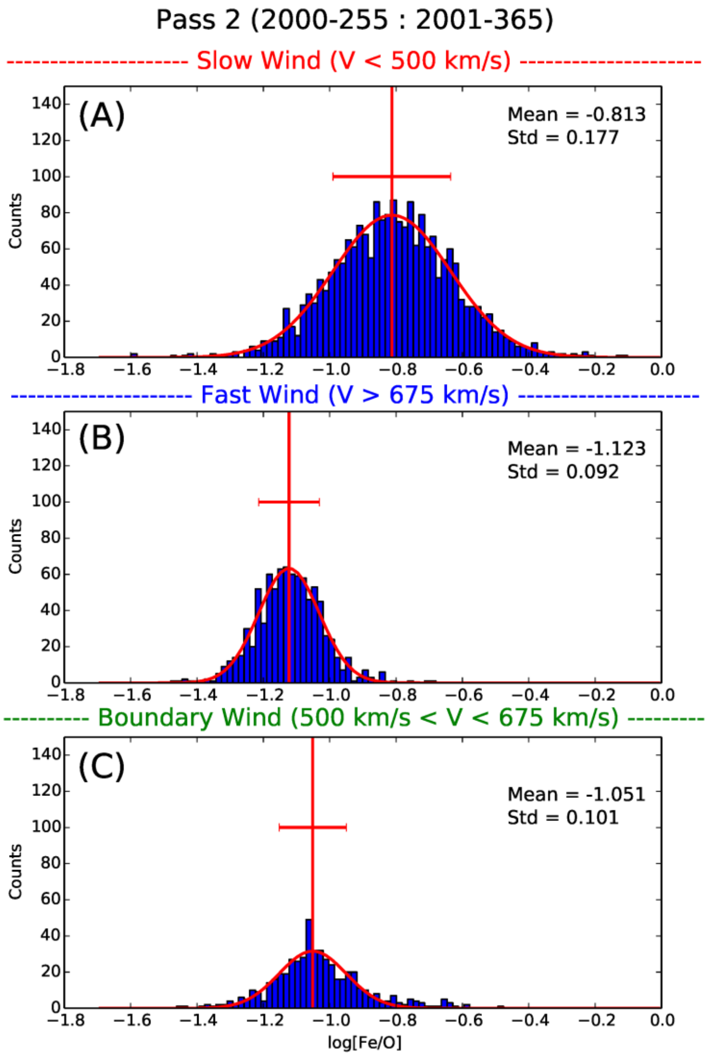

Figure 2.5: Distribution of Fe/O ratio for the second pass: 2000-255 -- 2001-365. Panel A shows the Fe/O ratio for all values slower than 500 km s^{-1}. Panel B shows the Fe/O ratio for all values faster than 675 km s^{-1}. Panel C shows the Fe/O ratio for all values between 500 km s^{-1} and 675 km s^{-1}. The curves plotted over the data (red) are Gaussian fits. The red line indicates the mean of the distribution in log space and the error bars correspond to one standard deviation away from the mean in log space. The distribution of the Fe/O ratio for the boundary wind (Panel C) is nearly identical to that of the fast wind (Panel B) and distinctly different than the slow wind (Panel A).

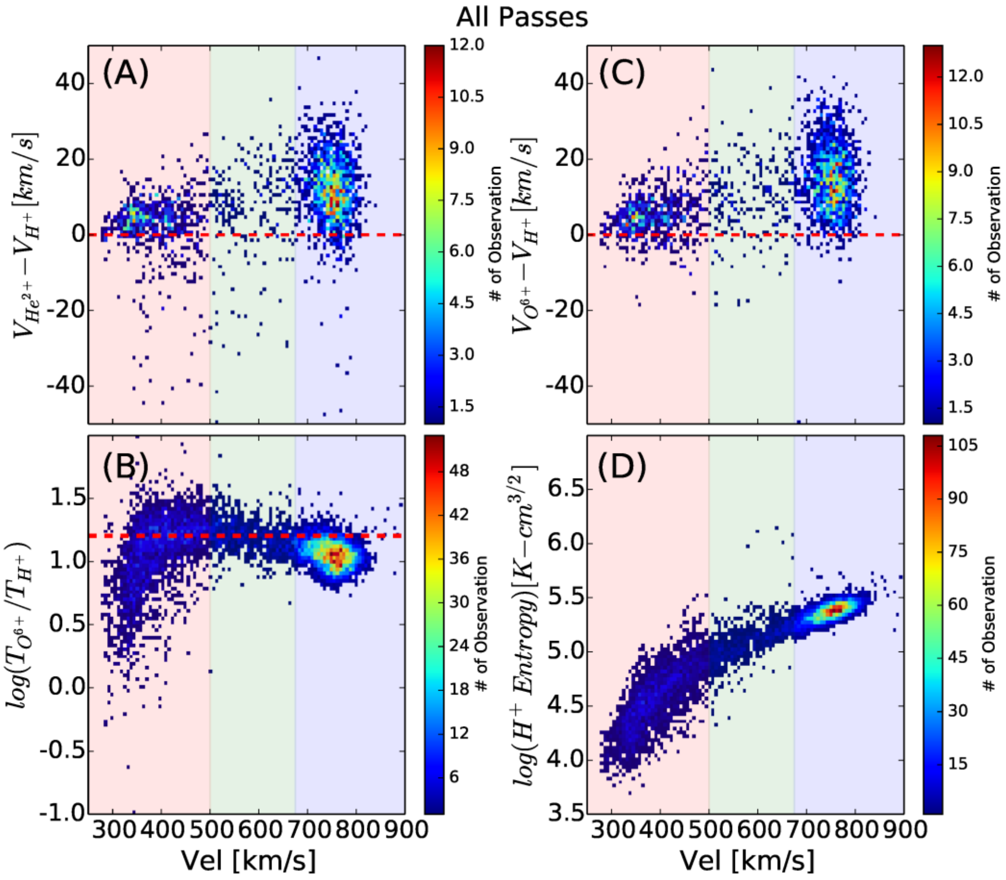

Figure 2.6: Kinetic properties for all of the Ulysses fast latitude scan. Panel A shows the proton to alpha velocity difference. Panel C shows the O^{6+} to proton velocity difference. Both panel A and C filter the data to only include measurements that were taken over 66% of the time within 30 degrees of the magnetic field being parallel to the radial direction. The red dotted line in panels A and C indicate no velocity difference. Panel B shows the temperature ratio between O^{6+} and protons. The red dotted line in panel B indicates a mass proportional temperature ratio. Panel D shows the proton entropy ($T/n^{1/2}$). The highlighted colors in the background of the plots indicate the different types of solar wind: slow [red], boundary [green], fast [blue]. Panels A and C show the differential streaming between the protons and heavy ions are different in the slow wind ($V < 500$ km s^{-1}) than wind with velocity greater than 500 km s^{-1}. This same break in the properties of the wind at 500 km s^{-1} can also be seen in the temperature ratio [Panel B] and entropy [Panel D]. This point also corresponds to the compositional distinction point seen in Figures 2.2-2.4.

Panel D shows the specific entropy of the solar wind. The specific entropy of the solar wind is given by the formula $T/n^{\gamma-1}$, where T is the proton kinetic temperature and n is the density of the plasma. The polytropic index, γ, of the solar wind has previously been calculated by Totten et al. (1995) using the Helios 1 data and found to have a value of $\gamma=1.46\pm0.04$. This value is usually rounded to 1.5 (e.g. Burton 1999, Pagel 2004) leaving us with $T/n^{1/2}$. Typically the specific entropy of fast streams are higher than that of slow streams (Siscoe and Intriligator 1993). Numerous studies have looked into the correlation between the specific entropy of the solar wind and compositional ratios, specifically O^{7+}/O^{6+} (e.g. Burton 1999, Crooker and McPherron 2012). Pagel (2004) finds that there is a high correlation between the specific entropy and the O^{7+}/O^{6+} ratio outside of ICMEs and that the proton specific entropy is a reliable indicator of stream structure outside of solar maximum. In panel D of Figure 2.6 we use the entropy to study the differences in the solar wind types. Here we can see that there is a narrow range of observed specific entropy within the fast solar wind around 250,000 K $cm^{3/2}$ and that this value follows an exponential dependence with solar wind velocity down to 500 km s^{-1}. Below 500 km s^{-1} the entropy deviates from this exponential dependence and steepens. The trend seen in this plot further exemplifies the similarities between the boundary wind and the fast solar wind and how they differ from the slow solar wind.

2.5. Discussion

The observed O^{7+}/O^{6+} and C^{6+}/C^{5+} ratios and the kinetic properties of the boundary solar wind indicate that there is a continuum of charge states that range from the slowest to the fastest speeds. The elemental composition data, on the other hand, highlights a distinct difference of origin in the wind at speeds below 500 km s^{-1} and the wind at speeds above 500 km s^{-1}. This distinction is further reinforced by the differences in the differential streaming, the entropy, and the ratios of the observed kinetic temperatures of oxygen and protons. Thus, during the observed time-periods, there is a third type of wind - a boundary wind - between high-latitude fast (i.e. $v > 675$ km s^{-1}) and slow (i.e. $v < 500$ km s^{-1}) wind. We have shown that the fast wind and boundary wind have similar elemental composition, differential streaming, oxygen to proton temperature ratio, and entropy slope vs. speed. The similarities in these two types of wind lead us to believe that they originate from similar source regions and are heated and accelerated by the same mechanism near the Sun. The slow solar wind, on the other hand, is distinguishable from both the boundary and high-latitude fast wind: Slow wind has little to no differential streaming, has a completely different oxygen to proton temperature profile and is compositionally distinct from the rest of the solar wind, indicating that it likely originates from a different source and is accelerated by a different mechanism.

One possible explanation for the increased charge state ratios of the boundary wind over that of the fast wind is that the magnetic field near the boundary of coronal holes expands more than that of the magnetic field at the center. Yet, the boundary wind is a subset of the fast solar wind that undergoes a significantly different expansion history than high-latitude fast wind, altering its ionic charge states and also observed solar wind speed and kinetic temperature. This expansion argument aligns with previous work done by flux-tube expansion (e.g. Wang et al. 2009 and references therein). This expansion leads to slower speed wind everywhere along the wind path. This slower speed results in more ionization to occur leading to increased charge states. The more expanded the flux tubes are, the greater the velocity decrease would be, resulting in a continuum of charge state ionization from the barely expanded flux tubes near the center of coronal holes to the extremely expanded flux tubes at the edges. However, this process would not change the elemental composition of the plasma and would result in wind that has higher charge states and the same Fe/O ratio as the fast solar wind.

2.6. Conclusion

Several theories exist to explain solar wind heating and acceleration, including: gradients in the Alfvén wave pressure, electric field acceleration due to electron charge separation and magnetic reconnection. In this chapter we argue that it is possible for multiple methods to be active in the solar corona. The fast and boundary winds are two manifestations of the same type of wind originating from coronal holes and are heated and accelerated by the same process. However, the boundary wind originates closer to the boundary of the coronal hole, and therefore undergoes more expansion, leading to different wind speeds, electron temperatures, and densities at the foot points of coronal holes. As a consequence, this wind is compositionally very similar to the fast wind but has a lower velocity and increased ionization of heavy ions.

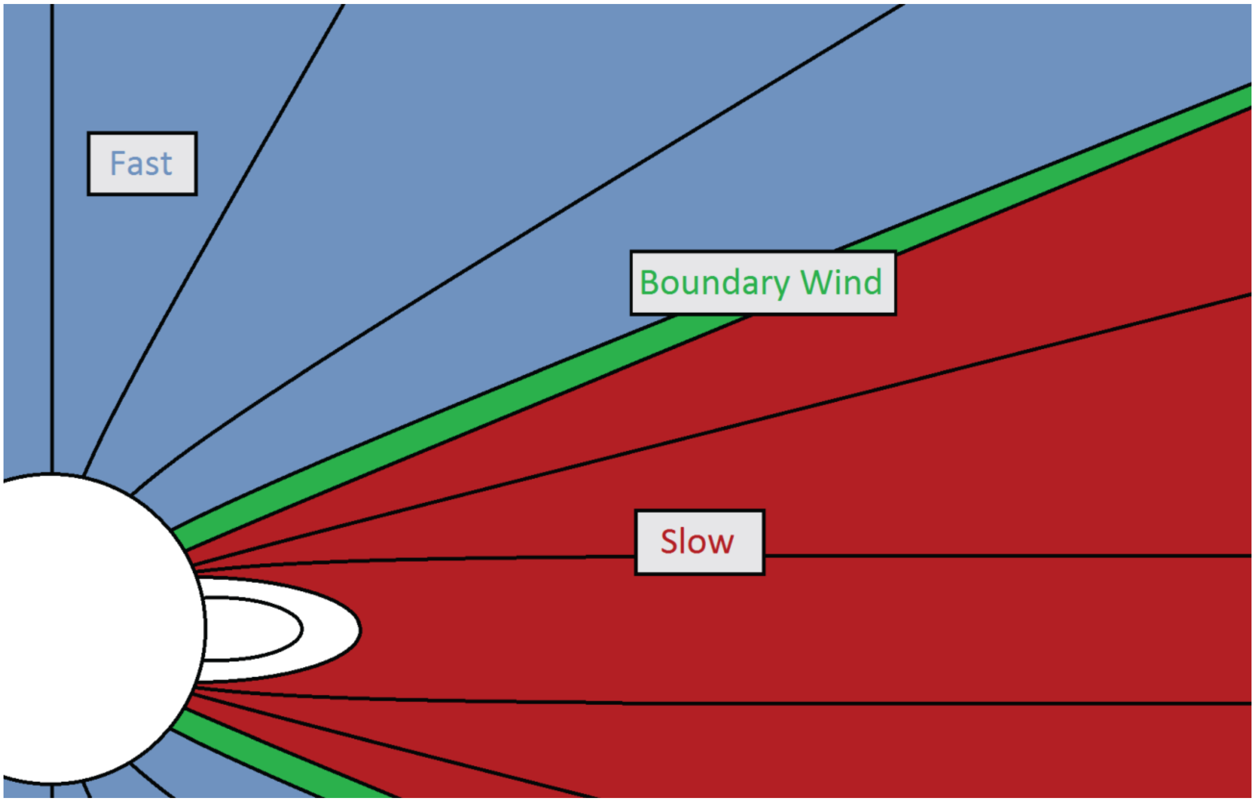

Figure 2.7: Diagram of the solar wind. The fast solar wind (blue) originates from the open magnetic field near the poles. The slow wind (red) originates from magnetic reconnection of closed coronal loops at the boundary of large scale streamers. The boundary wind (green) originates from open field lines near the boundary between coronal holes and streamers. It is to be noted that there is no sharp transition between the fast wind and the boundary wind, as the speed and charge state composition of the former gradually approach those of the latter as the wind footpoint locations are closer to the coronal hole/streamer boundary.

A more complete picture of the solar wind can be made using these results. In order to relate these findings to earlier work, Figure 2.7 shows a simplified picture of the Sun and the solar wind streaming from it. In this picture there exists 3 types of wind: slow, fast, and boundary wind. The slow wind (red) corresponds to the wind with speed lower than 500 km s^{-1}, likely produced by magnetic reconnection of closed and open field lines at the boundary between coronal holes and closed field regions. This interpretation of the slow wind is consistent qualitatively with Fisk 2003 and Antiochos 2011. This wind originates from regions with high electron temperature and density resulting in more ionization of heavy ions. The fast solar wind (blue) originates from open magnetic field lines near the poles. This wind has lower charge states and ionization, higher speeds, and nearly photospheric elemental composition values. Finally we have the boundary wind (green) that originates from the edge of coronal holes; it is important to note that there is not a sharp divide between the fast and the boundary winds, as the speed and charge states of the former slowly and gradually change into those of the latter. This wind has an elemental composition identical to the fast solar wind but has decreased velocity and increased ionization, leading to a continuum of velocity and charge states between the fast and slow solar wind.

CHAPTER III

On Solar Wind Origin and Acceleration: Measurements from ACE

This chapter is taken from Mark Stakhiv, Susan T. Lepri, Enrico Landi, Patrick Tracy, and Thomas Zurbuchen (2016), *Astrophysical Journal, 829*, doi: 10.3847/0004-637X/829/2/117

3.1. Abstract

The origin and acceleration of the solar wind are still debated. In this chapter we search for signatures of the source region and acceleration mechanism of the solar wind in the plasma properties measured in-situ by the Advanced Composition Explorer (ACE) spacecraft. Using the elemental abundances as a proxy for the source region and the differential velocity and ion temperature ratios as a proxy for the acceleration mechanism, we are able to identify signatures pointing toward possible source regions and acceleration mechanisms. We find that the fast solar wind in the ecliptic plane is the same as that observed from the polar regions and is consistent with wave acceleration and coronal hole origin. We also find that the slow wind is composed of two components: one similar to the fast solar wind (with slower velocity) and the other likely originating from closed magnetic loops. Both components of the slow solar wind show signatures of wave acceleration. From these findings we draw a scenario that envisions two types of wind, with different source regions and release mechanisms, but the same wave acceleration mechanism.

3.2. Introduction

Traditionally, the solar wind has been divided into two separate components by velocity: the fast wind with velocity greater than 600 km s^{-1} and the slow wind with velocity slower than 500 km s^{-1} (Zurbuchen 2007, and references therein). These two winds are thought to originate from different sources on the Sun, and they have very different properties, reflecting their respective source and acceleration profiles. For example, the charge state ratios of C^{6+}/C^{5+} and O^{7+}/O^{6+} are inversely correlated with wind speed (Geiss et al. 1995). Consequently, the coronal electron temperatures inferred from the O^{7+}/O^{6+} charge state ratios are very different in the two winds. There are also important solar cycle-dependent changes to the charge state distributions of several elements. The magnitude of the change in charge state distribution is different for winds belonging to different velocity classes (Lepri et al. 2013). The fast and slow solar wind also exhibit large differences in the relative abundances of heavy elements. In particular, the fast solar wind's elemental abundance ratios measured in-situ reflect values remotely observed in the photosphere of coronal hole regions (Geiss et al. 1995). This characteristic suggests that the fast solar wind escapes along open field lines where processes do not significantly modify the elemental abundances of the plasma during its release from the source. The slow solar wind, on the other hand, has been shown to exhibit enhanced abundance ratios, relative to photospheric measurements, of elements with low first ionization potential (FIP < 10 eV) compared to elements with high FIP (FIP > 10 eV) (Geiss et al. 1995). This enhancement is called the "FIP effect," and has long been observed remotely on closed magnetic field structures (magnetic loops) filling the quiescent and active solar corona (Laming & Feldman 2003; Feldman & Laming 2000, and references therein). The similarity between the slow wind elemental abundances and elemental abundances on closed coronal loops suggest a common origin for the slow solar wind (Feldman et al. 2005 and references therein). These loops are generally located near the streamer belt and presumably feed the slow wind, which is confined to 15° around the heliospheric current sheet (Schwenn 2006).

While coronal holes are accepted to be the source of the fast wind (see, e.g., McComas et al. 2003), the source of the slow wind remains under debate. However, the acceleration process for both the fast and slow wind is still unknown. Two groups of theories have been put forth to explain the origin and acceleration of the slow solar wind.

The first group of theories deals with the acceleration of the solar wind and assumes that the solar wind at all speeds propagates along the open magnetic field inside coronal holes. The basic assumption common to all theories in this group is that the solar wind is accelerated by Alfvén wave pressure gradients and is heated by Alfvén wave dissipation (e.g., van der Holst et al. 2014, and references therein). The Alfvén waves are generated by magnetic field fluctuations that are then reflected by density gradients, producing counter-propagating waves (e.g., Leroy 1980; Matthaeus et al. 1999; Cranmer 2010). These counter-propagating waves then cause a turbulent cascade that releases energy, thus heating the solar wind (Velli et al. 1989). The slower solar wind originates from the boundaries of coronal holes, where the magnetic field expansion is larger than at the coronal hole center. The larger magnetic field expansion creates a plasma that is slowed down consistent with mass conservation and flux tube expansion. This slower plasma, ejected from the edge of coronal holes, spends more time in the inner corona, allowing it to be ionized more than the fast wind coming from coronal hole centers. This theory successfully explains the compositional properties of the fast solar wind, but it does not reproduce the coronal elemental composition of the slow wind that is due to the origin of the plasma and not the acceleration processes.

The second group of theories addresses the origin of the slow solar wind. The common assumption is that the slow solar wind is accelerated out of large closed magnetic loops in the corona via interchange reconnection with open magnetic fields (Antiochos et al. 2011; Fisk 2003). In this scenario the solar wind speeds observed in the slow wind depend inversely on the temperature of the material that is involved in the reconnection (Fisk 2003). This theory allows for the generation of a slow wind that has an ionic and elemental composition very similar to that of closed loops and it successfully connects the plasma properties measured through remote sensing and in-situ observations. The intrinsic randomness and patchiness of the reconnection process is expected to drive a more variable wind, as the slow wind is observed to behave. However, this theory is vague at describing how the plasma is accelerated outward once it is released.

The traditional classification for the solar wind delineated by speed, ionization state, and elemental composition is unable to account for all of the wind measured in-situ. For example, solar wind with speeds between 500 km s^{-1} and 600 km s^{-1} lie between the classifications that are typically used. Also, the phenomenological nature of this classification does not provide any information on the source region and acceleration mechanism of the fast and slow winds.

Recently this two-state picture of the solar wind has been revisited in chapter 2 of this dissertation. They searched for signatures of different sources of solar wind using data from the three fast latitude passes completed by the Ulysses spacecraft, and examined the Fe/O ratio, O^{6+}/ H^{+} temperature ratio, alpha-to-proton differential streaming, O^{7+}/O^{6+} density ratio, C^{6+}/C^{5+} density ratio, and proton specific entropy. The proton specific entropy, $\ln(T_p/n^{1/2})$, following Pagel et al. (2004), is a parameter that incorporates the proton temperature, T_p, and the proton density, n. This parameter has been used in the past to find correlations with the solar wind's compositional ratios in stream structures (e.g., Burton et al. 1999; Crooker & McPherron 2012). Here the specific entropy is used to identify the fast and slow solar wind plasmas (e.g., Burlaga et al. 1990).

The analysis performed in chapter 2 revealed that the wind with speeds between 500 and 675 km s^{-1} had nearly photospheric elemental composition and kinetic properties consistent with fast solar wind but higher charge states and slower velocities more akin to that of the slow solar wind. This wind was labeled "boundary wind", as it was found to be consistent with the fast solar wind predicted to originate near the boundaries of coronal holes by Oran et al. (2015). In that model, which belonged to the first group of models discussed above, the boundary wind was predicted to have lower velocities due to the larger expansion of magnetic flux tubes at the coronal hole edges relative to coronal hole centers (see, e.g., Wang & Sheeley 2006). This lower speed causes the plasma to spend more time in the inner corona, where it can be ionized to a greater extent than the faster wind emanating from coronal hole centers. The lack of FIP effect is also consistent with a coronal hole origin of the boundary wind, therefore this wind is interpreted as being coronal hole-associated wind. In chapter 2 we also found that the heavy element composition across all of the solar wind revealed a clear break point at 500 km s^{-1}, above which Fe/O values were closer to photospheric composition, and below which they could span over an order of magnitude. This break point was interpreted as the point above which the slow, streamer-associated solar wind is no longer found. Throughout this chapter, we refer to the wind accelerated from coronal holes (the fast wind) with speed slower than 600 km s^{-1} as “boundary wind”.

The results of chapter 2 raise two major questions. The first question is whether the boundary wind is relegated to higher latitudes only accessible to Ulysses, or whether it can be found close to the ecliptic, as would be observed by the Advanced Composition Explorer (ACE). The second question is whether the boundary wind could potentially extend to speeds below 500 km s^{-1}. If true, the portion of the wind that we traditionally consider as part of the slow wind category is actually a mixture of both wind coming from closed loops and coronal hole wind that has been slowed below 500 km s^{-1}.

In this chapter we address these two questions by leveraging in-situ measurements of the solar wind properties made by the ACE spacecraft in the ecliptic plane and comparing them with results obtained in chapter 2 using Ulysses. In Sections 2 and 3 we describe the methodology and the data used for this analysis, respectively. In Section 4 we examine the compositional and kinetic parameters of the wind slower than 500 km s^{-1}, and search for evidence of different origins and acceleration mechanisms for different types of wind. The resulting measurements, uncertainties, and implications are discussed in Section 5.

3.3. Methodology

The elemental and kinetic properties of the solar wind bear the signatures of the wind’s source regions and acceleration mechanisms. In this work we will use the wind’s elemental, ionic, and kinetic properties to identify the presence of the boundary wind in the ecliptic, and to investigate the questions posed above. In particular, we rely on three main solar wind characteristics to discriminate between different types of wind: the elemental abundance (specifically Fe/O), the differential velocity (between He^{2+} and H^{+} and between O^{6+} and H^{+}), and the ion kinetic temperature ratio ($T_{O^{6+}}/T_{H^{+}}$).

The solar wind’s elemental composition is used to link the plasma back to the source region. Although these parameters are measured in-situ, they allow us to investigate the source region because they do not change once released from the Sun. In particular, the Fe/O ratio is used because it is a measure of a low-FIP element (iron) to a high-FIP element (oxygen) and the FIP ratio of the solar wind differs by source region (see von Steiger & Zurbuchen 2016, and references therein).

The second parameter we use to distinguish between the slow wind and fast/boundary wind is the differential streaming (alpha to proton and O^{6+} to proton). Differential streaming is a by-product of wave acceleration (Cranmer et al. 2008, and references therein), as waves tend to preferentially accelerate heavy ions over protons, causing the heavy ions to travel up to an Alfvén speed faster than the protons. Thus, differential streaming is expected to be present in wind accelerated by waves from coronal holes, provided this wind is sufficiently collisionless (Neugebauer et al. 1996). On the other hand, wind released from coronal loops is expected to have little differential streaming, as all particles leave the Sun with nearly the same speed. Coronal hole wind acceleration is expected to occur in the chromosphere, where it needs to lift the plasma to the corona. This process allows for a longer acceleration time over coronal loop wind and more time to build up a differential velocity. However, plasma released from loops are opened up by reconnection higher up giving the acceleration less time to build up a differential velocity, if waves do accelerate the plasma. In the absence of wave-particle acceleration under sufficiently collisionless conditions, the plasma should remain without differential streaming when observed in-situ (Kasper et al. 2008).

The third parameter we examine is the ion kinetic temperature, which reflects the origin and acceleration mechanism of the associated wind plasma. The ion kinetic temperature probes the plasma’s initial acceleration mechanism because wave-accelerated fast wind is expected to exhibit mass-proportional temperature ratios (e.g., Cranmer et al. 1999; Chandran 2010; Kasper 2013; Khabibrakhmanov & Mullan 1994). Plasma originally on closed loops are expected to have temperatures closer to equilibrium, i.e. equal temperatures, in the absence of wave acceleration. This temperature ratio is dependent on the acceleration of the plasma at the source region, in particular the dissipation of Alfvén waves cascading to higher frequencies. The plasma temperature ratio measured in-situ is the result of the interplay between plasma heating during acceleration and cooling by Coulomb collisional relaxation (Tracy et al. 2015).

The data analysis tools used here have some important limitations. First, the amount of increase in the low-FIP/high-FIP ratios is not constant, but has been found to depend on the age of the loop (Widing & Feldman 2001). In this case, low Fe/O values can in principle also be due to slow wind released from newly formed loops, making it difficult to draw a firm conclusion about the source on a case-by-case bases (see, von Steiger & Zurbuchen (2016) for variability). Second, loops reaching large heights in the solar corona can have a density low enough to limit ion heat conduction. In these cases, coronal heating models based on Alfvén waves also predict ion temperatures close to mass proportional toward the top of these loops before reconnection releases their plasma into the solar wind (van der Holst et al. 2014). This may challenge a simple interpretation of ion temperatures to identify signatures of Alfvén wave acceleration in the solar wind. Third, and most importantly, both differential velocities and ion temperatures in the solar wind are significantly affected by Coulomb collisions. Coulomb collisions drive the plasma toward equal bulk speeds and the same temperature, changing the signatures imparted on the plasma by the Alfvén wave heating and acceleration process (Maruca et al. 2011). The impact of these three limitations (loop age, loop dimension, and Coulomb collisions) on our results will be discussed in Section 5.

3.4. Observations

The data used for this analysis were obtained from two different instruments on board the ACE spacecraft, launched in 1997 and providing nearly continuous measurements of the solar wind at L1 from 1997 through the present. Onboard sensors provide measurements of solar wind composition, plasma characteristics, and magnetic field, as well as other quantities not utilized in this study. The heavy ion and proton composition data used were part of the latest release of the Solar Wind Ion Composition Spectrometer (SWICS) data set, reprocessed and expanded by Shearer et al. (2014). The magnetic field data were obtained from the Magnetometer (MAG) instrument. These two data sets are available at the ACE Science Center at http://www.srl.caltech.edu/ACE/ASC/. Interplanetary Coronal Mass Ejections (ICMEs) have been removed using the Richardson & Cane (2010) list, including an additional six hours before and after the begin/end date of each event in the list to eliminate potential biasing of our analysis due to the presence of unusual charge states and elemental compositions associated with ICMEs (see Zurbuchen & Richardson (2006) for more information). Any additional interplanetary ejecta that may have escaped the Richardson & Cane catalogue contribute negligibly to the results presented here.

3.5. Results

3.5.1.Boundary Wind near the Ecliptic

In order to test whether the boundary wind is present in the ecliptic we selected ACE/SWICS data spanning a two-year time period between 2007 January 1 and 2008 December 31, during the minimum of solar cycle 24. We restrict our analysis to this period as a compromise between the competing needs of maximizing statistics and minimizing the effects of the solar cycle, which are known to cause composition values to change over time (Lepri et al. 2013). The two-year period during solar minimum was chosen because it coincided with one of the fast latitude passes used in the previous study. However, the results of this study are the same regardless of the two-year period we consider.

Figure 3.1 shows the solar wind elemental and charge state composition as a function of proton speed as a 2D histogram. This figure organizes the results in the same way as in chapter 2, where we used Ulysses/SWICS to study the boundary and fast solar wind at all latitudes. This figure is highlighted with three colors to point out the three velocity ranges: the red section ($V < 500$ km s^{-1}) highlights the slow solar wind; the green section (500 km s^{-1} < V < 675 km s^{-1}) highlights the boundary wind (again, a subset of the fast solar wind); and the blue section ($V > 675$ km s^{-1}) highlights the fast solar wind. The color scale shows the number of measurements in a given bin. Figure 3.1A shows the Fe/O ratio, Figures 3.1B and 3.1C show two charge state ratios (C^{6+}/C^{5+} and O^{7+}/O^{6+}, respectively). Figures 3.1B and 3.1C show the well known anticorrelation between solar wind speed and charge state ratio, as discussed by Geiss et al. (1995). However, Figure 3.1A does not show this same clear anticorrelation, but rather that the Fe/O ratio values are confined to a relatively narrow range of values at speeds larger than 500 km s^{-1}, while below that velocity the Fe/O ratio spreads over almost one order of magnitude (similar to what was found in chapter 2).

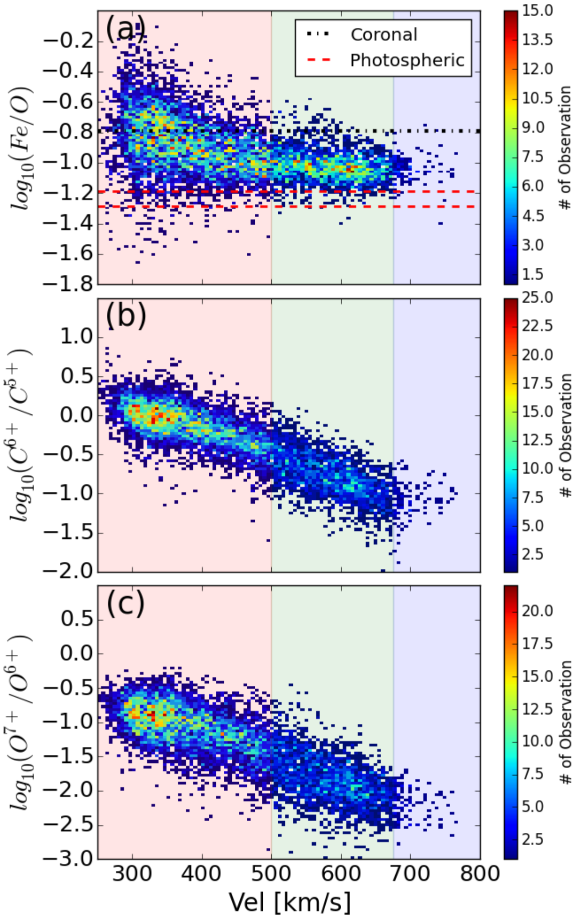

Figure 3.1: ACE/SWICS measurements of the solar wind composition and charge state properties for 2007-2008. (a): Fe/O ratio; the red dotted lines show the measured photospheric values for this ratio (Grevesse & Sauval 1998; Asplund et al. 2009) to indicate a range of values due to the uncertainties in the photospheric oxygen abundance. The black line marks the coronal value (Feldman 1992). (b) C^{6+}/C^{5+} density ratio. (c) O^{7+}/O^{6+} density ratio. This plot shows an anticorrelation between the solar wind velocity and the charge state ratios. This anticorrelation is not seen in the Fe/O ratio. This plot shows similar results to that in chapter 2.

Figure 3.2 shows the plasma kinetic properties of the solar wind over this same time period. This figure is organized in the same way as in chapter 2 and the velocity space is divided into the same three parts as Figure 3.1. Figure 3.2 shows the differential velocity ((a): alpha to proton, and (b): O^{6+} to proton), (c) the O^{6+}-to-proton temperature ratio, (d) and the proton entropy. In (a) and (b) the differential velocity was calculated by using the measured heavy ion velocity ((a): He^{2+}; (b): O^{6+}) and correcting for the magnetic field angle (following Berger & Wimmer-Schweingruber 2011). The red dotted line in (a) and (b) indicate zero differential velocity. In (c) the temperature ratio of the fast wind and boundary wind are approximately independent of speed and slightly above mass proportional heating (marked by the red dotted line). On the other hand, in the slow wind this ratio is strongly dependent on the speed, and approaches unity (that is, equal temperatures) at the lowest speeds. Still, even at the lowest speeds a sizable fraction of the wind has ion temperature ratio values at, or close to, mass proportional. In (d) the entropy value for both the fast and boundary wind exponentially decreases with velocity at a fixed rate, while in the slow wind the rate increases. Thus Figure 3.2 confirms the wind classification proposed in chapter 2, and extends it to ACE measurements in the entire 1998-2011 period: namely, between 500 and 675 km s^{-1} the solar wind consists of a subset of wind accelerated from coronal holes, with the same origin and acceleration mechanisms as the true fast wind, whose speed is lower because it is accelerated from the coronal hole boundaries.

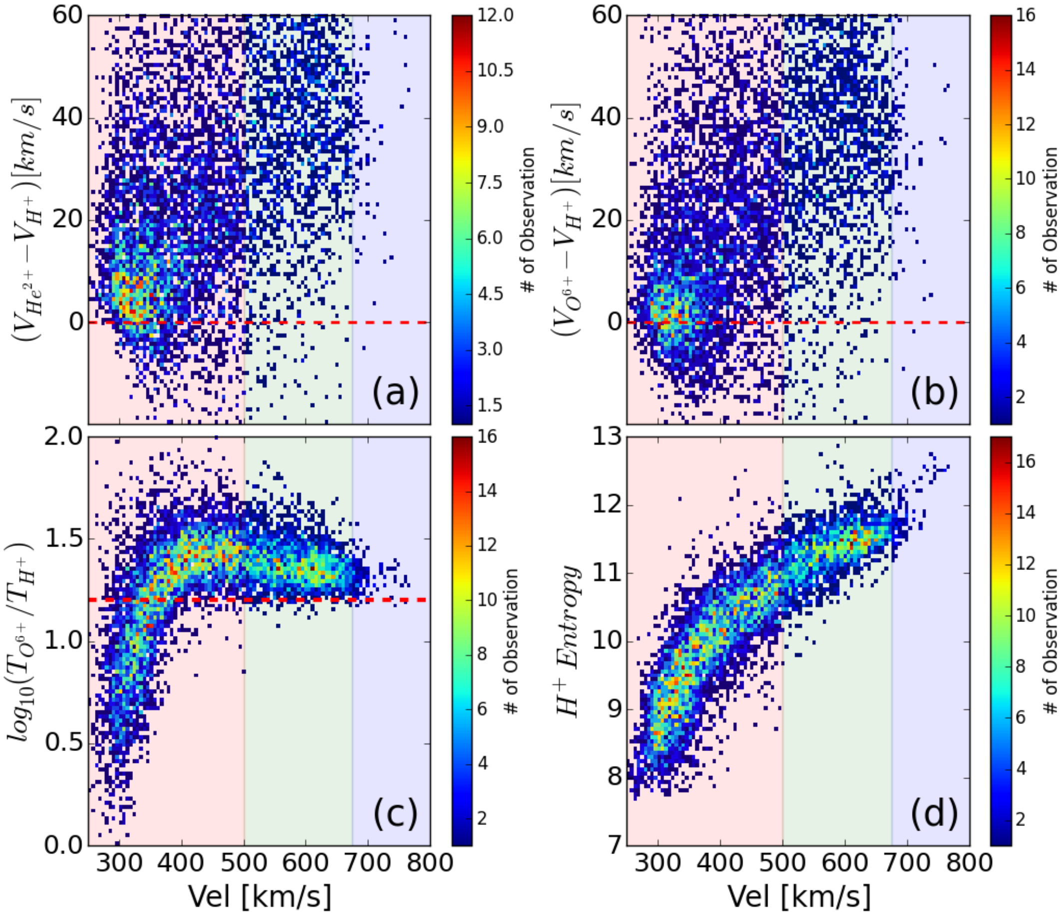

Figure 3.2: ACE/SWICS measurements of the solar wind kinetic properties for 2007-2008. (a) He^{2+}-proton differential velocity. (b) O^{6+}-proton differential velocity. In these 2 panels the velocities are corrected for the angle of the magnetic

field (following Berger & Wimmer-Schweingruber (2011)). (c) O^{6+}/proton temperature ratio. (d) Proton specific entropy (here the H^+ Entr. quantity is the natural log of the temperature divided by the square root of the density divided by 1 $K/cm^{3/2}$). This figure shows distinct changes in the behavior of the solar wind when the 500 km s^{-1} velocity threshold is crossed.

3.5.2. Properties of the Wind Slower Than 500 km s^{-1}

Figures 3.1 and 3.2 also suggest that the slow solar wind (V < 500 km s^{-1}) could be composed of two parts: wind released from closed loops via magnetic reconnection, and a small population of coronal hole wind traveling at speeds slower than 500 km s^{-1} that can be identified by its low Fe/O ratio, higher differential streaming, and higher temperature ratio. To investigate whether the slow wind consists of these two populations, we examine the data using the Fe/O ratio, the ion temperature ratio, and the differential velocity.

The first parameter we study is the Fe/O ratio, which can be taken as a proxy for the source region of the wind plasma — coronal holes (low, near photospheric Fe/O values), or coronal loops (higher than photospheric Fe/O values). Figure 3.3 shows the slow solar wind properties divided into three classes of Fe/O ratios. This figure is split into 4 columns (highlighted by the background colors red, orange, green, and white). Columns 1-3 (red, orange, and green) show all the wind with velocity less than 500 km s^{-1} and further filtered by different Fe/O ratios. For reference, column 4 (white) corresponds to all the solar wind with velocity greater than 500 km s^{-1}. The rows show the different properties of the solar wind within those specific filters: (a) Fe/O , (b) alpha-to-proton differential velocity (with the red dotted line marking the zero differential velocity point), (c) and O^{6+}/H^+ temperature ratio (with the red line marking the mass proportional temperature ratio), (d) proton density, and (e) entropy . If the slow solar wind is a mix of the two wind types — the boundary wind coming from coronal holes with low Fe/O ratio values, and wind coming from closed loops with high Fe/O values — we should be able to see differences in these properties in the three Fe/O wind classes shown in Figure 3.3. In fact, the wind coming from coronal holes is expected to have high temperature ratio and differential velocity if not erased by Coulomb collisions, while the wind coming from coronal loops should have equal temperatures and no differential velocity.

The high Fe/O ratio wind (Column 1) is confined to the lowest velocity values and it has low ion temperature ratios, as expected from a wind released by closed magnetic loops close to equilibrium. In the intermediate Fe/O ratio (Column 2), which can be expected to be released from newly formed loops where the FIP effect has not yet completed its elemental fractionation, the ion temperature ratio is close to the mass proportional temperature ratio, and it decreases at lower wind speeds. On the contrary, the ion temperature ratio in the low Fe/O ratio wind (Column 3) has high values above 350 km s^{-1}, consistent with the fast wind, and decreases toward equal temperatures only at the slowest velocities. The differential velocity of all Fe/O classes increases at speeds above 400 km s^{-1}, reaching the values of the slowest fast wind (500-550 km s^{-1} in B4). The lower Fe/O ratio wind has a larger percentage high differential streaming (67% over 10 km s^{-1}) compared to the higher Fe/O ratio wind (55% over 10 km s^{-1}).

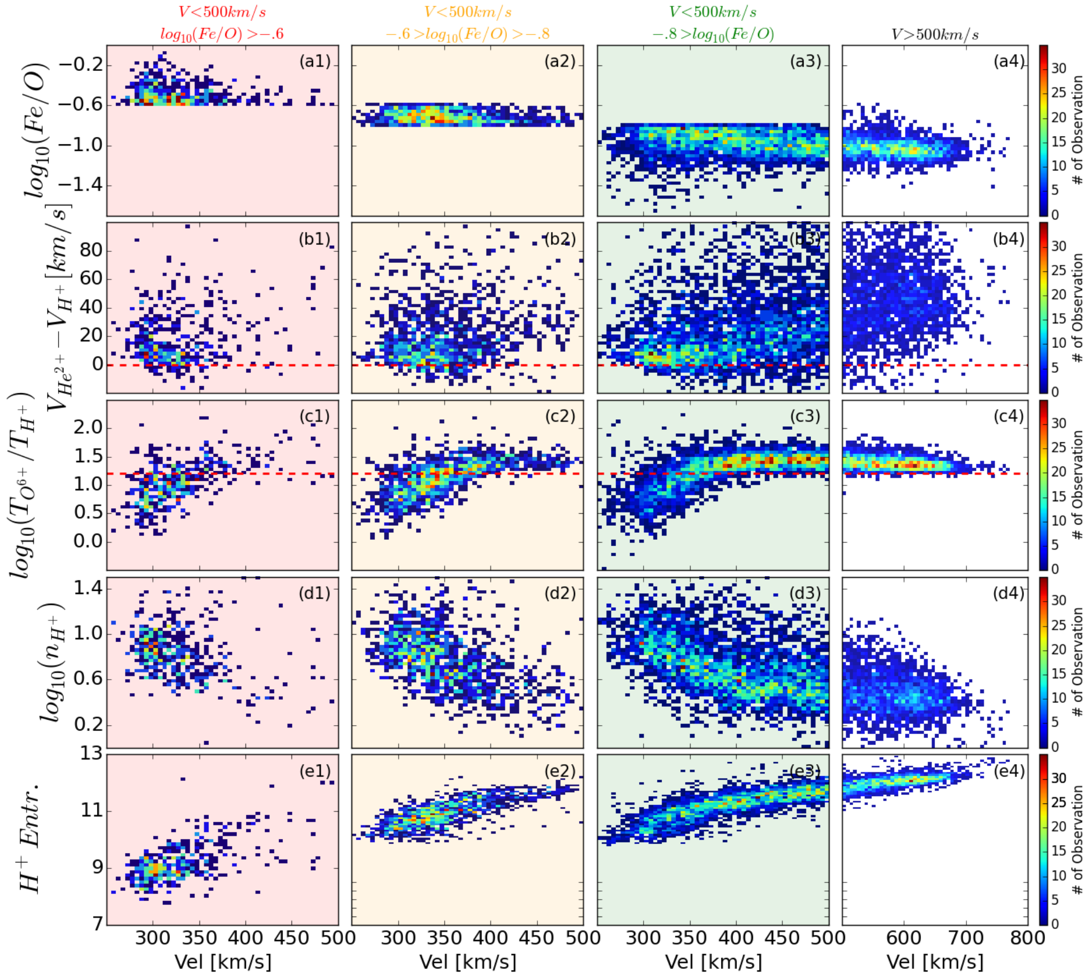

Figure 3.3: Properties of the slow velocity solar wind split by Fe/O ratio. The figure is split into four columns (highlighted by the background colors red, orange, green, and white). Columns 1-3 (red, orange, and green) show the wind with velocity less than 500 km s^{-1} and further filtered by different Fe/O ratio values. Column 4 (white) shows the solar wind with a velocity greater than 500 km s^{-1}. Each row shows a different property of the solar wind within those

specific filters: (a) Fe/O ratio , (b) alpha to proton differential velocity, (c) and O^{6+} to proton temperature ratio, (d) proton density (here the n_{H+} quantity is the proton density divided by 1 cm^{-3}), (e) and proton specific entropy (here the H^+ Entropy quantity is the natural log of the temperature divided by the square root of the density divided by 1 $K/cm^{3/2}$).

In all three Fe/O wind classes, it is important to notice that the ion temperature ratio correlates with the plasma density: the higher the density, the lower the ratio. The results in Figure 3.3 can be summarized as follows:

1. High and intermediate Fe/O ratio wind:
    a) Confined to lower speeds and has larger density
    b) Less differential velocity compared to low Fe/O ratio wind
    c) Ion temperature ratio inversely correlated with density, ranging from near unity to mass-proportional values
2. The low Fe/O ratio wind:
    a) Ion temperature ratio values similar to the fast wind, except when the density is highest
    b) More differential velocity than the high and intermediate Fe/O wind

The results of the low (column 3) Fe/O ratio wind can be interpreted with this wind being the extension of the boundary wind to speeds typical of the traditional slow wind. In fact, the elemental composition and ion temperatures are similar to those of the fast wind, and only the differential velocity is different. However, the results of the differential velocity can be explained by the larger density of this wind. In fact, a larger number of Coulomb collisions tends to erase the differences in speed between different species toward a uniform value. Larger density can also explain why at the slowest speeds, where density is largest, the ion temperature ratio departs from the fast wind values and decreases toward equal temperatures. In this case, however, it is also possible that plasma released from newly emerged loops, where the FIP effect has not had the time yet to change their Fe/O ratio, contributes to decrease the ion temperature ratio.

The results of the high (column 1) and intermediate (column 2) Fe/O ratio winds can be explained by a scenario where Alfvén waves are also active in the plasma released from closed loops. Given their Fe/O ratios, both these wind classes are likely to originate from closed coronal loops (with different ages) opened by magnetic reconnection. At the moment of release their differential velocity and ion temperature ratio are expected to be zero and unity, respectively, as this plasma is likely to have been at rest and near equilibrium before release. However, the temperature ratio values closer to the fast wind values strongly suggest that the same processes accelerating the wind from coronal holes are active in accelerating this plasma outward after release. Starting from equal temperatures, the plasma evolves toward temperature ratios closer to the fast wind values; however, its higher density leads to more Coulomb collisions than in the fast/boundary wind, partially erasing the effect of the waves on the temperature ratio and completely wiping out the effects on differential velocities.

Figure 3.3 provides a qualitative picture of the kinetic properties of the plasmas with different Fe/O values. To further investigate the relationship between the differential velocity, ion temperatures, and the Fe/O ratio, we investigated in detail the distributions of the differential velocity and of the ion temperature ratio.

Figure 3.4 (a)-(c) shows the distribution of the solar wind differential velocity for all wind with velocity less than 400 km s^{-1} divided into the same Fe/O classes as Figure 3.3. In all classes the distribution is a skewed distribution with a dominant peak at low differential velocity and a large tail. We used an upper velocity limit of 400 km s^{-1} rather than considering the whole range of speed of the slow wind in order to eliminate the range of velocities where the differential velocity and ion temperature ratio for all Fe/O classes resemble the fast wind (see Figure 3.3 (b) and (c)). In this way, we focus on the wind that shows the largest mix of values, while preserving a data set spanning the entire range of Fe/O ratio values. Figure 3.4(d) shows all the fast solar wind (speed above 500 km s^{-1}). Figure 3.4 shows that the distributions of all three Fe/O classes of the slow wind (panels (a)-(c)) are essentially the same, with the only difference being the relative size of the tail to the peak. However, the distribution of the fast wind in Figure 3.4(d) is broad, centered at ~37 km s^{-1}, and resembles the tail of the slow wind distributions. This begs the question: Is the high differential velocity tail in the slow wind due to a second population, similar to the fast wind? We have carried out a 2-Gaussian fit of the distributions in each of the three Fe/O slow wind classes, and compared the results with the single Gaussian fit in the fast wind. Results are listed in Table 1. Figure 3.4 shows each of the two Gaussians individually in orange and their total in red. The parameters of the first Gaussian peak at low differential velocity are the same in all Fe/O classes, indicating that there is a portion of the slow wind that has little or no differential velocity; this portion accounts for 35-60% of all slow wind depending on the Fe/O class. The parameters of the second Gaussian also are very similar across all Fe/O classes: it is significantly broader than the first Gaussian, it is centered at around 20-26 km s^{-1}, and it accounts for 40-65% of the slow wind depending on the Fe/O class. The differential velocity corresponding to the peak of this second Gaussian is lower than that of the fast wind, but still is much larger than the first Gaussian, and shows that even in wind with high Fe/O ratio values, clearly originating from coronal loops and characterized by a large plasma density, the differential velocity is not negligible. We obtain qualitatively the same results when using the O^{6+}-to-proton differential velocity instead of the alpha-to-proton differential velocity.

Table 3-1: Parameters of the two Gaussian distributions fitted on the differential velocity distribution shown in Figure 3.4, and for the single Gaussian distribution fitted on the differential velocity of the wind faster than 450 km s-1, arbitrarily separated in a few velocity classes.

	Low Differential Velocity Gaussian			High Differential Velocity Gaussian		
	Centroid	Standard Deviation	% Counts	Centroid	Standard Deviation	% Counts
V < 400 km s^{-1} Log (Fe/O) >-0.6	5.65	5.5	35.7	21.8	17.6	64.3
V < 400 km/s -0.8 < Log(Fe/O) < -0.6	6.02	7.99	58.9	26.3	17.9	41.1
V < 400 km/s Log(Fe/O) < -0.8	5.68	6.27	42.3	21.1	17.7	57.7
450 km s^{-1} < V < 500 km s^{-1}	NA	NA	NA	24.5	20.9	100
500 km s^{-1} < V < 550 km s^{-1}	NA	NA	NA	36.8	26.8	100
550 km s^{-1} < V < 600 km s^{-1}	NA	NA	NA	45.9	26.5	100
600 km s^{-1} < V < 675 km s^{-1}	NA	NA	NA	44.8	21.5	100

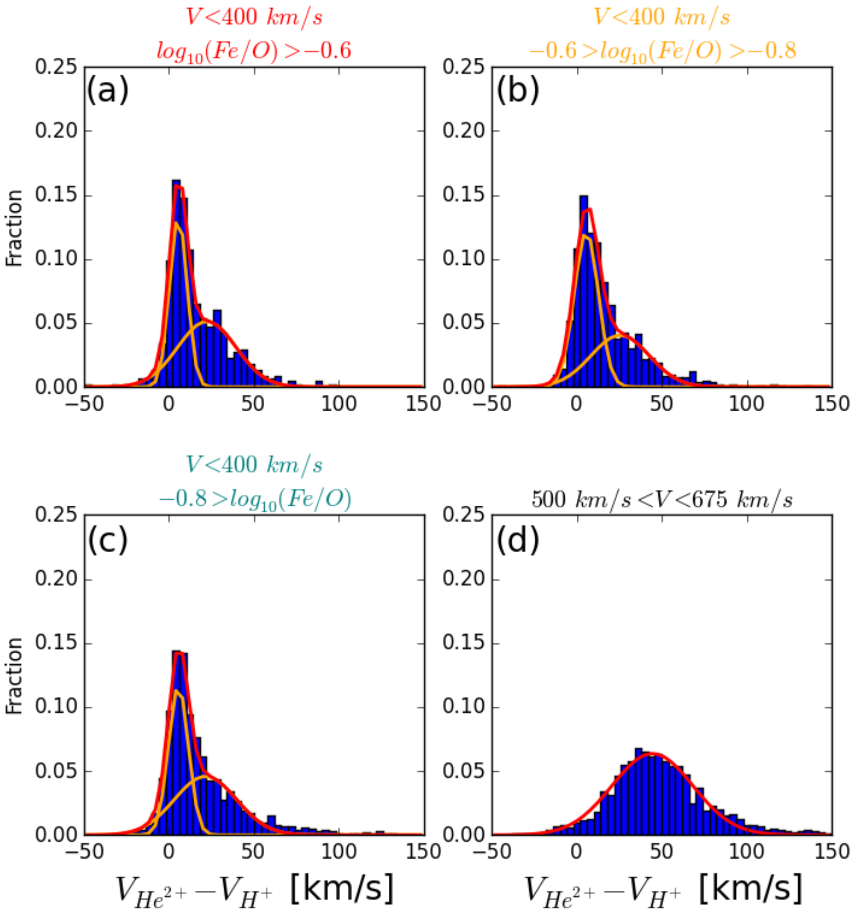

Figure 3.4: (a-c) Normalized distribution of the alpha-to-proton differential streaming of the slow velocity solar wind (V < 400 km s^{-1}) split by Fe/O ratio values. (d) Normalized distribution of the differential streaming of all the solar wind with velocity greater than 500 km s^{-1}. The solid red lines in all of the figures are the sum of the two Gaussians fitted to each wind component (shown in orange). This figure shows the two populations contained within the differential streaming in the slow solar wind.

It is also worth noting that if we carry out a single Gaussian fit to the fast wind, divided into velocity classes (which correspond to lower densities as the speed increases), we see that the centroid gradually increases from values similar to the second Gaussian in the slow wind to a maximum value of 45 km s^{-1} (see Table 1). This increase indicates three things: 1) Coulomb collisions are still active also in the fast wind; 2) they seem to stop being effective at speeds larger than ~550 km s^{-1}, after which the differential velocity distribution does not shift anymore; and 3) the effectiveness of Coulomb collisions on the tail of the distribution in the slow solar wind seems to plateau at the levels of the slowest fast wind.

This increase is most likely due to Coulomb collisions decreasing the differential velocities: Even if they are most effective in the slow wind, they are nonetheless unable to erase it completely.

The same type of analysis can be made for the O^{6+}-to-proton temperature ratio, and it is shown in Figure 3.5. Figures 3.5(a)-(c) show the temperature ratio for the slow solar wind ($V < 400$ km s^{-1}) divided into the same Fe/O classes as in the previous figures. We used the same upper limit of the velocity (400 km s^{-1}) as in Figure 3.4 in order to eliminate the range of velocities where the ion temperature ratios for all Fe/O classes resemble the fast wind one (see row C in Figure 3.3). Figure 3.5(d) shows the fast solar wind between 500 and 675 km s^{-1}. As in Figure 3.4, the slow wind distribution shows a marked tail at large ratio values and a peak at values closer to unity; however, the size of the tail is strongly dependent on the Fe/O value. The distributions were fitted with a double Gaussian, except for the fast wind where a single Gaussian was used. Figure 3.5 shows each of the two Gaussians individually in orange and their total in red. The results of the fit are reported in Table 2. The first peak at low ratio values shows two remarkable trends: First, its centroid and width are constant in all three Fe/O classes; second, its size (indicated by the percentage of the total number of counts) is larger at high Fe/O and much lower at intermediate and low values of Fe/O. On the other hand, the parameters of the second Gaussian indicate that 1) its centroid is lower than in the fast wind case, but it approaches the fast wind value as Fe/O decreases; 2) its width is larger than in the fast wind case; and 3) its size increases as Fe/O decreases. Also, the fast wind distribution centroid is even larger than the mass-proportional value.

Table 3-2: Parameters of the two Gaussian distributions fitted on the ion temperature ratios shown in Figure 3.5. On the left is data from the first Gaussian fit of the lower temperature population in the distribution. On the right is the data from the second Gaussian fit. Only one Gaussian was fitted on the wind faster than 500 km s-1.

	Low Temperature Gaussian Fit			High Temperature Gaussian Fit		
	Centroid	Standard Deviation	% Counts	Centroid	Standard Deviation	% Counts
V < 400 km s^{-1} Log(Fe/O) >-0.6	6.45	3.50	50.5	14.65	6.83	49.5
V < 400 km/s -0.8 < Log(Fe/O) < -0.6	5.89	2.36	24.7	14.61	6.78	75.3
V < 400 km/s Log(Fe/O) < -0.8	5.86	2.91	26.5	17.84	8.30	73.5
500 km s^{-1} < V < 675 km s^{-1}	NA	NA	NA	22.52	4.28	100

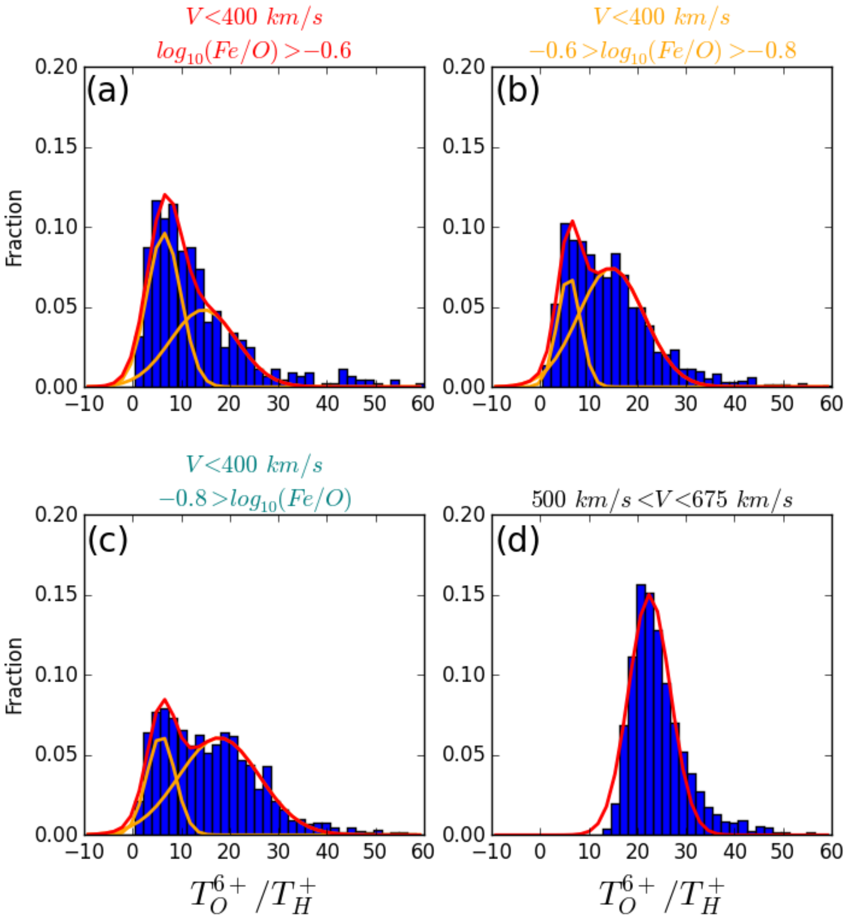

Figure 3.5: (a-c) O^{6+}-to-proton temperature ratio of the slow wind ($V < 400$ km s^{-1}) split up by Fe/O ratio ranges. (d) O^{6+}-to-proton temperature ratio of the fast wind (500 km $s^{-1} < V < 500$ km s^{-1}). The red lines in each figure are the sum of the fitted Gaussian (individually shown in orange) distributions whose parameters are listed in Table 1. All of the slow wind has two distinct peaks: peak one is at low temperature ratio closer to an equal temperature profile; another at a high temperature ratio close to a mass proportional temperature ratio of 16.

3.6. Discussion

The properties of the solar wind shown in Figures 3.1 and 3.2 indicate that the results obtained out of the ecliptic in chapter 2 are confirmed by ACE in the ecliptic plane, although there are a few differences. The speed of the fast solar wind is much larger in the Ulysses measurements, which report a speed around 760 km s^{-1}, relative to ACE, where the measurements seldom reach 700 km s^{-1}. The fact that the ACE spacecraft sees very little of the fastest wind is consistent with the fact that this spacecraft is more likely to observe wind coming from low-latitude coronal holes or from the boundaries of coronal holes (e.g. Oran et al. 2015), and also the fact that fast solar wind in the ecliptic is likely to interact with slow wind streams and thus lose momentum. At any rate, the conclusions drawn in chapter 2 for the wind faster than 500 km s^{-1} out of the ecliptic are confirmed also for the wind observed by ACE at the ecliptic: This wind is all fast wind, which owes its variable speed to the different locations within coronal holes where it is accelerated. Also, waves are the most likely drivers of its heating and acceleration.

Our analysis of the wind slower than 500 km s^{-1} has shown several important results. First, the kinetic properties of the slow wind at any Fe/O ratio present signatures of wave acceleration, namely, 1) the presence of non-negligible differential velocity, and 2) ion temperature ratios larger than unity and closer (or equal) to the fast wind values. It is particularly important to stress that these values are found even in the wind class with the largest Fe/O ratio, where the plasma is likely released by reconnection from previously closed coronal loops, and the proton density is largest. This indicates that wave acceleration is also present in the wind originating in closed coronal loops. Second, the presence of a wind with speed lower than 500 km s^{-1} having the same low Fe/O ratio and kinetic properties as the boundary (and hence fast) wind at larger speeds suggests that the boundary wind extends to velocities typical of the slow wind. In other words, wind accelerated by waves from the boundaries of coronal holes is present at basically all solar wind speeds.

We have carried out our analysis focusing on the Fe/O ratio, ion-proton differential velocities, and ion-to-proton temperature ratios. Each of these parameters has some uncertainty, as discussed in Section 2. We address these uncertainties here. First are the statistical uncertainties associated with the data, which are based upon Poisson counting statistics propagated through in the calculation of the reported plasma parameters. The uncertainties in the velocity measurements of the heavy ions are low. The average uncertainty in the measurement of the velocity of O^{6+} is around 0.2%, with 95% of the data falling below an error of 0.43%. This uncertainty corresponds to less than 1 km s^{-1} deviation in the measurements in the slow wind, and less than 1.5 km s^{-1} deviation in the fast wind. The uncertainties in the measurement of the velocity of He^{2+} are even less than those for O^{6+}, having an average error of around 0.03%, with 95% of the data falling below an error of 0.13%.

The statistical uncertainties in the measurement of the temperature of O^{6+} are larger than that of the velocity. These uncertainties are dependent on the measured counts, which have a strong dependence on velocity (i.e. a faster solar wind generally leads to more measured counts). The fast solar wind ($V > 500$ km s^{-1}) has an average measured uncertainty of around 2%, with 95% of the data having an uncertainty of less than 3.4%. The slow solar wind ($v < 500$ km s^{-1}) has an average measured uncertainty of around 8%, with 95% of the data having an uncertainty of less than 16.5%. The measured uncertainty for the proton temperature is less than that of O^{6+}, with 95% of the data having an uncertainty of less than 8% and 1.9% in the slow and fast solar wind, respectively. The statistical measurement error for the O^{6+}-to-proton temperature ratio (calculated by propagating the O^{6+} and proton temperature error) is an average of 9% and 2.3% in the slow and fast wind, respectively, with 95% of the data having an error of less than 17% ($V < 500$ km s^{-1}) and 4% ($V > 500$ km s^{-1}). This uncertainty corresponds to an uncertainty of less than 1.9 in the measured temperature ratio in the slow wind, and less than 0.6 in the fast wind. This difference in the uncertainty leads to a slightly larger spread in the measured temperatures of the slow solar wind, but not a significant enough spread to affect the conclusions drawn. Similarly, the statistical error in measurement of the density ratios of carbon and oxygen used in this chapter are around 16%, regardless of speed, very comparable to previous reports of density errors (von Steiger et al. 2000).

Another measurement error affecting the spread in the differential velocity is the averaging of the magnetic angle to the two-hour measurement cadence. Since particles in the solar wind are tied to the magnetic field, differential streaming occurs along these field lines. When these field lines are not radially outward from the Sun the instrument records only the radial projection of the differential streaming. The measurement is then corrected to calculate the true differential velocity along the field line given the magnetic field angle (following Berger & Wimmer-Schweingruber 2011). During the two-hour measurement time the magnetic field angle may change, and with it the correction in the differential velocity also changes. To characterize how much the magnetic field changes during our measurement time we calculated a standard deviation in the magnetic field angle. This standard deviation allows us to visualize how much the magnetic field changes during the measurement with a low standard deviation corresponding to a steady magnetic field and a high standard deviation corresponding to a more transient magnetic field. The data used in this study had an average standard deviation in the magnetic field angle of around 13 degrees. In the solar wind this 13 degree standard deviation corresponds to an error of around 7.4 km s^{-1} in the slow solar wind ($V < 400$ km s^{-1}) and 17.4 km s^{-1} in the fast solar wind ($V > 500$ km s^{-1}). Using a shorter accumulation time would mitigate the uncertainties due to the magnetic field angle correction but introduce an increase in the measured uncertainties due to a decrease in the counting statistics. The dominant contribution to the uncertainty in the differential streaming stems from the deviation in the magnetic field, and depends on the measured speeds and average magnetic field angle. Overall, the measurement uncertainties make the differential velocity a less reliable parameter, while the ion temperature ratio and the density ratios are quite accurate as their uncertainties are significantly below their variability

In this chapter we have assumed that the ion-proton temperature ratios in closed magnetic loops — supposedly the source region of the high and intermediate Fe/O wind — need to be unity. However, coronal models based on Alfvén wave heating predict that ion-proton temperature ratios larger than unity can also be found in quiescent, large-scale coronal loops, reaching heights of around 0.3–0.4 solar radii from the photosphere or more. In the highest portions of these loops the density is sufficiently low to inhibit thermal conduction from protons and ions, so that the temperatures of different species can be different (van der Holst et al. 2016, in preparation). Once reconnection opens these loops, the plasma released in the heliosphere can have ion-proton temperature ratios larger than unity and close to mass-proportional values even without any additional wave acceleration. However, the large height of these loops would also cause their plasma to be subject to elemental fractionation by gravitational settling, a process studied in situ in the solar wind by Weberg et al. (2012, 2015). Gravitational settling causes the abundances of the heavier elements to be depleted at the top of the loops compared to the abundances of lighter elements. This process would cause coronal loop plasma to have Fe/O values lower than coronal values even in very old loops that should be affected by the FIP effect: the Fe/O values of the wind plasma from these loops, measured by Weberg et al. (2012, 2015), is at the low end of the low Fe/O class of slow wind considered in the present work. Thus, this process might account for the low Fe/O plasma with high temperature ratio. However, this does not explain the small but significant amount of slow wind of any Fe/O class that has non-zero differential velocity: gravitational settling has no affect on this parameter. Furthermore, Weberg et al. (2012, 2015) reported that the gravitationally settled wind accounts for 6-8% of the total wind (at any speed), a far lower percentage than the fraction of the slow wind in the low Fe/O class in our analysis. Thus, gravitationally settled loops can be safely dismissed as a relevant source of uncertainty for the ion temperature ratio in our analysis.

Coulomb collisions are a much more important source of uncertainty for the present work. Tracy et al. (2015) showed that protons are by far the most important source of Coulomb collisions in the solar wind, and their effect on the wind plasma, among others, is to equalize the ion temperatures of different species, and erase the signatures of differential velocity. Thus, Coulomb collisions are expected to dilute and erase the signatures of wind wave acceleration. The effects of Coulomb collisions are expected to take place in all the Fe/O wind classes we have introduced, but they should be strongest in the highest Fe/O class, as the density is largest, and should introduce a velocity dependence in the differential velocity and ion temperatures since slower speed winds tend to have larger densities (row D in Figure 3.3). Such a velocity dependence is readily identified in the ion temperature ratio measurements (row C of Figure 3.3) in all Fe/O classes of the slow solar wind, showing that indeed Coulomb collisions are active in these plasmas. However, there are two things to notice in Figure 3.3: First, Coulomb collisions stop providing significant effects in the ion temperatures ratios at speeds larger than 400 km s^{-1}, as this parameter becomes constant at values even larger than the mass-proportional one; second, even if they are effectively erasing the signatures of differential velocities for a large portion of the wind at speeds lower than 400 km s^{-1}, there is still a sizable portion of wind with non-negligible differential velocity, as shown by Figure 3.4 and Table 1. Even if its centroid is shifted toward lower values of the differential velocities than the fast wind, the second Gaussian in Figure 3.4 and Table 1 clearly shows that differential velocity is present despite the effects of Coulomb collisions. The differential velocity steadily increases even in the fast wind as the wind speed increases (and the wind density decreases), reaching a plateau at speeds larger than 550 km s^{-1}. These results indicate that both wave acceleration and Coulomb collisions are simultaneously active in all Fe/O classes of solar wind as well as in the fast wind, with the latter diluting the effects of the former on the kinetic properties of different species. The efficacy of Coulomb collisions is best seen with the Coulomb collisional age (A_C), which is a parameter that estimates the number of collisional timescales elapsed during the wind's journey from the Sun to our instruments. A larger A_C means that the plasma has undergone more Coulomb collisions, while low values of A_C are associated with plasmas that experienced fewer Coulomb collisions and thus can be expected to better preserve any signatures of processes experienced in the inner corona. We calculated the Coulomb collisional age for the O^{6+} heavy ion according to Kasper et al. (2008) and Tracy et al. (2015):

$$A_C = \nu^{\epsilon}_{th,O6p}\left(\frac{R}{V_{SW}}\right) \tag{3.1}$$

where $\nu^{\epsilon}_{th,O6p}$ is the thermalization rate of O^{6+} with protons and R/V_{SW} is the estimated ballistic travel time to 1 AU. The thermalization rate of the plasma was computed following Hernandez and Marsch (1985). Figures 3.6 and 3.7 show the ion temperature ratio for the three different Fe/O classes ((a)-(c)) and for the fast wind (d) with low (Log $A_C < 0$, Figure 3.6) and high (log $A_C > 1$, Figure 3.7) collisional age. In the high A_C case, the temperature ratios are very close to unity, but in the low A_C case, where Coulomb collisions are less frequent, the distributions of the ion temperature ratios in all Fe/O classes of the slow wind are very similar to those of the fast wind. Unfortunately, the parameter space of low A_C and high Fe/O is also the least sampled with our measurements at 1 AU. Were the statistics available, the kinetic signatures preserved in this low A_C, high Fe/O population would be ideal to compare to those seen in the coronal hole wind, which commonly arrives at 1 AU with a relatively low A_C. However, we can clearly see a signature of wave acceleration even in the partially collisional slow wind samples observed at 1 AU. This implies that wave acceleration leaves the same imprint on all our observed slow solar wind, regardless of its Fe/O ratio, and hence regardless of its source region, be it the boundary of a coronal hole or a coronal loop.

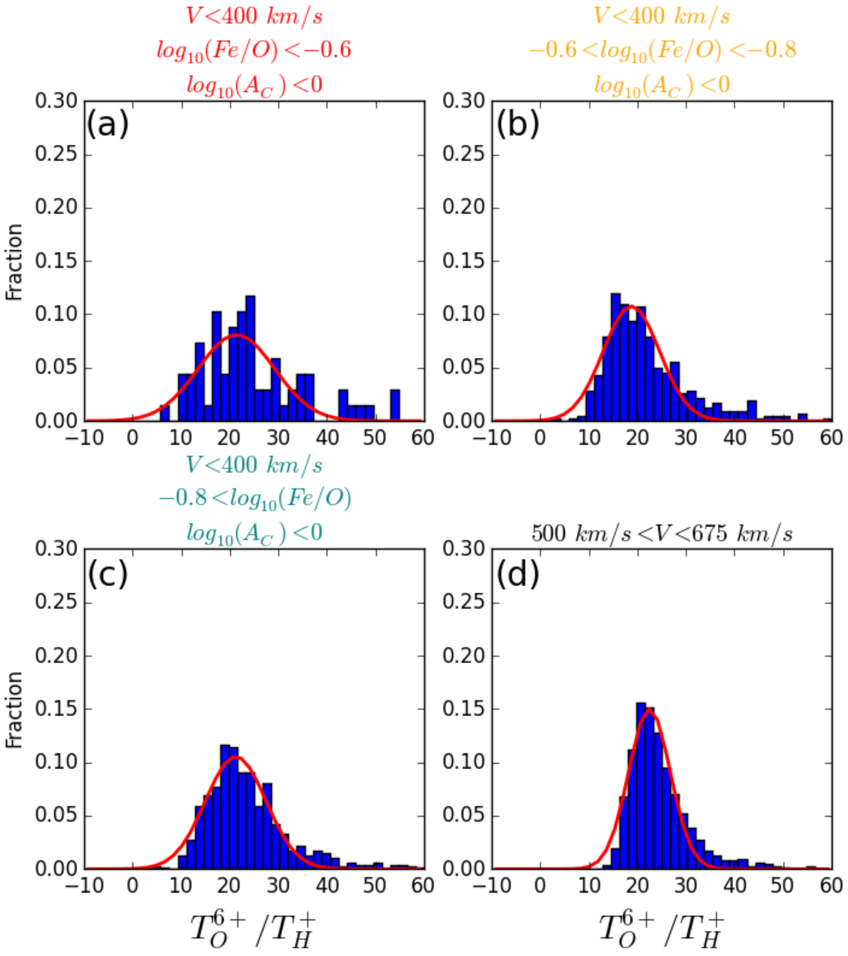

Figure 3.6: (a-c) O^{6+}-to-proton temperature ratio of the slow velocity solar wind ($V < 400$ km s^{-1}) with low collisional age ($\log(A_C) < 0$) split by Fe/O ratio. (d) fast wind. When only the low collisional age plasma is taken from the slow solar wind, the mass proportional temperature ratio population is isolated.

Another uncertainty in our methodology lies in the identification of the low Fe/O ratio class of slow solar wind as wind coming from the boundary of coronal holes rather than from coronal loops. The FIP effect, which is responsible for the increase of the Fe/O ratio in quiescent and active coronal loops, has been shown to be dependent on the age of the loops themselves, as the latter emerge from the subsurface regions of the Sun with photospheric composition and then their elemental abundances start to change with time. Thus, the wind plasma in the low Fe/O ratio class can be equally accelerated from the boundary of coronal holes or released from very young coronal loops by reconnection. Once released, both plasmas are subject to the same acceleration processes, and thus they cannot easily be distinguished from each other. This is the main weakness of the present work, and it casts a shadow of uncertainty on our identification of the presence of coronal hole-associated wind in the slow wind itself. However, since there is no compelling reason why the boundary wind could not be slower than 500 km s^{-1} (for example, Oran et al. (2015) predict the presence of boundary wind at 250 km s^{-1}) we think it likely that the low Fe/O ratio class of the solar wind is composed of both plasma released from very young loops *and* boundary wind.

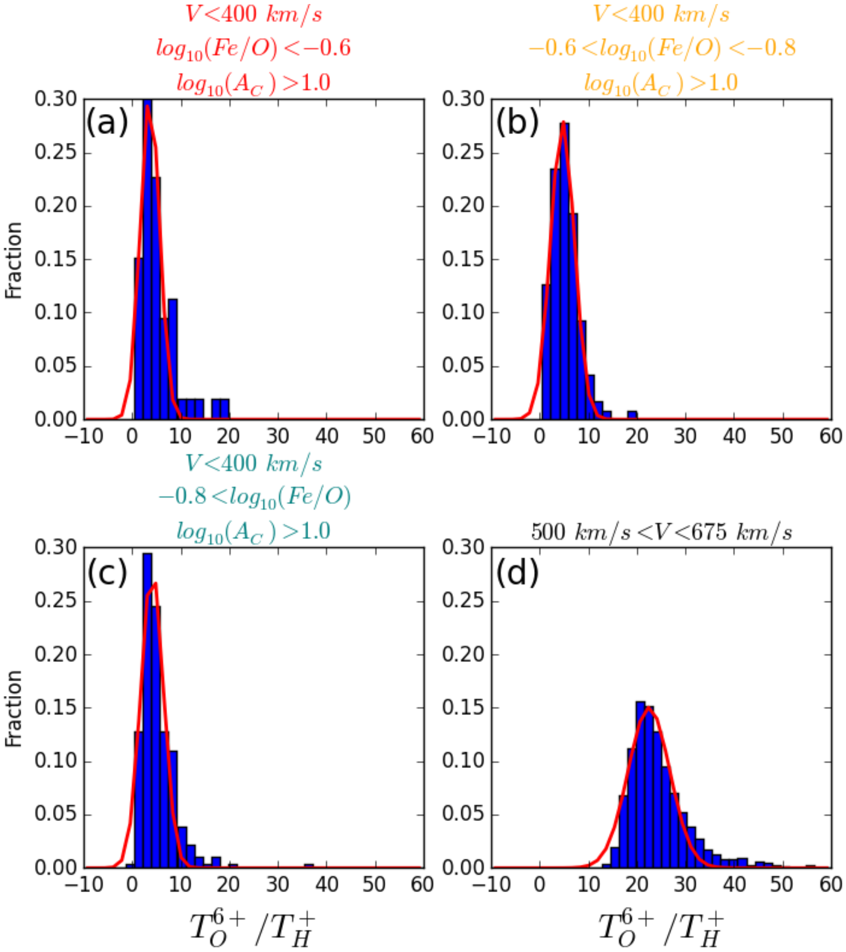

Figure 3.7: (a-c) O^{6+}-to-proton temperature ratio of the slow velocity solar wind (V < 400 km s^{-1}) with high collisional age (log(A$_C$) > 1.0) split by Fe/O ratio. (d) Same ratio for the fast wind. When only the high collisional age plasma is taken from the slow solar wind, the low temperature ratio population is isolated.

The final uncertainty that we address here is the changes in the measured thermodynamic properties of the plasma. Unlike the compositional properties, the thermodynamic properties of the solar wind can be changed in situ. One of the main mechanisms for changing these properties is stream interaction regions (SIR). SIRs are in-situ interfaces of the fast and slow solar wind (Burlaga 1974; Gosling et al. 1978). SIRs arise due to the difference in speed between the slow and fast solar winds and the rotation of the Sun. The buildup of material at the SIR interface results in a density enhancement that in turn results in more Coulomb collisions. A momentum transfer between the fast and slow solar wind also occurs at the interface. Over the two-year period of this study 20% of the data were found to occur within an SIR listed in Jian et al. (2006). When filtered out of the data, the results of this chapter are unchanged. Further analysis of SIRs and their effects on this study are warranted but outside the scope of this chapter.

3.7. The Unified Wind Scenario

Considering the results of our analysis, and the discussion of the uncertainties intrinsic to the quantities we have analyzed, we come to three main conclusions regarding the slow solar wind:

1. The high Fe/O ratio wind originates from loops where it can acquire a FIP bias before being released by reconnection.
2. The low Fe/O ratio wind either originates from young loops or from coronal holes, near their boundary with closed field regions.
3. In all cases the slow solar wind is heated and accelerated by waves, regardless of its origin.

These results are consistent with those obtained in chapter 2, where we showed that the solar wind observed by Ulysses faster than 500 km s^{-1} is accelerated from coronal holes. The differences in wind speed and charge state composition are explained by the location of the source region within coronal holes. The slower, more ionized wind originates from the boundaries of coronal holes, and faster, less ionized wind comes from coronal hole centers. Having shown in the present work that the Ulysses results about the fast wind are confirmed with ACE on the ecliptic, we combine them with our analysis of the wind slower than 500 km s^{-1} to propose a unified scenario regarding the solar wind, in which the solar wind is consistent with all of our data. We suggest that the solar wind has two different source regions (closed loops and coronal holes) but a single acceleration mechanism for all types of wind.

CHAPTER IV

HIS Modeling

4.1. Introduction

There still exist many outstanding questions about the origin and heating of the solar wind. In order to answer these questions more comprehensive measurements must be made of the solar wind. It has been observed that there exists an anisotropy in the temperature distribution of protons and heavy ions. Previous measurements of the heavy ions with ACE and Ulysses SWICS cannot measure these deviations from Maxwellian distributions due to the 1D nature of the measurements. To address this full 3D velocity distribution functions of heavy ions need to be made to enable us to study the temperature anisotropy that exists in the solar wind. Additionally, in situ data at different distances from the Sun can shed light on any processes that are occurring to the solar wind between the Sun and the Earth, such as Coulomb collisions and in situ heating. Finally, as shown by the Ulysses spacecraft, data taken at different latitudes can provide a wealth of information on differences in the origin of the solar wind. Solar Orbiter (SO) is a new mission that seeks to answer the following questions:

1) What are the origins of the solar wind streams and the heliospheric magnetic field?
2) What are the sources, acceleration mechanisms, and transport processes of solar energetic particles?
3) How do CMEs evolve in the inner solar system?

Heavy ions in the solar wind can reveal valuable insight into the outstanding questions above. The Heavy Ion Sensor (HIS) on the SO will answer some of these questions by providing full 3D velocity distribution functions at varying radii and inclinations. In this chapter we support the HIS instrument development by characterizing the instrument's performance and calculating the geometric factor and time of flight efficiencies through the use of ion optical simulations. Having accurate knowledge of efficiencies and geometric factor of the instrument are critical in the accurate determination of physical quantities in the solar wind. The work done in this chapter provides the ground work for the calibration of the instrument by offering a reference for calculations of the efficiencies and geometric factor to compare against laboratory measurements.

4.1.1. Solar Orbiter introduction

Solar Orbiter (SO) is a European Space Agency mission set to launch in October of 2018. The spacecraft is dedicated to studying heliospheric physics with an array of Sun observing instruments. The main objectives of the mission is to make significant breakthroughs in our understanding of the inner heliosphere and the Sun using in situ measurements and remote sensing close to the Sun. In order to accomplish this task the SO spacecraft is planned to be inserted into a unique, highly elliptic orbit with a progressive inclination. Figure 4.1 shows the latitude and orbital distance this spacecraft over the course of the mission.

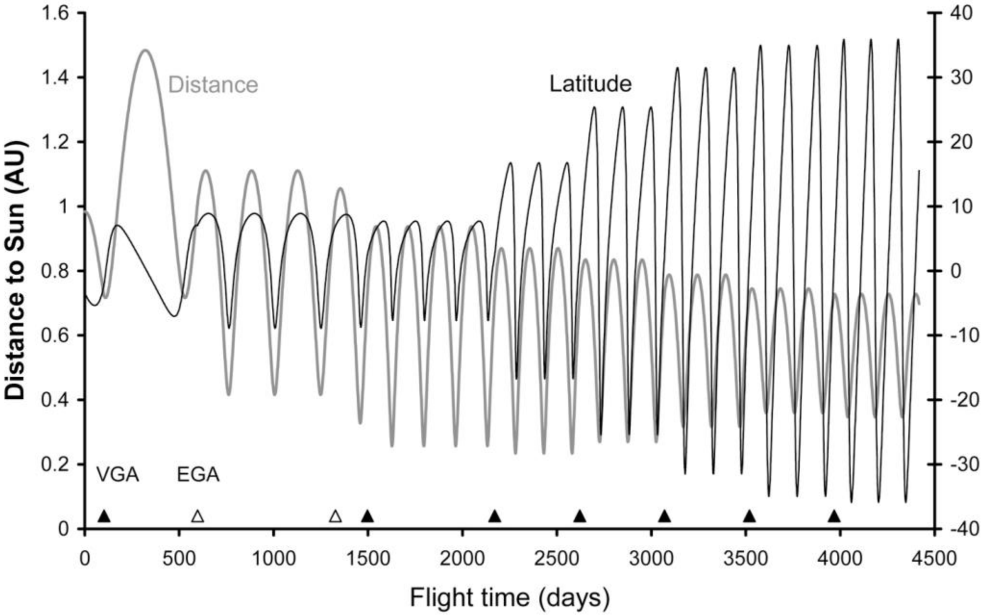

Figure 4.1: Latitude and distance of the Solar Orbiter spacecraft over the course of its mission

The Solar Orbiter spacecraft will be positioned at a range of latitudes over its lifetime. This will allow extensive measurement of solar wind streaming from different regions on the Sun and provide a connections to previously taken measurements with Ulysses and ACE. The instrument on the Solar Orbiter spacecraft that will be focused on in this chapter is the Heavy Ion Sensor (HIS) instrument.

4.1.2. Science Motivation for HIS

The Solar Orbiter spacecraft has several prioritized science objectives that HIS can help address: What is the origins of the solar wind streams and of the heliospheric magnetic field? How do coronal mass ejections evolve in the inner solar system? By providing 3D velocity distributions of heavy ions at different radii and inclination, the HIS instrument will be able to see the evolution of the solar wind as it streams farther into the heliosphere. In particular HIS will be able to measure the temperature anisotropy that exists in the heavy ions and observe how the temperature changes as a function of radius and measure the heating signatures left in the wind from heating in the corona. This change in the temperature with radius can provide insight into the local mechanisms that affect the solar wind in the heliosphere, and provide the ground work for modeling the solar wind at its source. Measurements at different solar radii can also enable the spacecraft to disentangle in situ heating from the initial coronal heating, allowing us to further understand how much the solar wind is heating in the corona.

The unique orbit that Solar Orbiter will be placed in allows for sections of the orbit to be co-rotating with the surface of the Sun. During these time periods the surface of the Sun will be essentially stationary under the spacecraft and allow the spacecraft to observe the same flux tube over a long period of time. Measurements taken during this time period can be compared to simultaneous remote-sensing observations on the spacecraft, allowing for the solar wind to be traced back to its solar source region. These measurements will allow us to see the time variations in a single flux tube without the usual spatial variations associated with the spacecraft moving from flux tube to flux tube. These measurement will provide the data to help answer science questions in the heliosphere, including: How does fast solar wind relate to the three-dimensional structure of coronal holes? Does the slow solar wind originate from the edge of coronal holes or from loops?

4.1.3. Instrument layout

The HIS instrument is a top-hat time-of-flight ion mass spectrometer capable of measuring energy per charge (E/q), energy (E), time-of-flight (TOF), azimuth angle into the instrument (φ), and elevation angle into the instrument (θ). The instrument consists of 3 sections: the electrostatic analyzer with ion steering (EA-IS, described in section 4.1.3.1), the time-of-flight section (described in section 4.1.3.2), and the electronics section (as can be seen in Figure 4.2). The instrument is cylindrically symmetric over a 96° range that corresponds to the azimuthal field of view, as shown in Figure 4.3.

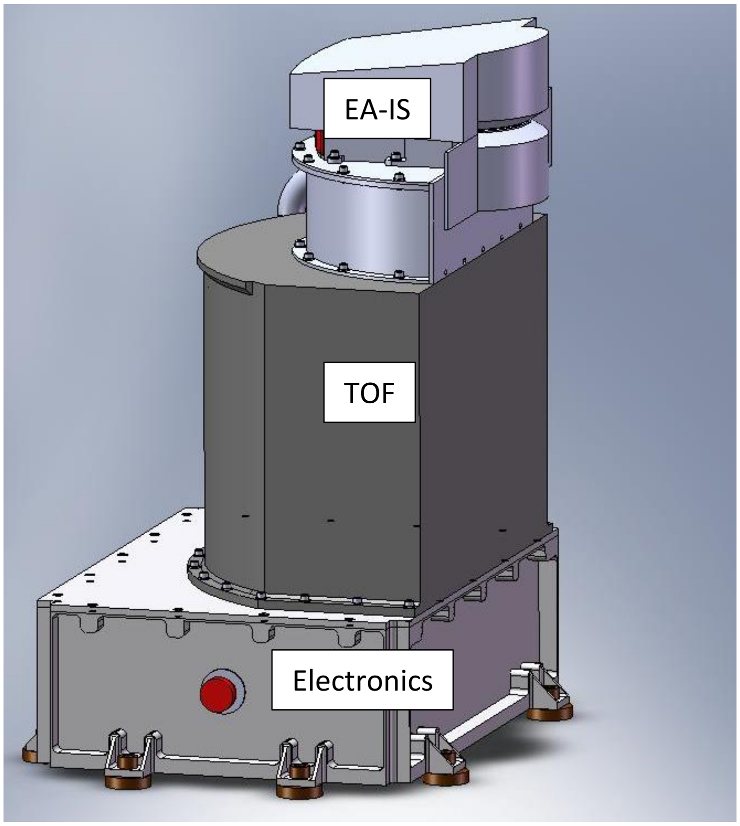

Figure 4.2: CAD drawing of the HIS instrument showing the 3 main sections of the instrument: the electrostatic analyzer with ion steering (EA-IS), the time of flight sections (TOF), and the Electronics sections

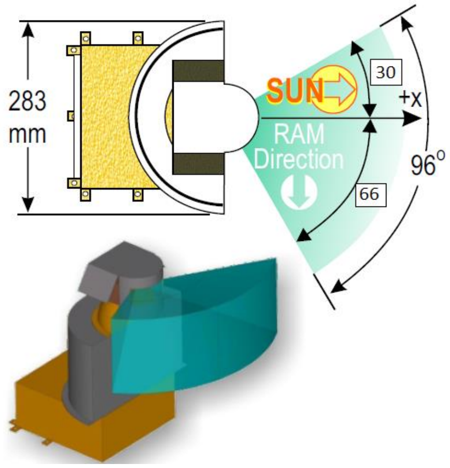

Figure 4.3: Field of view of the HIS instrument. There is a total azimuthal field of view of 96°, with 66° in the ram direction.

There are a total of 3 measurement surfaces in the HIS instrument. The instrument measures the energy (E) of ions with a solid state detectors (SSD) located at the back end of the TOF section. The time-of-flight of ions are measured with microchannel plates (MCPs) located in the TOF section. The E/q and elevation angle (θ) of the ions are passively collected based on the voltage settings of the EA-IS (see section 4.1.3.1). The azimuthal position (φ) is measured with the start MCP. Both the EA-IS section and TOF sections have different voltages applied to them to guide the particles through the instrument. The EA-IS has a total of 4 charged plates with adjustable voltages that are used to steer into the aperture. Ions leaving the EA-IS section of the instrument are accelerated before entering the TOF section by a large voltage difference between the two sections of the instrument. This voltage difference between the EA-IS and TOF section is used as to accelerate ions leaving the EA-IS to give the ions sufficient energy to trigger the energy detector in the TOF section of the instrument (20-30 keV; Wuest et al. 2007). When an ion enters the TOF section it passes through a carbon foil which is used to both neutralize the ion and scatter electrons that are guides to an MCP used for the start signal. Several voltages are applied to different surfaces in the TOF section to guide electrons generated at the carbon foil and SSD to the start and stop MCPs, respectively. The case housing the MCPs are held at slightly lower voltage than MCP themselves to suppress any secondary electrons generated, guiding them back towards the MCP. Figure 4.4 shows the entrance a cut of the HIS instrument with the flight path of an ion through the EA-IS and TOF sections.

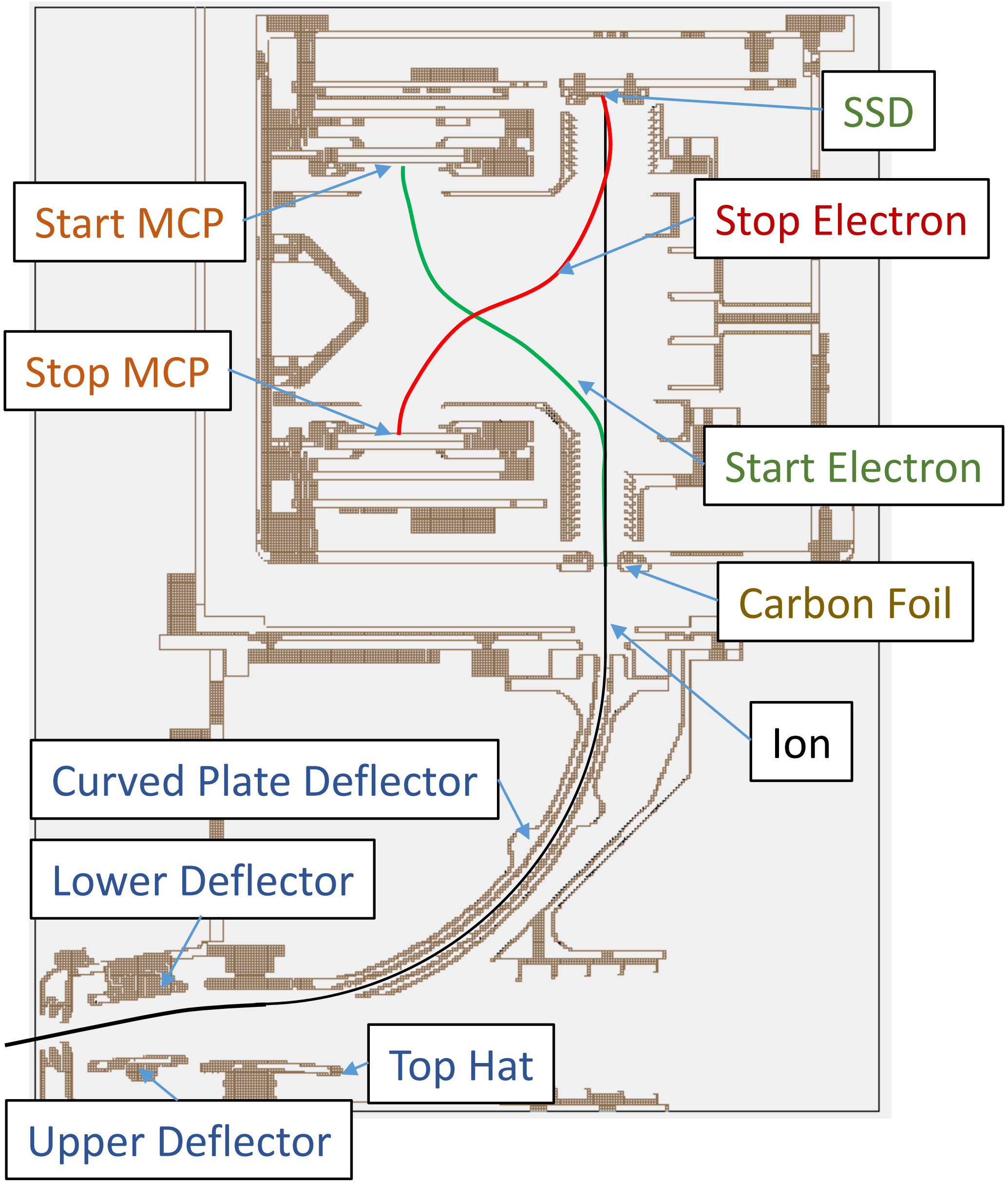

Figure 4.4: Cut of HIS instrument around the 0° azimuthal line. The four charge surfaces that can be set in the EA-IS (curved plate deflector, lower deflector, upper deflector, and top hat) are labeled in blue. The start MCP, stop MCP, SSD, and Carbon Foil (CF) in the TOF section are also labeled. A flight path of an ion is sketched in the figure (black) with the corresponding electrons that are scattered by the electrons (start electron – green, stop electron - red)

4.1.3.1. EA-IS Section

The electrostatic analyzer section of the HIS instrument uses 4 plates with adjustable voltages to select and guide ions through to the TOF section. The field of view of the instrument spans 96° in azimuth (from -30° to 66°). The front of the EA-IS section has a heatshield to protect it from the extreme heats from the Sun. Once ions pass through the EA-IS, the E/q and elevation angle (θ) of the ions are known to within an energy passband and elevation passband, which will be discussed later in this chapter in section 4.4.3. Figure 4.5 shows a cut of the EA-IS with voltages applied to select for an E/q of 1 keV/e and 0° elevation angle.

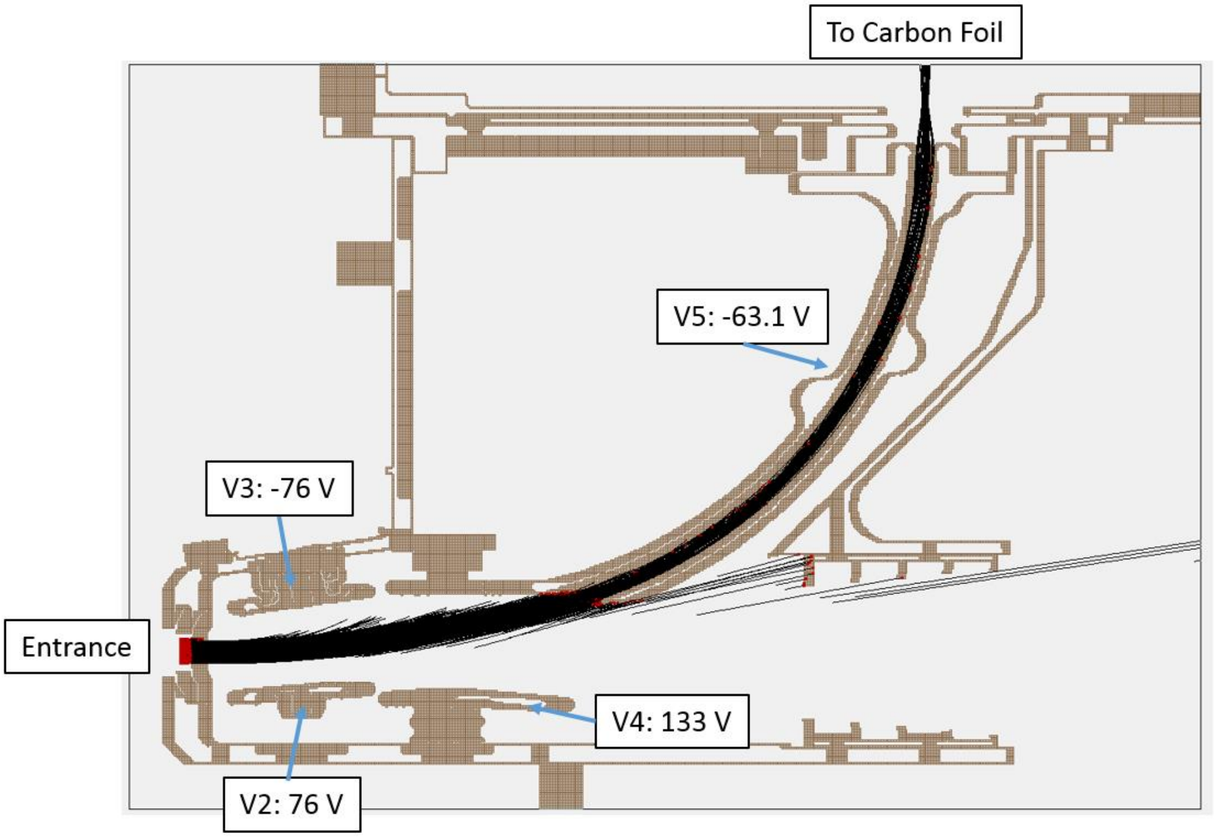

Figure 4.5: EA-IS Cut with labeled voltages and ion flight path (black). The electric fields produced by setting the voltages at the various surfaces guide ions with specific E/q and elevation angles through the EA-IS.

In Figure 4.5 we can see the flight path of the simulated ions (black) through the EA-IS. The applied voltages in this section of the instrument create an electric field that deflects the ions that enter the instrument (seen as black lines). Ions traveling too fast or possessing too low of a charge will not be deflected enough to make it through the curved plates, resulting in them hitting the wall or exiting out of the back of the instrument. Ions traveling too slow or possessing too high of a charge will be deflected too much and meet a similar fate. The instrument is specifically designed to allow light to pass through it, or be deflected in such a way as to not let light through the EA-IS and into the TOF section. This is important because stray light can cause noise on the detectors in the TOF section. Once the particle has made it through the EA-IS section of the instrument it is accelerated into the TOF section.

The EA-IS voltages are set for a specific E/q and elevation angle. Once the collection time for a particular step is done the EA-IS adjusts its voltages to the next step (stepping over a range of E/q and elevation angle values). Once all of the voltage setting have to been collected, a full scan is compiled and the distribution of the solar wind can be calculated.

4.1.3.2. TOF Section

Emerging from the EA-IS section of the instrument, the ion is accelerated by an electric field across a small gap present due to the TOF section being held at -25000 V and the EA-IS section being held near 0 V. This acceleration is known as a post acceleration because it is a known acceleration imparted on the particles after the E/q of ions are known. This post acceleration is in place to give the ion enough energy to eventually registered an energy measurement in the SSD, which requires a minimum energy of 20-30 keV (Wuest et al. 2007). Figure 4.6 shows a diagram of the TOF section with particles trajectories. The first thing that ion encounters in the TOF section is the carbon foil, which is mounted on the case of the TOF section. The carbon foil is a thin sheet of carbon that allows the ion to pass through while mostly neutralizing the ion and scattering off electrons (further details on carbons foils can be found in McComas et al. 2004). These forward scattered electrons (green) are then guided through the TOF section to the start MCP where they record a start signal.

Once the ion passes through the carbon foil, the newly neutralize or slightly charged ion flies to the SSD where it triggers the energy detector and creates secondary electrons. These electrons (red) that are scattered off of the SSD by interactions with the ions penetrating the SSD are then guided to the stop MCP via charge surfaces, where they are recorded as a stop signal. The distance from the carbon foil to the SSD is known. With this distance and the start and stop times collected from the MCPs, the velocity of the particle can be calculated by dividing the distance by time. The actual time of flight time is calculated from eq. 4.1.

$$TOF = T_{Stop} - T_{Start} + TOF_{Start\_E} - TOF_{Stop\_E} \tag{4.1}$$

Where T_{Stop} is the Time of the stop signal, T_{Start} is the time of the start signal, TOF_{Start_E} is the known flight time of the start electron, and TOF_{Stop_E} is the known flight time of the stop electron. The time it takes for the electrons to travel from the carbon foil to the start MCP (TOF_{Start_E}) is only several nanoseconds and is similar to the time it takes for the electrons generated at the SSD to travel to the stop MCP (TOF_{Stop_E}) (Gloeckler et al. 1992). Nevertheless, these times contribute to the total measured flight time of the ion and must be subtracted out to accurately recover the TOF of the ions.

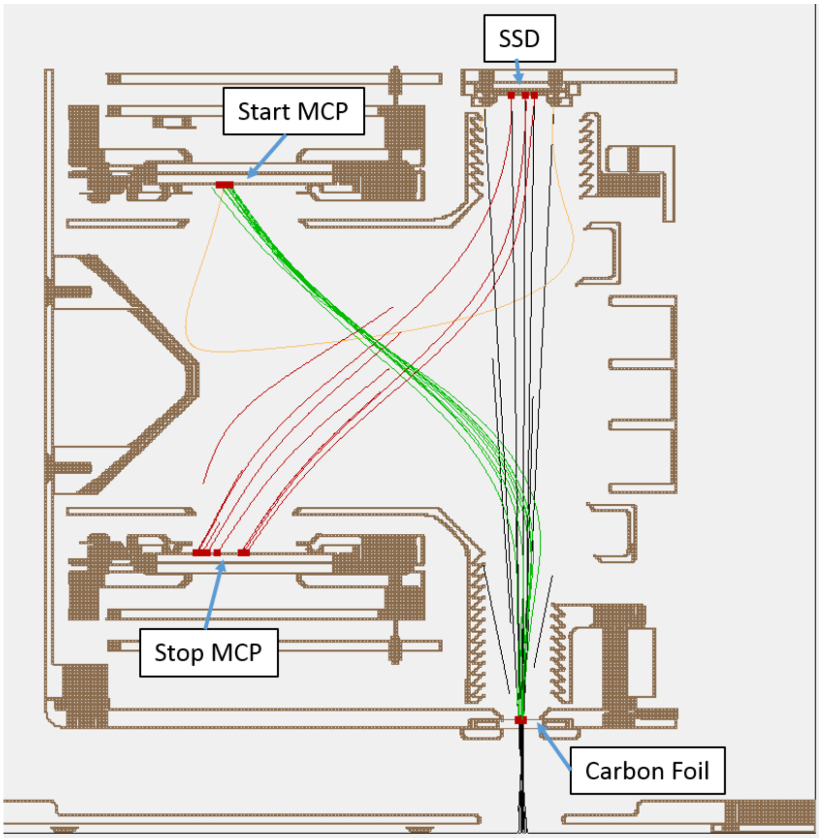

Figure 4.6: TOF section of the HIS instrument with particle trajectories. The ions are shown in black, the start electrons scattered off of the carbon foil are shown in green, the stop electrons scattered off of the SSD are shown in red.

When an ion passes through the carbon foil four things occur: (1) The ion is neutralized or left signally charged (Allegrini et al. 2014); (2) The ion scatters electrons off of the carbon foil used for the start signal; (3) The ion is deflected; (4) The ion loses energy.

4.2. HIS SIMION model

To study and characterize the HIS instrument, a SIMION model was created and test particles were flown through the instrument in Monte Carlo simulations. SIMION is an ion optical program that numerically solves the Laplace equation in 3 dimensions given an instrument geometry and surface voltages. The Full 3D CAD model of the HIS instrument was imported into the SIMION program for the purposes of characterizing the instruments geometric factor, efficiencies, and the general instrument performance. Section 4.3 of this dissertation focuses on using the SIMION model to identify performance issues with the HIS instrument. Section 4.4 describes and calculates the geometric factor of the instrument with the help of Monte Carlo simulations using the SIMION model. Finally, the efficiencies of the TOF section of the instrument are calculated using the SIMION model in section 4.5. In the SIMION model ions are generated at the entrance of the instrument with a given energy, mass, charge, and initial trajectory (azimuthal angle and elevation angle). In the simulations the particles are generated evenly across the entire entrance aperture and evenly over a given energy and elevation angle range. When an ion reaches the carbon foil in the model it randomly deflects the ion in a forward direction consistent with previous lab measurements of carbon foils. Energy is also taken from the ion at this point to fully simulate the effects of the carbon foil. Finally an electron is generated at the carbon foil and given a random forward direction scattering similar to the deflection of the ion. When the Ion reaches the SSD another electron in generated in the model to simulate the scattered electron off of the SSD. Also simulated are electrons generated by the ion hitting any surface in the TOF section. This secondary electron simulation allows us to see the noise caused by electrons generated by other sources in the TOF other than the SSD. In the end, snapshot measurements of the position (x,y,z), velocity (V_x, V_y, V_z), and energy are collected at 7 locations:

1. Initial position
2. Exit of the EA-IS
3. Pre-carbon foil
4. Post-carbon foil
5. Ion termination location (either SSD, or wall)
6. Start electron termination location

7. Stop electron termination location

4.2.1. Resolution difference in the curved plate and its effect on the analyzer constant

SIMION is a Laplace solver with finite resolution. Fine surfaces that have structures smaller than the resolution size of the SIMION model are not accurately refined. This problem occurs in the EA-IS curved plate surfaces, where there is a fine ridged structure and a small separation (2.3 mm) between the two plates (See Figures 4.7 and 4.8).

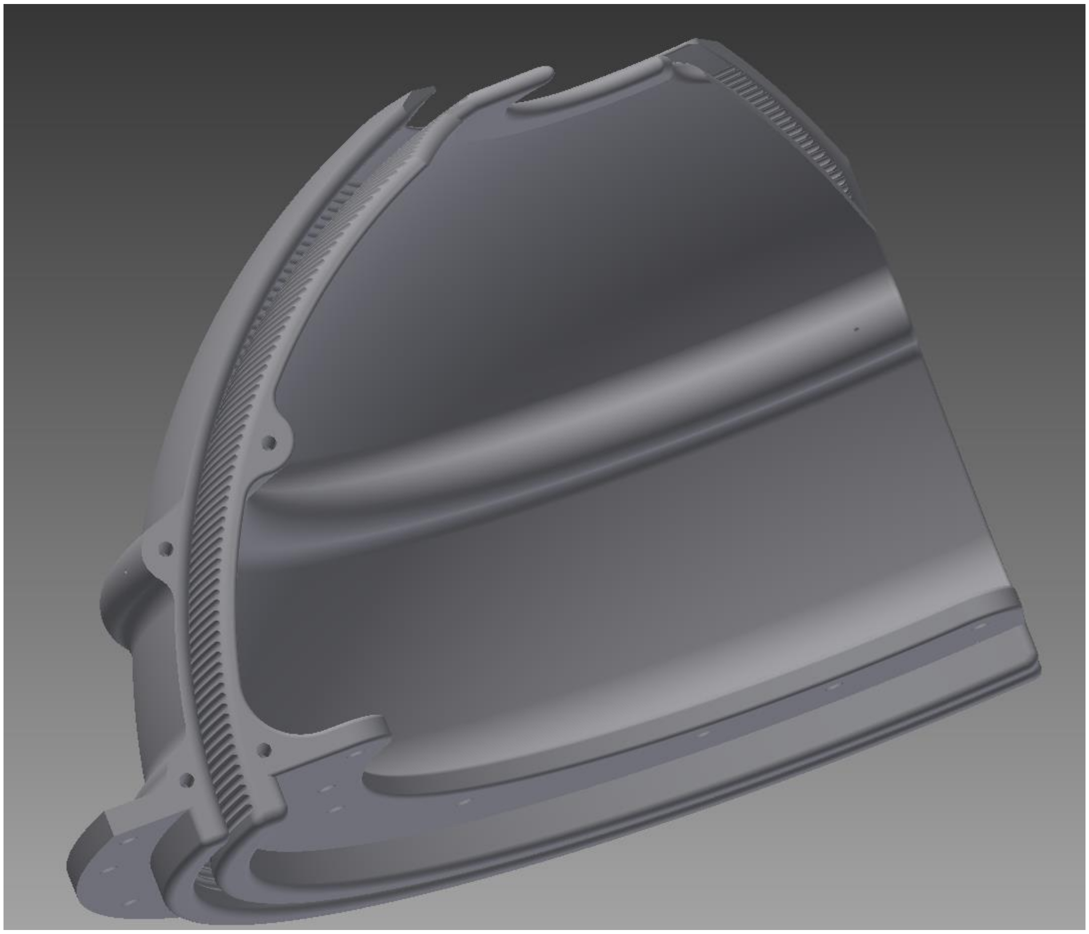

Figure 4.7: Capture of the curved plate geometry and separation distance

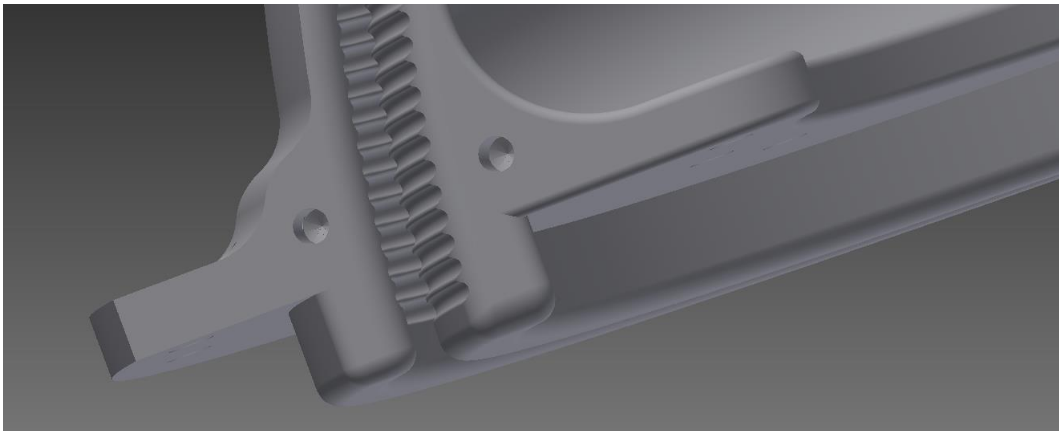

Figure 4.8: Zoomed capture of separation distance of curved plate and the jagged interior surface

Limitations in computational memory required the model to run at a resolution of 0.25 mm/gu (graphical unit). This resolution combined with the jagged edges of the curved plates cause the model solution in the curved plates to be compressed. This results in a smaller distance between the plates and a larger analyzer constant than what the actual instrument possesses. A previous study of the instrument was conducted to characterize the analyzer constant due to the set model resolution. The analyzer constant is a standard characterize parameter in electrostatic analyzers. This analyzer constant is a ratio between the energy of the particle (eV) and the voltage difference (V) between the curved plates over the gap. Figure 4.9 below shows the results of this study for several different resolutions.

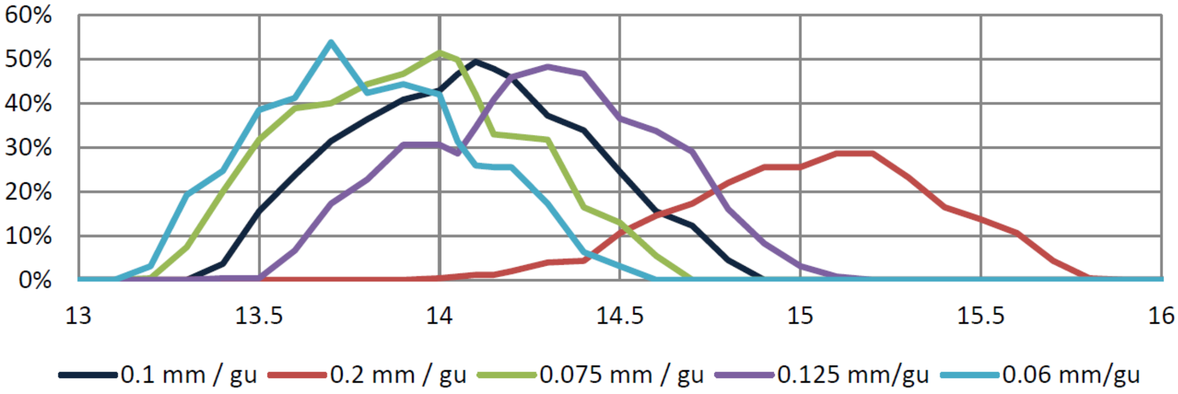

Figure 4.9: From 130-0367 Ion Optics Simulations Summary by Matt Panning. Simulated count rate through the curved plate of the EA-IS for various model resolutions.

From these results the following equation was developed to relate the resolution to the analyzer constant.

$$k = 34.192\,x^2 - 0.4108\,x + 13.814 \tag{4.2}$$

Where x is the model resolution (mm/gu) and k is the analyzer constant. For the purposes of this chapter the highest resolution possible was chosen (x = 0.25), giving the model an effective analyzer constant of 15.85 eV/V. This is due to an apparent narrowing of the space between the two curved plates due to the resolution. This is larger than the actual analyzer constant of 13.5 eV/V.

4.3. Instrument Performance

To maximize science return from HIS, it is vital to model and analyze the performance of the instrument design. Although an ideal instrument would not have any performance issues, the real instrument does and these need to be characterized and accounted for. Identifying and characterizing all of the known issues in the instrument will allow us to understand the output of the instrument better and create more accurate corrections to the data sets. Another reason to identify and address issues with the HIS instrument is to build up a knowledge base for future designs of instruments. This section of the dissertation will address several performance issues that the HIS instrument possesses.

4.3.1. MCP azimuthal angle dependence

One of the independent measurements that the HIS instrument needs to acquire in order to produce 3D velocity distribution functions is the azimuth position of the measured ion. This is accomplished with the start MCP which measures the position of the start electron that was created at the carbon foil, using a delay line anode. Upon investigation it was discovered, both in the laboratory and in simulations, that there was an angular dependence to the position sensing of the start MCP. Figure 4.10 shows the measured azimuthal position vs. the incoming position of the measured ions. Both the Laboratory measurements (red) and simulations (blue) show a linear response on the SSD to the input position, but a strong measurement dependence on the start MCP. In the SSD the measurement range covers the expected range of the instrument from -30° to 66°.

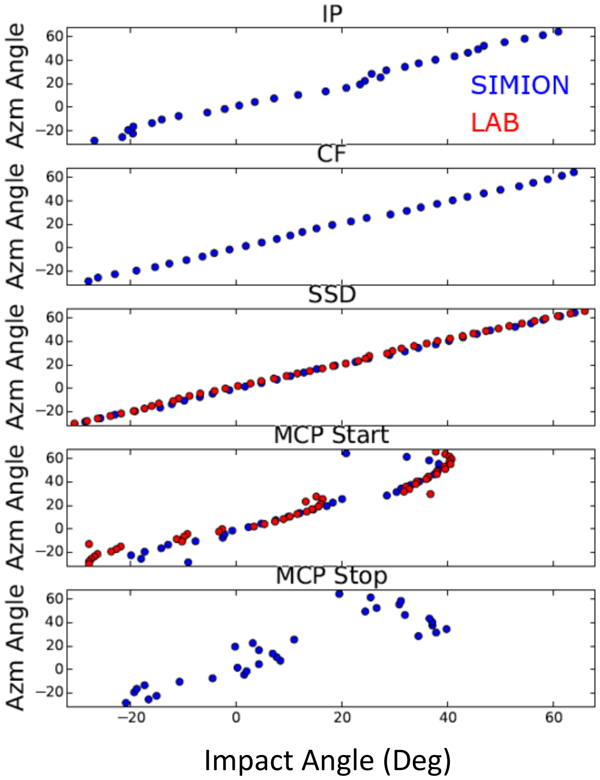

Figure 4.10: Measured azimuthal position vs. ions initial azimuthal position for the initial position (panel 1), carbon foil (panel 2), SSD (panel 3), Start MCP (panel 4), and Stop MCP (panel 5).

In Figure 4.10 we can see that at higher azimuthal angle measurements the reported position from the MCP (panel 4) is deflected back towards the center of the detector. This deflection of electrons before the MCP results in a loss of measurable azimuth angle above 30°. Although the instrument does take measurements up to 40°, the last 10° of that measurement space is not unique, therefore making it impossible to identify at which angle the particles originated.

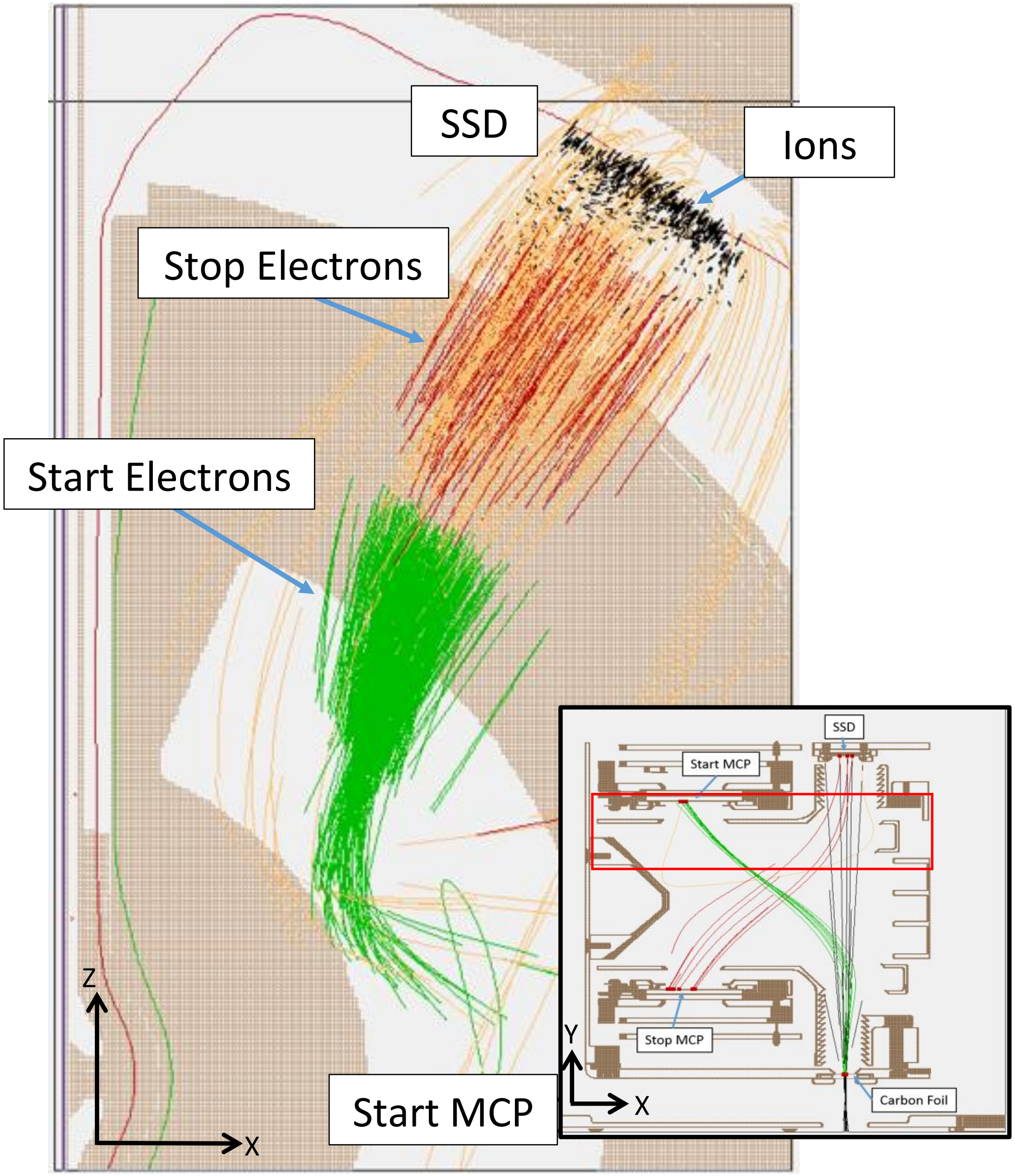

Figure 4.11: Horizontal cut over 20 mm of the TOF section of the HIS instrument. The position of the cut can be seen in the subfigure in the lower right, highlighted by the red box. The flight path of the start electrons (green), stop electrons (red), ions (black), and secondary electrons (yellow) can be seen in this figure. The ions (black) are flying from the carbon foil (into the page) to the SSD (out of the page), where they create the stop electrons (red). The start electrons are created at the carbon foil (into the page)

The cause of this azimuthal measurement error was investigated with the SIMION model to see if a solution could be developed. The first step was identifying where the electrons were being deflected and why they weren't hitting the start MCP in the proper location. To accomplish this task a test case was simulated where ions at azimuthal angles between 50° and 66° were generated at the entrance of the instrument. It was discovered through these simulations that the deflection was occurring near the end of the start electrons flight path. Figure 4.11 shows a cut of the instrument with the flight path of the start electrons (green).

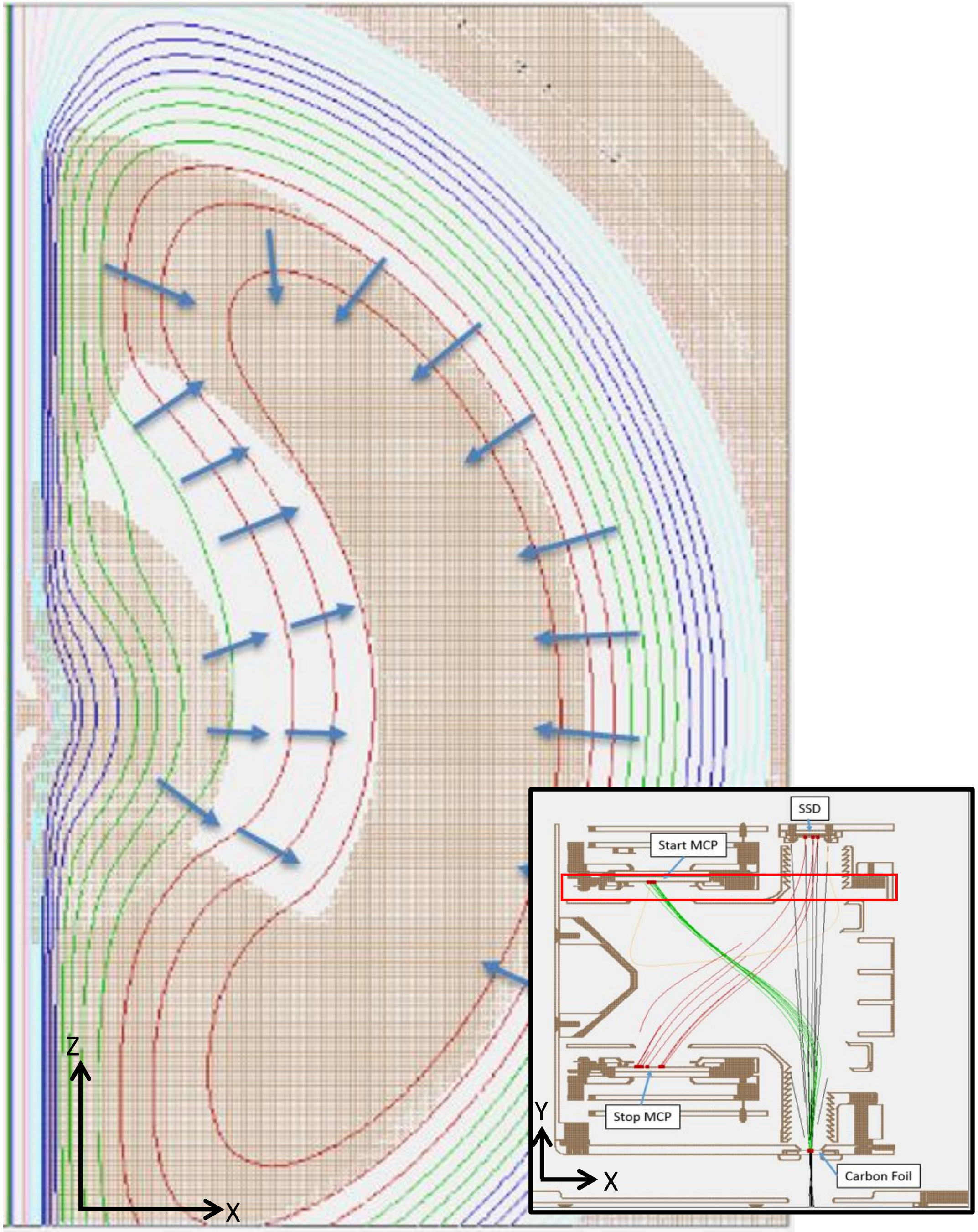

Figure 4.12: Horizontal cut over 5 mm of the TOF section of the HIS instrument. The position of the cut can be seen in the subfigure in the lower right, highlighted by the red box. Equal potential lines for the field near the start MCP. The blue arrows are annotations of the direction of the force experience by an electron in this field.

In figure 4.11 we can also see the ions (black), stop electrons (red), and secondary electrons (yellow) in the second half of the TOF section. The outline of the start MCP (large white area at the bottom) is shown, along with where the start electrons hit this MCP. Here we can see that the start electrons that should be hitting the top part of the start MCP are being deflected towards the middle of the detector.

Figure 4.12 shows the equal potential contour lines for the fields around the start MCP, annotated with arrows showing the resulting force on the electrons in that field. The electric field near the top of the MCP, where the particles with azimuth angles over 40° are measured, exerts a force on the electrons which moves them towards the center of the detector. This force is caused by the detector being placed too close to the wall of the TOF section which is held at -25000 V (while the detector itself is held at -24000 V). The same force cannot be seen on the other side of the detector because that side of the MCP only extends to -30° and is positioned far enough from the wall.

It is hard to conceptualize a solution to this problem without redesigning the TOF section. Swinging out the wall so that it is parallel to the top of the MCP would solve this problem, but would result in the TOF section being larger. Pulling the MCP farther from the wall could result in the electrons not being deflected enough to make it into the start MCP and would require the deflector in the middle of the TOF section to protrude farther into the instrument. These solutions are possible to employ in future designs of the TOF section, but are not practical for the HIS instrument that is already in fabrication.

The only possible solution that is present is acquiring the position sensing from the SSD rather than the start MCP. The SSD signal is less robust than the MCP because the minimum energy threshold for a signal to be generated is higher. The SSD also is less efficient at measuring ions that make it into the TOF section than the start MCP. However, when constructing the 3D velocity distribution functions (VDF) only particles that have triple coincidence (start signal, stop signal, and energy signal) will be considered. This means that an SSD signal is required for these VDF to be created, eliminating one of the reasons not to use the SSD for position sensing.

4.3.2. MCP Start Impact area

Over the course of a mission MCP detectors ability to detect electrons decline. To maximize the lifetime of the instrument, the flux of the particles hitting the detector should be evenly distributed across the MCP, to prevent hot spots and subsequently uneven wear and failure. Figure 4.13 shows the impact location on the start and stop MCPs with a simulation of 400,000 particles uniformly generated over all azimuthal angles. This distribution shows that the MCPs are preferentially being impacted on the far side of the detector. In figure 4.13 the polar position (R, θ) of the particles are being reported, since the MCP detectors are curved.

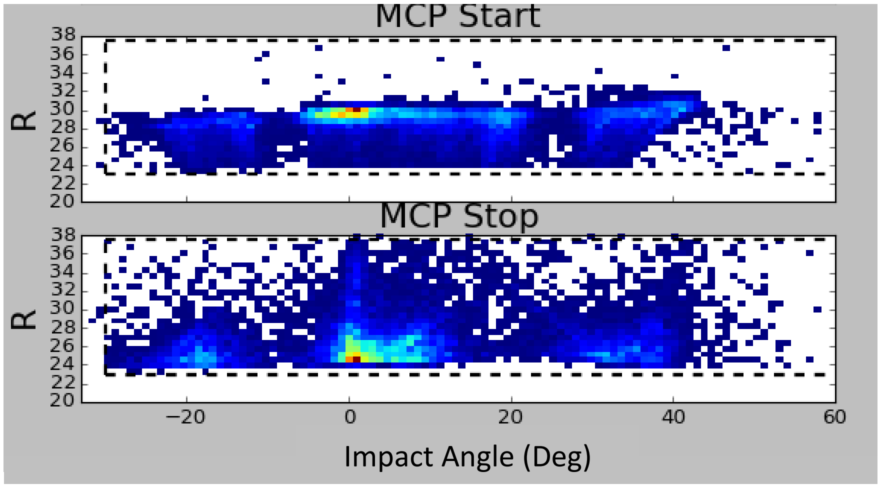

Figure 4.13: Start and Stop MCP impact area. The outline of the detector impact area are outlined with the black dotted line. In this figure the polar positons of the detectors are being reported due to the curved design of the detectors.

This simulation shows that only about half of the start MCP area is utilized. This is true for all configurations of elevation angles and E/q steps tested, which is expected because the TOF section should be independent of the EA-IS settings. This impact area can also be seen in Figure 4.14, in a cut of the instrument TOF section.

The source of the issue in the TOF section causing the start and stop detectors to only utilize half of their active area is that the electrons generated from the carbon foil and SSD are not deflected properly by the Center Deflector. To correct this issue, the TOF section CAD model was modified to extend the center deflector 5mm further into the TOF section. Several different distances were simulated with the 5mm distance providing the best results. This modification and resulting simulation can be seen in Figure 4.15.

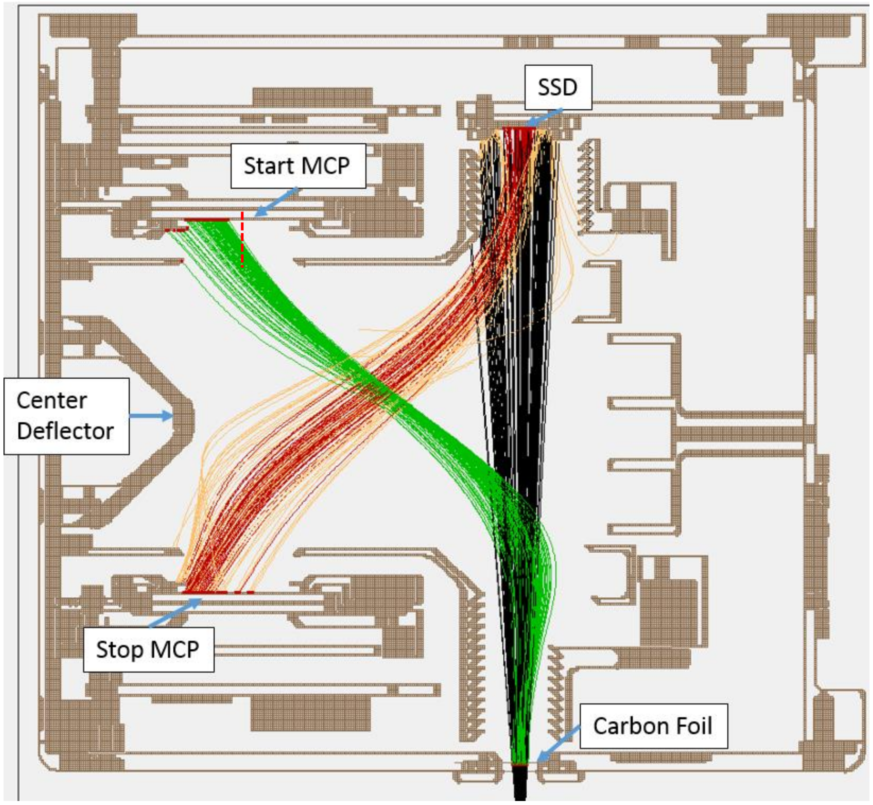

Figure 4.14: Particle flight path through TOF section illustrating the impact position in the start and stop MCP. Ions are shown in black, start electrons are shown in green, stop electrons are shown in red. The centerline of the start MCP is marked with a dotted red line.

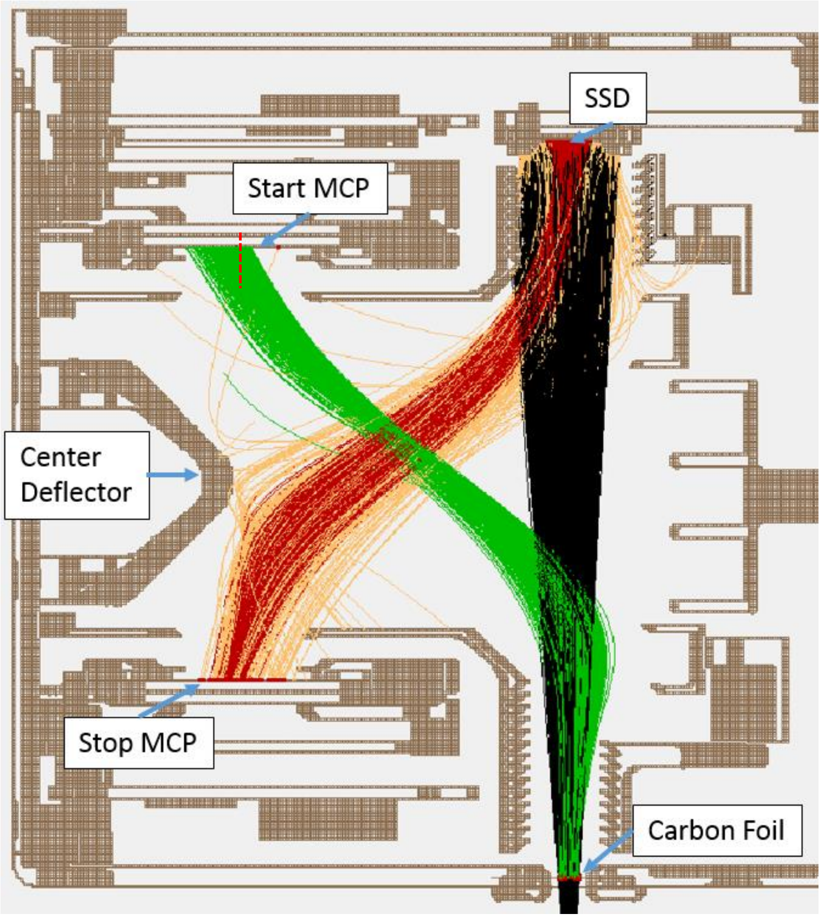

Figure 4.15: Modified TOF section with extended center deflector. Ions are shown in black, start electrons are shown in green, stop electrons are shown in red. The centerline of the start MCP is marked with a dotted red line.

In Figure 4.15 we can see that the modified deflector position better deflects the electrons on both the start and stop MCP, resulting in a better coverage of the detector area. A full simulation of this configuration with 400,000 test particles reveals that the start detector utilized >10% more of its detector area over the original design. The start and stop MCP detector maps can be seen in Figure 4.16. In this figure we can see that both the start and stop MCPs have more of their active area utilized over that of the original design.Although the extended center deflector does increase the amount of utilized area in the start detector, it still does not cover the full range of the detector. Further analysis of this configuration should be done to analyze if a change in the position of center deflector would result in negative effects in the TOF section, such as an over deflection of electrons or a loss of positional sensing resolution.

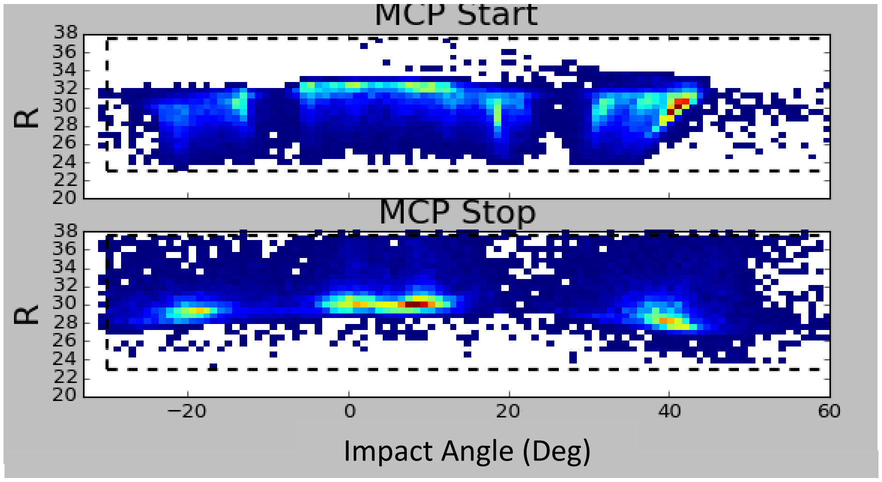

Figure 4.16: Start and stop MCP detector map for the modified TOF section design.

4.3.3. Carbon foil strut impedance on start MCP measurements

One of the design decisions made on HIS was to have structural struts as supports for the carbon foil. These supports were necessary to meet launch vibration requirements and prevent damage to the carbon foil during launch. These struts were place in two positions in the carbon foil area at -10° and 25°, as seen in Figure 4.17. The struts were placed at these two locations because they provide antiquate support while being located outside of the range of the expected bulk solar wind, minimizing their effect.

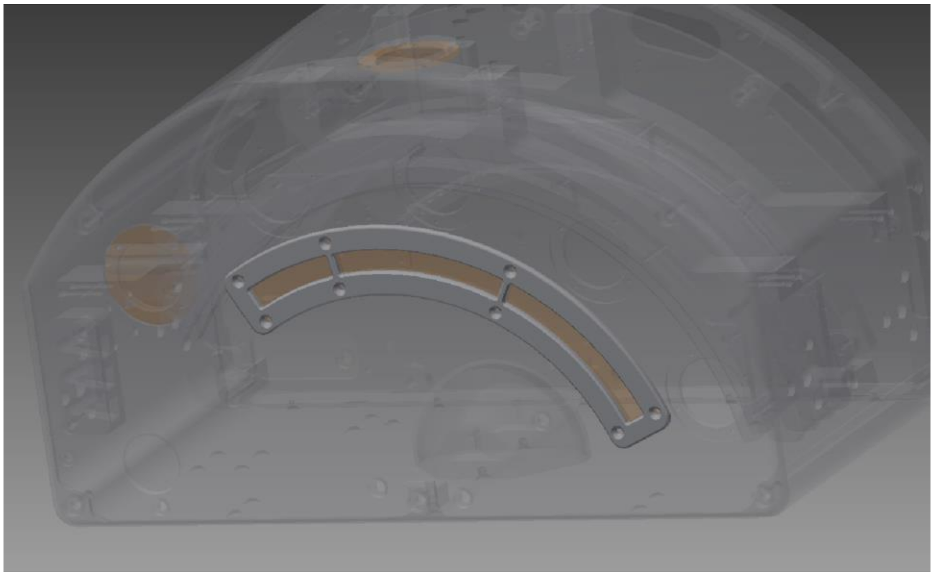

Figure 4.17: Time-of-flight section of the HIS instrument with the carbon foil and carbon foil struts highlighted. These carbon foil struts are located at azimuth angles -10° and 25°

The main drawback of these support struts are that they physically block ions that make it through the EA-IS, leading to loss of field of view in measurable ions.

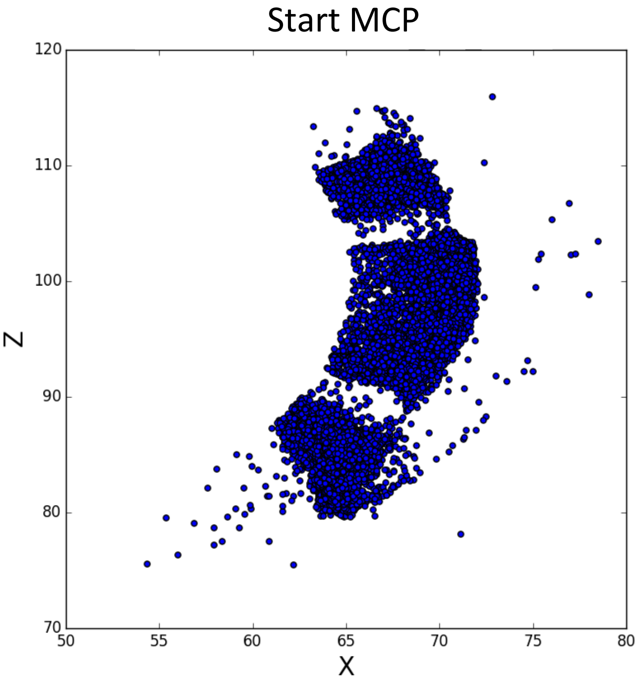

Figure 4.18: Start MCP electron impact location of 10,000 simulated particles through the HIS instrument.

Figure 4.18 demonstrates these blind spots in a simulation of 10000 ions hitting the start MCP. In this figure we can see that there are two clear areas in the MCP that are blocked by the carbon foil. The struts in the carbon foil are less than 2° wide, but seem to result in a loss of ion impact area on the start MCP of larger than 2°. Upon investigation, it was discovered that fringe electric fields at the edge of the struts were causing electrons created at the carbon foil to be deflected slightly. This slight deflection over the distance of the time-of-flight section of the instrument resulted in a magnification of the effect of the struts on the position sensing of the start MCP. Figure 4.19 shows this deflection of particles at the carbon foil. In Figure 4.18 electric potential contour lines were drawn every 25 V from -25000 V to -24825 V and can be seen as the colored line (with the first red line at -25000 V and the last blue line at -24825 V). Figure 4.20 shows a sketch of this same scenario.

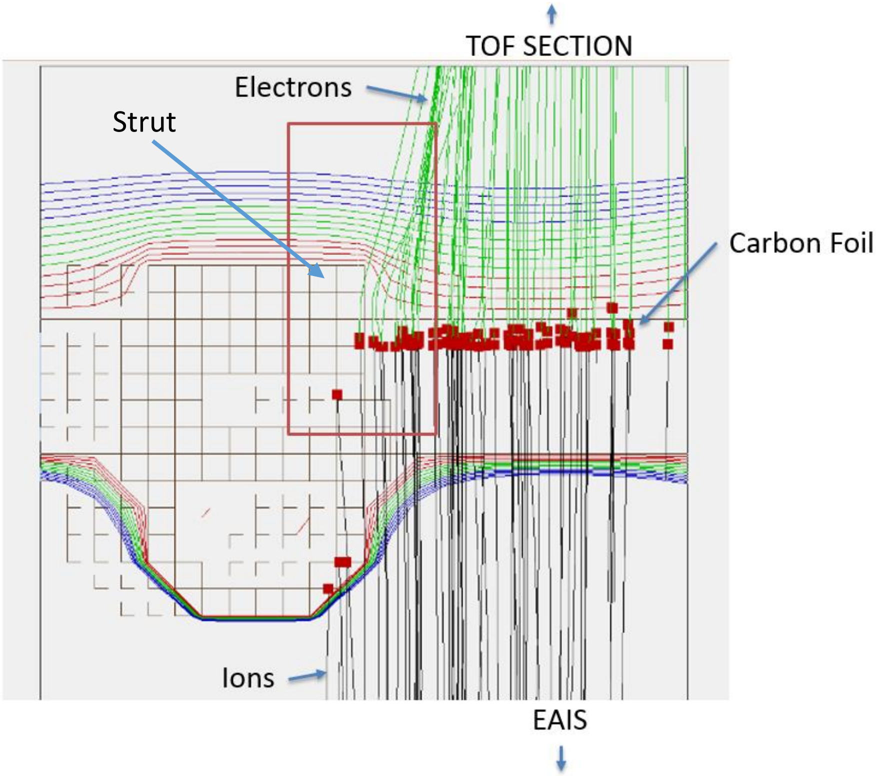

Figure 4.19: Electron deflection at the carbon foil due to fringe field. The colored lines (blue, green, red) are contours of the electric potential between -25000 V and -24825 V. The black lines are the ions that hit the carbon foil (at the red squares) and the green lines are the trajectory of the electrons generated at the carbon foil. The red box highlights the observed deflection of the start electrons due to the carbon foil strut.

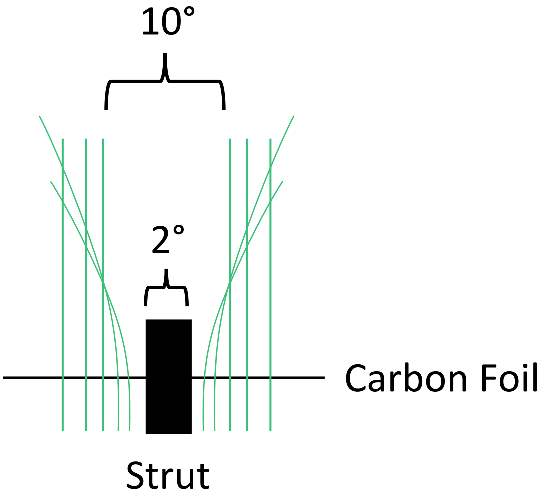

Figure 4.20: Sketch of the deflection caused by the impeding electric field from the carbon foil strut

To determine whether our theory about the deflection of the electrons at the carbon foil is causing the extended missing range of impact area on the start MCP, simulations were run with a grid inserted to hold off the voltage at the edges. This grid is held at the same potential as the housing of the carbon foil (-25000 V) resulting in it creating a field free region around the carbon foil.

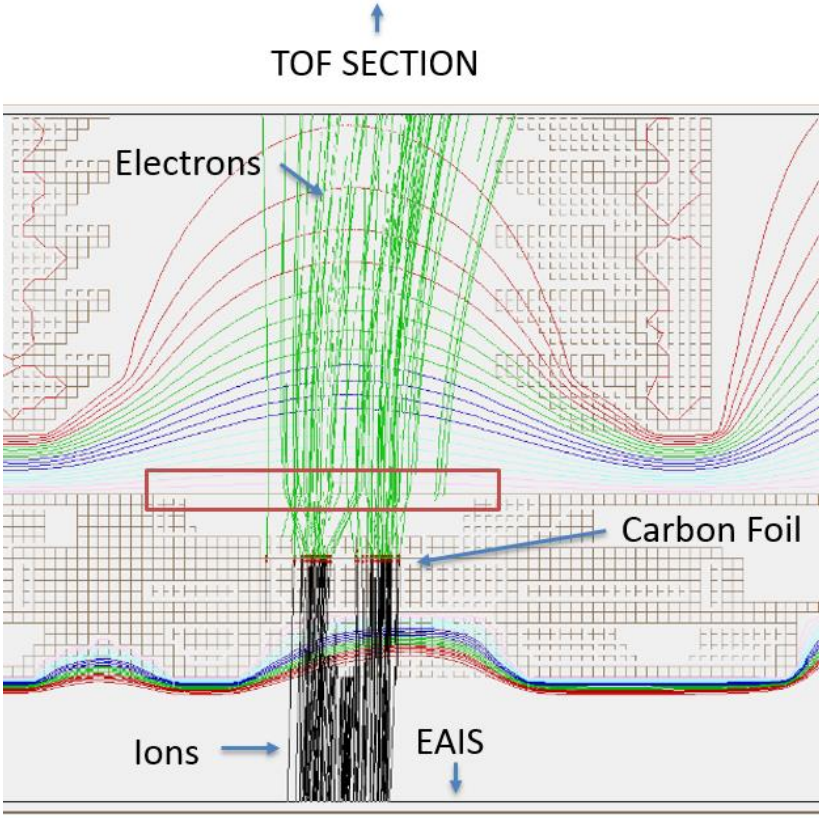

Figure 4.21: Flight path simulation with suppression grid at the carbon foil. The red box highlights the inserted grid at the exit of the carbon foil. The colored lines (blue, green, red) are contours of the electric potential between -25000 V and -24600 V, with a 50 V space between each line.

In Figure 4.21 a suppression grid is placed in the particle flight path just after the carbon foil (thin line outlined by red box). Electric potential contour lines are drawn every 50 V from -25000 V to -24600 V and can be seen as the colored line in figure 4.21 (with the first red line at -24600 V and the last pink line at -25000 V). Here we can see that there is still the expected random deflections off of the carbon foil, but no deflections from the fringe field that were created by the carbon foil struts. A re-examination of the start MCP impact figure shows that the large holes in the position sensing of the start MCP are no longer visible (Figure 4.22). The grid greatly reduces the missing locations in the impact area effects, therefore our hypothesis on the cause of this anomaly is correct and the suppression grid is able to reduce the problems caused by the carbon foil struts.

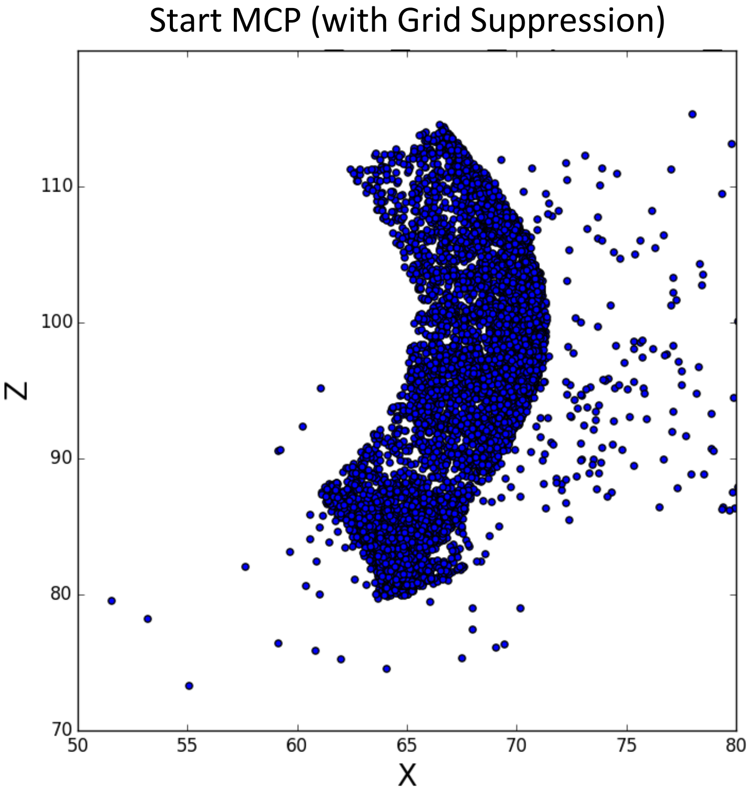

Figure 4.22: Start MCP hit position with suppression grid at the carbon foil

4.3.4. EA-IS post acceleration focusing

At the exit of the EA-IS there is a post acceleration region where the voltage changes from near 0 V to -25000 V over a small distance. This large change in voltage leads to an infringing electric field at the exit of the EA-IS, which can be seen in Figure 4.23. Due to this infringing electric field, the ions leaving the EA-IS experience a focusing where the focal point depends on the energy of the ions. Lower energy ions – such as the 1 keV/e ions in Figure 4.23 (LEFT) – have a focal point before the carbon foil. The higher the energy of the ions, the closer to the carbon foil the focal point becomes until it is beyond the carbon foil positon. This can be seen in Figure 4.23 (RIGHT) where the 5 keV/e ions have a focal point beyond the carbon foil. Once the focal point is beyond the carbon foil, the focusing of the ions is halted. This is because the ions pass through the carbon foil and are scattered in a random forward direction due to the properties of the carbon foil.

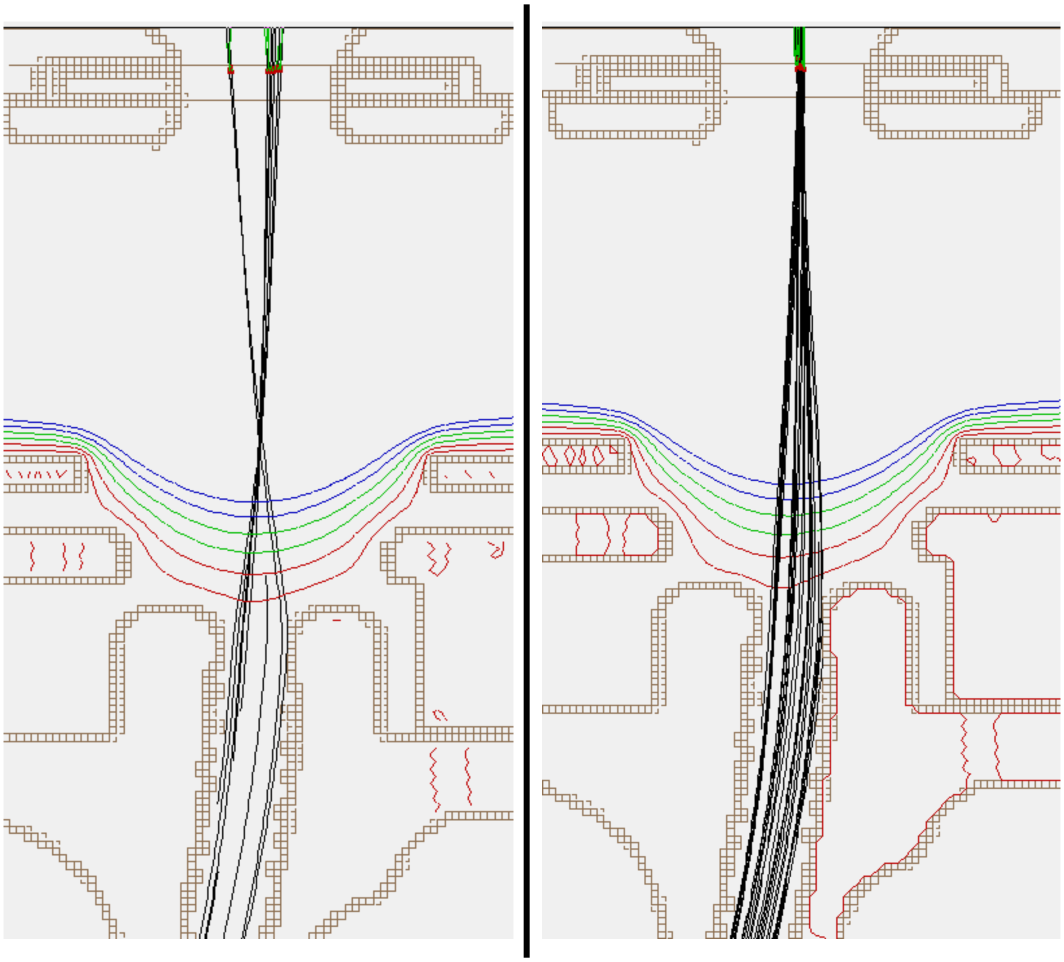

Figure 4.23: (LEFT) 1 KeV proton at the exit of the EA-IS showing the focusing due to infringing electric fields. The colored lines are several electric potential contour lines representing the background field (Red: 0V -500V, -1000V; Green: -1500V -2000V; Blue: -2500V, -3000V). (RIGHT) 5 KeV protons at the exit of the EA-IS showing that the focusing point is past the carbon foil.

The focusing of the ions has a great effect on the efficiencies in the TOF section. The efficiencies are discussed later in section 4.5. At low energies the focusing causes a large spread of the ions that leads to impact on surfaces surrounding the SSDs and subsequent emission of secondary electrons. These secondary electrons can then cause stop signals, leading to shorter TOF recordings. This can be seen in Figure 4.14 and 4.15, where the black lines are the ions, the red lines are electrons created off the SSD, and the yellow lines are secondary electrons created off any other surface. The effect of this focusing will need to be characterized in the calibration of the instrument since it has a large effect on the TOF section efficiencies (as discussed in section 4.5).

4.4. Geometric Factor

4.4.1. Phase space count distribution derivation

Calibration of the instrument is necessary to establish a relationship between the instrument measurements and actual plasma parameters being measured. The instrument is measuring total counts for a given E/q and elevation angle (θ) step. The first step is to relate the counts, C, that are seen to the phase space density of dimension $d^3x\, d^3v$, where d^3x is the volume element in configuration space and d^3v is the volume element in velocity space.

$$dC = f(\boldsymbol{x}, \boldsymbol{v})\, d^3x\, d^3v \tag{4.3}$$

Where $f(\boldsymbol{x}, \boldsymbol{v})$ is the particle distribution in a phase space element of dimension $d^3x\, d^3v$. Integrating this over the volume gives us the total counts in that volume.

$$C = \int_v \int_x f(\boldsymbol{x}, \boldsymbol{v})\; d^3x\, d^3v \tag{4.4}$$

From here we know that the instrument will collect particles that will pass through an area A in a time Δt. This allows us to convert one of the spatial integrals to an integral over time by substituting $dz = v\hat{\boldsymbol{v}}dt$ and $dx\, dy = \hat{\boldsymbol{n}}\, dA$.

$$dx\, dy\, dz = v\hat{\boldsymbol{v}} \cdot \hat{\boldsymbol{n}}\, dA\, dt \tag{4.5}$$

Here $(\hat{\boldsymbol{v}} \cdot \hat{\boldsymbol{n}}\, dA)$ is the projection of the aperture area towards the velocity direction which can be simplified to

$$\hat{\boldsymbol{v}} \cdot \hat{\boldsymbol{n}}\, dA = \cos\theta_v \cos\varphi_v\, dA \tag{4.6}$$

Where θ_v is the elevation angle between the velocity vector and the projected aperture area, and φ_v is the azimuth angle between the velocity vector and the projected aperture area (Wuest et al. 2007). Putting this all together and assuming that the velocity distribution function f is uniform over the aperture yields the total counts.

$$C = \int_{\boldsymbol{v}} \varepsilon\, v\, f(\boldsymbol{v}) \cos\theta_v \cos\varphi_v\, A(\boldsymbol{v})\, \Delta t\, d^3v \tag{4.7}$$

Here ε was included to account for the efficiency of the detection of particle in the TOF section. We now express eq. 4.7 in spherical coordinates in eq. 4.8 and grouped the like terms in eq. 4.9.

$$C = \int_v \int_\theta \int_\varphi \varepsilon\, v\, f(v,\theta,\varphi) \cos\theta_v \cos\varphi_v\, \Delta t\, A(v,\theta,\varphi)(dv)(v d\theta)\left(v sin\left(\frac{\pi}{2}-\theta\right) d\varphi\right) \tag{4.8}$$

$$C = \Delta t \int_{\boldsymbol{v}} \int_\theta \int_\varphi \varepsilon\, f(v,\theta,\varphi\,) \cos\theta_v \cos\varphi_v\, A(v,\theta,\varphi)\, v^3 cos\theta\, dv\, d\theta\, d\varphi \tag{4.9}$$

Here we have defined the counts the instrument would see for a given phase space distribution.

4.4.2. Geometric Factor Derivation

Often it is useful to describe the instrument in terms of geometric factor, G, which is a quantity that collects all of the dependent variables in the EA-IS section. The geometric factor is a term that has been used in the past to compare the measurements of different instrument. In order to do this we must return to the differential counts equation 4.3.

$$dC = f(\boldsymbol{x},\boldsymbol{v})\, d^3x\, d^3v \tag{4.10}$$

Taking the same substations as before we put eq. 4.5 and eq. 4.6 into eq. 4.10

$$dC = f(\boldsymbol{x},\boldsymbol{v})\, \varepsilon\, v\, cos\,\theta_v\, cos\,\varphi_v\, dA\, dt\, d^3v \tag{4.11}$$

We now express this in spherical coordinates

$$dC = f(v,\theta,\varphi)\ \varepsilon\, v\, cos\,\theta_v\, cos\,\varphi_v\, A(v,\theta,\varphi)(dv)(vd\theta)(vsin\left(\frac{\pi}{2}-\theta\right)d\varphi)dt \quad (4.12)$$

With the same assumption that the velocity distribution function f does not change within a pixel we can write

$$\Delta C = \varepsilon\, A(\mathrm{v},\theta,\varphi)\ \cos\theta_v \cos\varphi_v\ f(\mathrm{v},\theta,\varphi)\ v^3\ \cos\theta\, \Delta\theta\Delta\varphi\Delta v\Delta t \qquad (4.13)$$

From here we can derive the energy resolution of the instrument, δ. The energy resolution of the instrument is a quantification of what energy range is measured for a given step. A large energy resolution will allow a broader range of E/q values to be measures, allowing for more counts, but reducing the known energy per charge value of those counts.

$$\frac{E}{q} = \frac{1}{2}\frac{m}{q}v^2 \qquad (4.14)$$

$$d\left(\frac{E}{q}\right) = \frac{mv}{q}dv \qquad (4.15)$$

$$\frac{d\left(\frac{E}{q}\right)}{\frac{E}{q}} = \frac{\frac{mv}{q}dv}{\frac{1}{2}\frac{m}{q}v^2} = \frac{2dv}{v} \qquad (4.16)$$

$$\frac{\Delta\left(\frac{E}{q}\right)}{\frac{E}{q}} = \delta = \frac{2\Delta v}{v} \qquad (4.17)$$

$$\Delta v = \frac{1}{2}\delta\, v \qquad (4.18)$$

Where E is the energy, q is the charge, m is the mass, and v is the velocity. Substituting eq. 4.18 into eq. 4.13

$$\Delta C = \frac{1}{2}\varepsilon\, A(\mathrm{v},\theta,\varphi)\ \cos\theta_v \cos\varphi_v\ f(\mathrm{v},\theta,\varphi)\ \delta\, v^4\ \cos\theta\, \Delta\theta\Delta\varphi\Delta t \qquad (4.19)$$

From here we can extract the geometric factor of the instrument, G.

$$G = A(\mathrm{v},\theta,\varphi)\ \delta\ \cos\theta_v \cos\varphi_v \cos\theta\, \Delta\theta\Delta\varphi \qquad (4.20)$$

$$\Delta C = \frac{1}{2} \varepsilon \, G(\mathrm{v}, \theta, \varphi) \; f(\mathrm{v}, \theta, \varphi) \; v^4 \Delta t \tag{4.21}$$

In equation 4.20, δ is the energy resolution, $\Delta\theta$ is the elevation passband, $\Delta\varphi$ is the azimuthal passband, and ε is the efficiency of the TOF section. With a known geometric factor and distribution function, the total counts that the instrument observes can be calculated with equation 4.21. To use eq. 4.21 in the simulations we must first calculate the geometric factor of the instrument in section 4.4.4. The first step to calculating the geometric factor is to determine the energy resolution, δ, and elevation passband, $\Delta\theta$, which is done in section 4.4.3.

4.4.3. Energy and Elevation resolution

One of the main parameter that is incorporated into the final geometric factor is the energy resolution, δ. The energy resolution was derived in section 4.4.2 and can be seen in equation 4.17. At a given E/q setting on the instrument there is a range of E/q values that can make it through the EA-IS section, this range is the energy resolution. This range is due to particles that have slightly less energy per charge (or slightly greater energy per charge) than the set energy still having a path through the EA-IS. This range of energy values allows for more particles to be detected, but at a trade-off with the resolution of the energy per charge that can be ultimately associated with the measurements. To determine the energy resolution of the instrument we carried out a Monte Carlo simulation where the initial position, E/q, elevation angle, and azimuthal angle are varied around a pre-determined E/q and elevation angle step. In this simulation 500,000 particles were generated uniformly between 0.5 keV/e and 1.5 keV/e and between -5° and 5°. Due to the nature of the instrument the energy resolution and elevation resolution are dependent on each other and must be taken into account when calculating these terms.

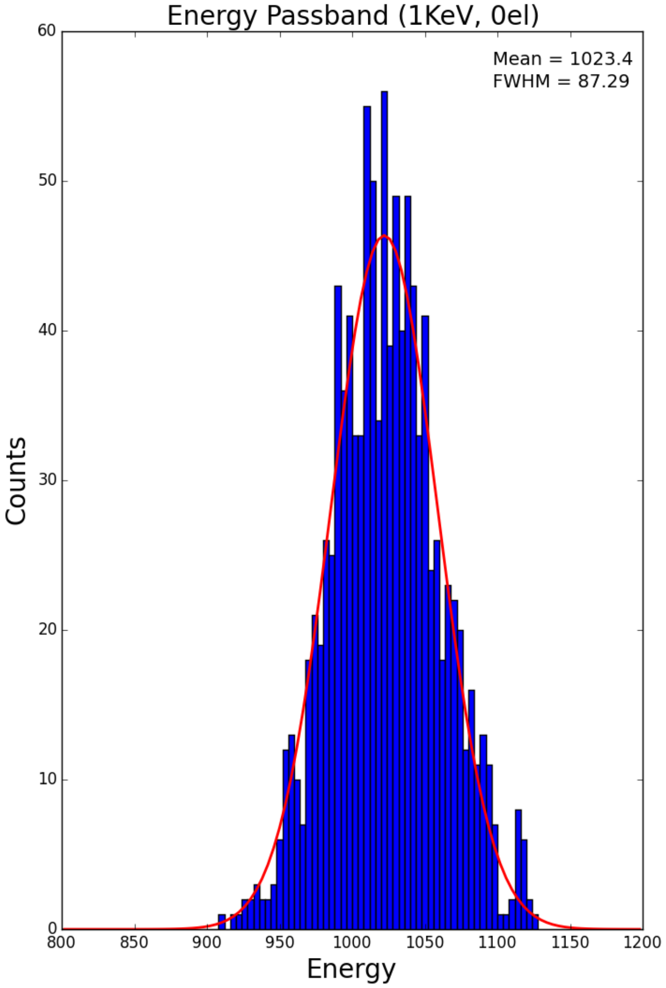

Figure 4.24: Energy passband of HIS set for particles at 1 keV/e and 0° elevation angle

Figure 4.24 reveals a couple of important facts about the instrument. First, at the energy setting of 1000 eV/e, the mean energy, E_o, that makes it through the instrument has an energy per charge of 1023.4 eV/e. This mean energy is higher than the set E/q but only by 2.3%. The other piece of information gathered through this simulation is the full width half maximum (FWHM) of this energy curve. This FWHM is equivalent to the energy passband of the instrument, *ΔE/q*, in equation 4.17. With this information we can calculate the energy resolution δ as 8.7%, which is equal to the FWHM divided by the centroid. This energy resolution is close to the required resolution for the level 1 requirements of around 8%. From the same simulation we can also plot the elevation passband in figure 4.25.

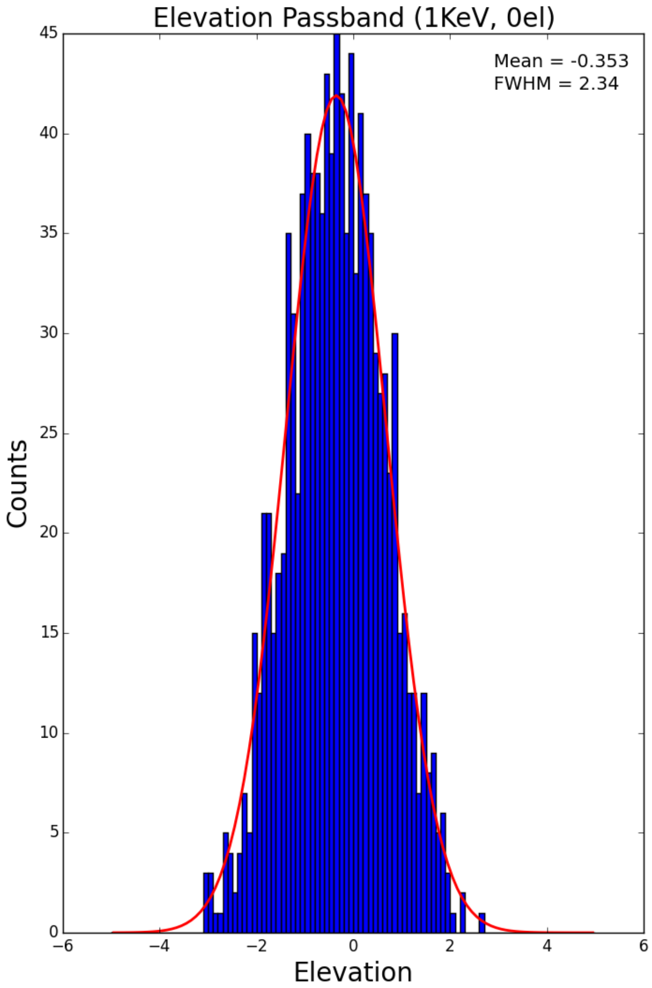

Figure 4.25: Elevation passband for HIS set for particles at 1 keV/e and 0° elevation angle

Similar to the energy resolution, the instrument also has an elevation resolution, or in this case an elevation passband. In figure 4.25 we can see that for a given instrument setting at 0° elevation, ions up to 3° degrees in either direction can make it into the instrument. The elevation passband, Δθ, is equal to the FWHM of this simulation, 2.34° which is much less than the level 1 requirements of 6°.

Ideally, the instrument would have a constant energy and elevation resolution over all E/q and elevation steps, but due to the complex geometry of the EA-IS there are variabilities in both the energy resolution and elevation passband over the measurement range of the instrument. Although the final E/q and elevation voltage settings have not been completed with the HIS instrument, several voltage settings have been determined to facilitate the initial process of determining the variability in the energy resolution and elevation passband. A total of 10 different steps have been initially optimized ([1, 5] keV/e, [-10, -5, 0, 5, 10]° elevation). The calculation of the energy resolution and elevation passband have been carried out identically to the 1 keV/e, 0° elevation angle case described above.

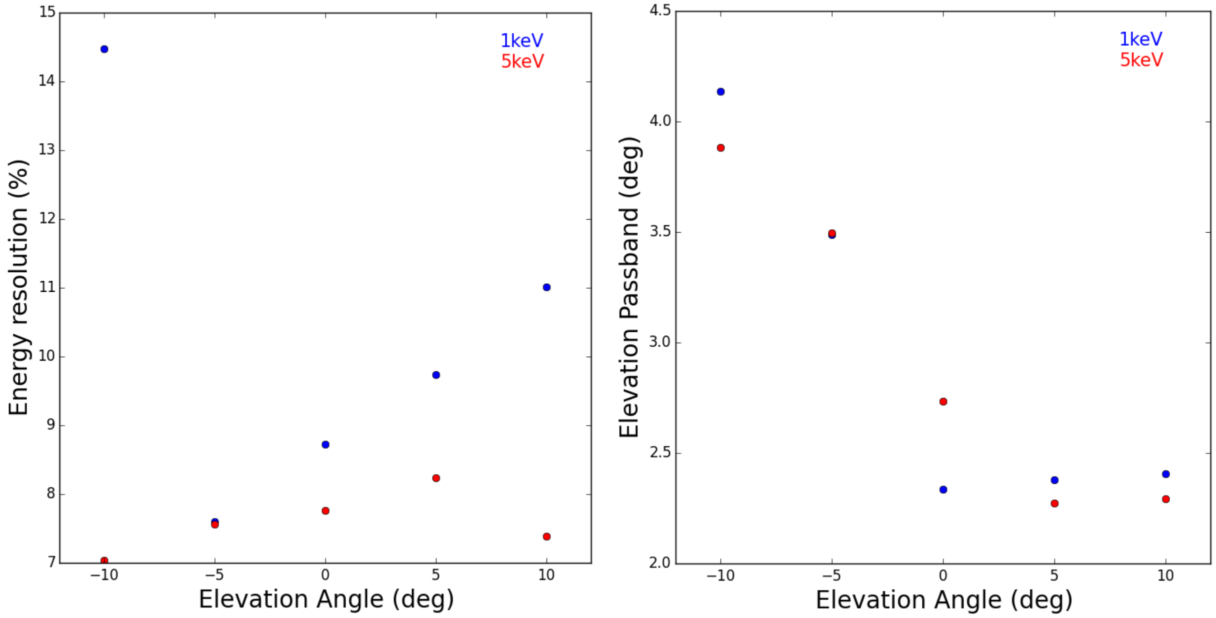

Figure 4.26: (LEFT) Energy resolution vs. elevation angle and (RIGHT) Elevation angle vs. elevation passband angle for 10 Monte Carlo simulations of the EA-IS system on HIS.

In figure 4.26 (LEFT) we can see the elevation angle vs. the energy resolution of the HIS instrument over various steps. When examining the figure we notice that the energy resolution varies both as a function of elevation angle and as a function of E/q. Figure 4.26 (RIGHT) shows the elevation passband for the various steps. In this figure we notice that the elevation passband has less of a dependence on the E/q than it does with the elevation angle. Both the 1 keV/e and 5 keV/e simulations are within 15% of each other at the same elevation step, with more than half of them being within 5% of each other.

Other than the negative elevation angles the elevation passband is relatively constant with E/q and elevation angle. Upon investigation of the elevation passband at -10°, it was found that this extended passband was caused by a rather large acceptance angle in the negative direction. Figure 4.27 shows the elevation passband for the instrument set at 1keV/e, -10°. A Gaussian was fit to the core of the distribution (red line). This Gaussian fit shows that the core of the accepted elevation angles has a FWHM of 2.35, similar to the other simulations seen in figure 4.26 (RIGHT). Adjusting the voltages for this setting on the instrument could result in elimination of the tail, ideally leaving only the core of the accepted elevation angles fitted here. If done properly the elevation passband could possibly be a constant over E/q and elevation angle.

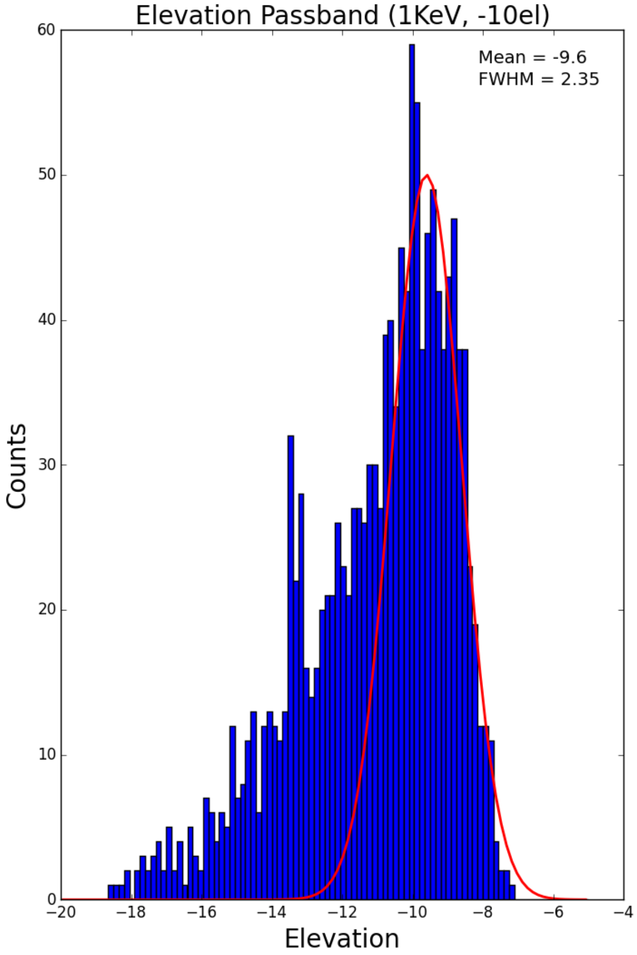

Figure 4.27: Elevation passband for HIS set at 1 keV/e and -10°. The main core of the distribution was fitted (red line). It was determined that the extended tail was causing a widening of the elevation passband at this low angles.

4.4.4. Geometric Factor Simulation

From equation 4.9 we use the SIMION model to calculate the effective geometric factor of the instrument. To do this we input ions into the SIMION model in an evenly distributed velocity distribution function making f constant over E/q, θ, and φ, and collect the counts that make it through in EA-IS at the various E/q, θ, and φ steps.

Following the work of Collinson et al. 2012 we determine the geometric factor of the instrument using a simulation by creating a known amount of particles (N_{in}) on a source surface (of size A_{suf}) in front of the aperture of the instrument, making sure to cover all extents of the instruments aperture area. We then measure the particles that navigate through the EA-IS and hit the carbon foil (C_{out}). With these measurements we can find the geometric factor using the following formula from Collinson et al. 2012.

$$G = \frac{C_{out} A_{suf} \bar{E} \cos^2 \theta \Delta E \Delta\theta \Delta\varphi}{N_{in} E_o^2} \tag{4.22}$$

Where $\bar{E}$ is the average energy of the simulation, $\Delta\theta$ is the elevation width of the beam, $\Delta\varphi$ is the azimuthal width of a detection pixel, ΔE is the energy width of the beam, and E_o is the peak collection energy. Equations 4.20 and 4.22 are equivalent, with equation 4.22 being in terms of known quantities for the simulation. In the simulation particles were generated at the surface of the entrance aperture of the instrument. Generating the particles right at the surface rather than in front of the surface ensures that every particle enters the entrance of the instrument rather than have some of the particles miss the entrance completely. Care has to be taken to make sure that the particles generated at this surface cover all possible entrance trajectories into the instrument, an assumption that was made in equation 4.22. Generating the particles in this way drastically reduce the amount of particle needed to simulate all possible trajectories This was important because the processing of the flight paths of the particles required a significant amount of computational power. In the end, the total number of particles that fly through the instrument at each azimuth angle needed to be statistically significant to produce the distributions required to characterize the energy and elevation bandpass (i.e. on the order of a couple of hundred counts). This required on the order of a million particles to be simulated. The set range of E/q and elevation angles are ΔE and Δθ in equation 4.22, respectively.

The geometric factor is a function of E/q, elevation angle, and azimuth angle. Several simulations were carried out at given E/q and elevation steps. The instrument is able to measure all azimuth angles at the same time without stepping, therefore this parameter can be extracted from the simulations during processing. In order to calculate the total geometric factor of the instrument we define 16, 6° pixel's in azimuth and calculate the geometric factor for each of the 6° pixel. These pixels were found by dividing the surface at the exit of the EA-IS. This 6° pixel is $\Delta\varphi$ in equation 4.22. In order to keep the small angle approximation made in the formulation of equation 4.22, the area of the particle source surface (A_{suf}) for the simulation needed to be relatively small in angular extent. To accomplish this the particles that were seen to hit the surface at the end of the EA-IS were traced back to their origins at the aperture surface. The FWHM of the extent of the particles locations on the particle source surface was calculated and the corresponding particle source surface was known. Only particles that were generated within this area were considered in the calculation of the geometric factor for this azimuthal pixel.

Figure 4.28 shows how this particle source surface is found. In this figure the bottom panel shows the impact angle on the carbon foil for particles measured between 0° and 6° in the azimuthal direction for an E/q setting of 1keV/e and 0° elevation. The top panel shows the initial position of the particle that hit the carbon foil between these azimuth bounds. This extent is larger than the 6° measurement window because particles entering the instrument slightly off from the ideal curve can still make it through the instrument. Care has to be taken when reading this figure to not confuse the impact position with the azimuthal angle of the particles. All of the particles seen in this figure have an azimuth angle between 0° and 6°. In this figure the two dotted red lines mark the extent of a FWHM of the initial position. This value is used as the particle source area. All of the particles that are generated within this initial position are run through the model to determine what fraction of them hit the 0° to 6° azimuthal position on the carbon foil.

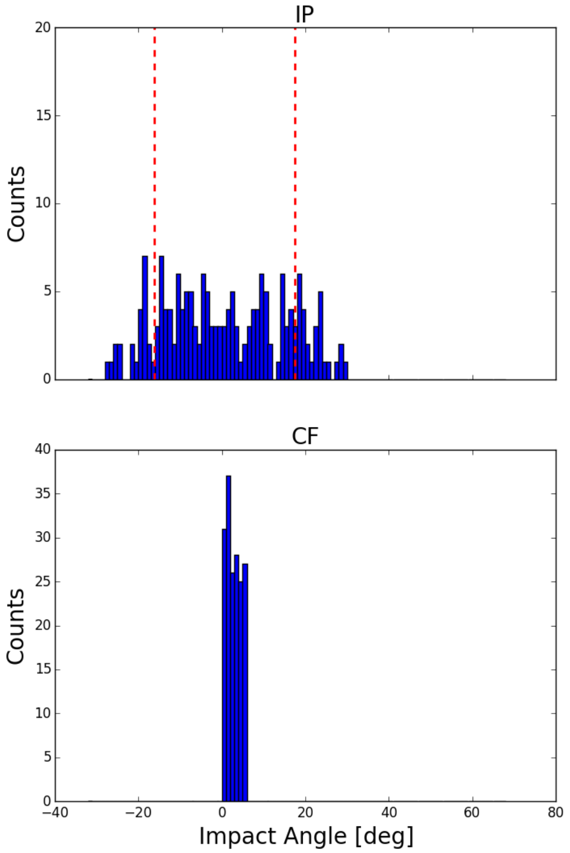

Figure 4.28: Determination of the initial position of particle that hit the carbon foil between a 0° and 6° azimuthal angle. The top panel shows where these particle initially were positioned. The red dotted lines mark the FWHM of this initial position, which is used at the extent of the particle source area in the calculation of the geometric factor.

From here we know the total number of particles that were flown from the source surface area (N_{in}) and the total number of particles that hit our azimuthal pixel at the end of the EA-IS, C_{out}. Finally, the only inputs left in the geometric factor calculation are the peak collected energy, E_o, and the peak collected elevation angle, θ. Both these inputs can be taken from the output of the passband calculation done in section 4.4.3. The outputs from 1keV/e, 0° and 5keV/e, 0° simulations are seen in figure 4.29. Here we can see that there is variability in the geometric factor with azimuth angle, particularly at the edges of the field of view. The geometric factor per azimuthal pixel can be seen in table 4.1.

Table 4-1: The maximum and minimum geocentric factor (GF) per azimuthal pixel for 1 keV/e and 5 keV/e measurements

	Minimum GF per Azimuthal Pixel [cm^2-sr-eV/eV]	Maximum GF per Azimuthal Pixel [cm^2-sr-eV/eV]
1 keV/e	1.7 x 10^{-6}	4.6 x 10^{-6}
5 keV/e	3.1 x 10^{-7}	4.2 x 10^{-6}

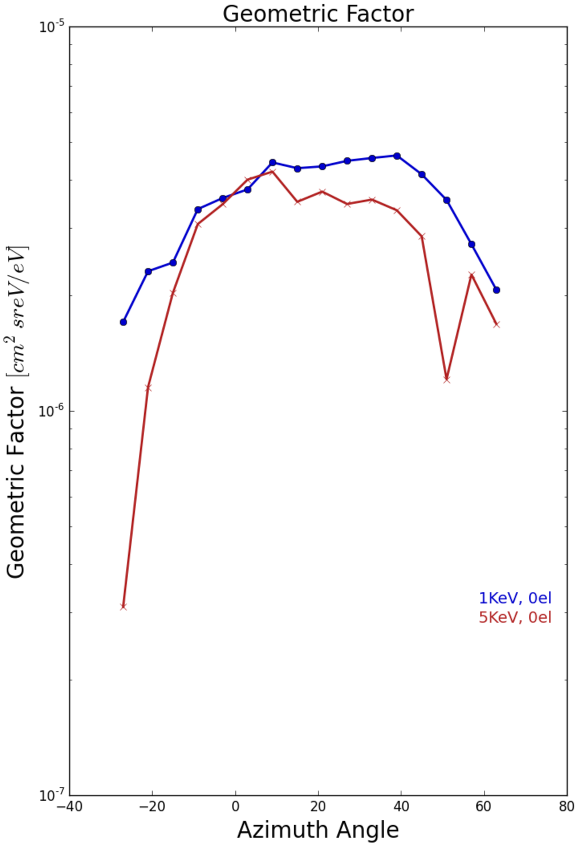

Figure 4.29: Geometric factor vs. azimuth angle for a simulation of the HIS instrument 1 keV, 0° (blue) and 5 keV, 0° (red)

Summing the geometric factor of each azimuthal pixel will give the overall geometric response of the instrument of 5.6 x 10^{-5} cm^2-sr-eV/eV at the 1 keV/e, 0° elevation step and 4.38 x 10^{-5} cm^2-sr-eV/eV for the 5 keV/e case. When the extreme azimuthal angles are taken out of the 1 keV/e case the difference in the geometric factor per azimuthal pixel is less than 30%. The difference in the overall geometric factor the two cases is only 22%. Although there is variability in the geometric factor with azimuth angle and E/q, this simulation tells us that it's relatively small.

Examining the full range of model simulations shows the variability over a larger range of instrument settings. Figure 4.30 (LEFT) shows the geometric factor for 5 different settings at 1 keV/e (at -10°, -5°, 0°, 5°, 10° elevation). Figure 4.30 (RIGHT) shows the geometric factor for 5 different setting at 5 keV/e (at -10°, -5°, 0°, 5°, 10°). In these figures we can see that there exists a variability in the geometric factor as a function of elevation angle. As the instrument observes ions farther from the 0° elevation line, the geometric factor of the instrument is reduced.

The geometric factor of the instrument relies heavily on how well the instruments voltages were tuned. The voltages used in this study are not the final voltages of the instrument. In general, the calculation of the geometric factor provided here should be looked at as a worst case scenario for the geometric factor because fine tuning the voltages in calibrations should drastically improve how many ions are able to navigate through the instrument. In particular, the 5° elevation case seen in figure 4.30 (LEFT and RIGHT) seems to be a poorly tuned voltage set, and the results from this analysis show that tuning the voltages should be done with caution to produce the best geometric factor.

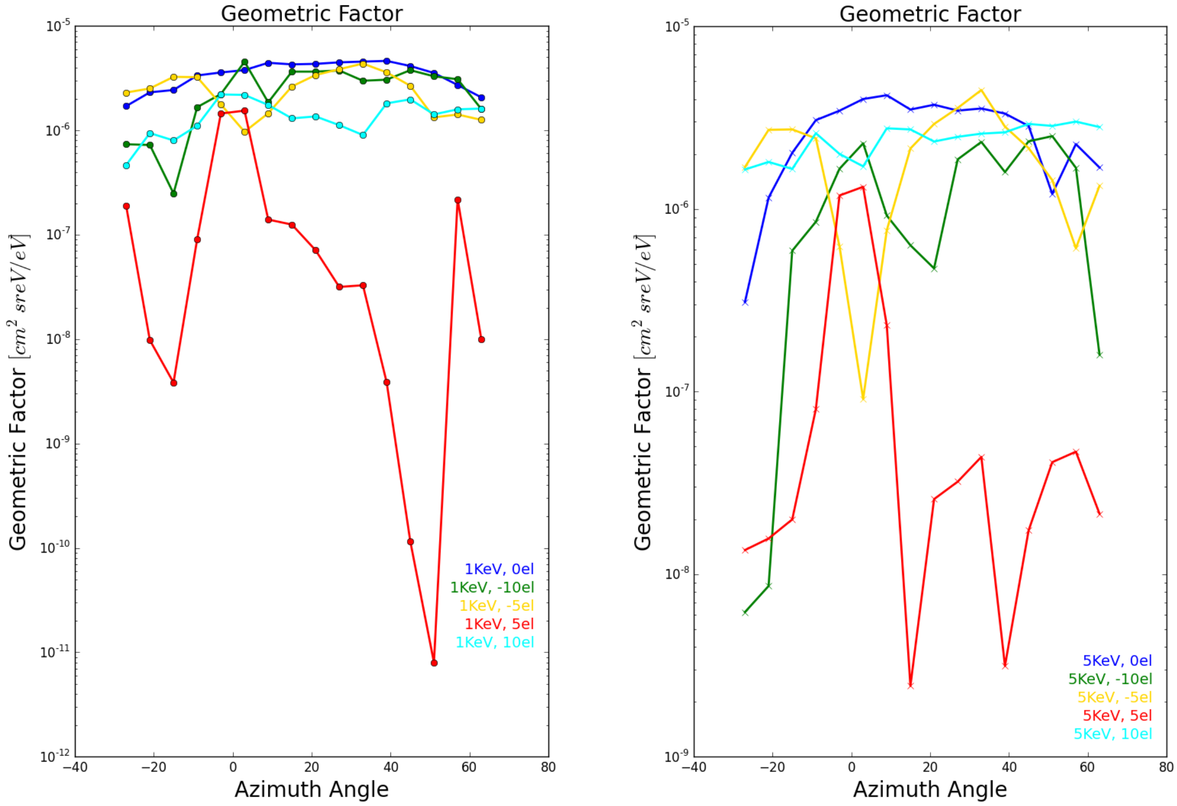

Figure 4.30: (LEFT) Geometric factor for 5 different settings at 1 keV (at -10° (green), -5° (gold), 0° (blue), 5° (red), 10° (cyan) elevation). (RIGHT) Geometric factor for 5 different settings at 5 keV (at -10° (green), -5° (gold), 0° (blue), 5° (red), 10° (cyan) elevation)

4.5. Efficiency characterization

The final thing left to characterize in the instrument is the efficiency of the TOF section. In section 4.4 we were able to calculate the geometric factor of the instrument, which characterizes the EA-IS section of the instrument. Calculating the efficiency of the instrument will allow us to characterize the TOF section. In equation 4.8 we can see the efficiency term, ε, plays a major role in the final counts seen by the instrument. This term collects all of the factors that lead to a particle entering the TOF section and not triggering a measurement. The main two factors that lead to particle not triggering a measurement once in the TOF section are: 1) The particle missing the detection surface and hitting a wall; 2) The particle hits the detector but does not trigger a measurement. With the SIMION model we are able to characterize the first factor. Simulations were run including the EA-IS section of the instrument because the focusing at the exit of the EA-IS plays a large role on the particles that enter the TOF section and miss a detector. The efficiencies in the TOF section could depend on the E/q step, elevation step, and the azimuthal angle.

In order to accurately characterize the TOF section, several simulations were run at the different E/q and elevation steps similar to the Monte Carlo simulations evaluated for the geometric factor (section 4.4.4). Figure 4.31 is a plot of the efficiencies calculated from 10 simulations. Two E/q settings (1 keV/e plotted as the solid lines with filled circles, and 5 keV/e plotted at the dashed lines with filled diamonds) were simulated over 5 elevations angles (0° - blue, 10° - green, 5° - gold, -5° - red, -10° - cyan). The SSD efficiencies are shown in the top left, the start and stop MCP efficiencies are shown in the left and right middle, respectively, and the time of flight and triple coincidence efficiencies are shown on the left and right bottom, respectively. The efficiencies were calculated based on the number of particles that hit the azimuthal range divided by the number of particles that exited the EA-IS section over those azimuthal angles (for the purposes of this simulation, a 6° azimuthal angle was considered when calculating the efficiencies). This calculation results in a percent of particles that hit the detectors based on the number of particle that made it through the EA-IS to the carbon foil.

There are different properties of the instrument that affect the instrument efficiencies of the various detectors. As discussed in section 4.1.2, the SSD measures the neutralized ions exiting the carbon foil. When passing through the carbon foil, these ions are scattered upon exiting. This leads to a reduction in efficiencies and must be captured in this simulation. The focusing at the exit of the EA-IS has the largest effect on the SSD efficiencies because it directly effects the flight path of the particles that will eventually hit the detector.

The start MCP detects electrons that are scattered off of the carbon foil. The TOF optics does an excellent job of guiding these electrons to the start MCP, having a near 100% detector efficiencies over most of the detector range. The only azimuth angles where this efficiency drops is at the angles that include the carbon foil struts and at the very extreme angles of the instrument (a problem discussed in 4.3.3).

The stop MCPs efficiencies are closely tied to the SSD efficiencies because the electrons used to trigger a signal in the stop MCP are generated at the SSD. For example if an ion that never hits the SSD then it will not produce a stop electron to trigger the stop MCP. Ions that hit the wall near the SSD, but not the detector itself, can still scatter electrons that are guided to the stop MCP and trigger a stop signal. These stop signals will not have an SSD measurement associated with them and may have a shorter distance and time of flight. This results in errors in the time of flight calculation of the ions.

The time of flight measurement is valid when both a start and stop signals are triggered (see eq. 4.1). Because of this fact, the time of flight efficiencies are directly tied to the start and stop MCP efficiencies. Only when a measurement is triggered at both the start and stop MCPs is the time of flight measurement recorded.

Finally, the triple coincidence measurement of the instrument is the culmination of all 3 detectors. This measurement takes into account the time of flight of the particle and the total energy deposited at the SSD. Because of the necessity of all 3 measurements the triple coincidence efficiencies are directly tied to the efficiencies of all 3 detectors. This results in the triple coincidence efficiencies being the lowest out of all of the TOF section efficiencies.

In figure 4.31 there are two groups of lines that correspond to two different E/q settings on the instrument. From the grouping of the simulations in this figure we can conclude that the E/q setting on the instrument has a larger effect on the efficiencies than the elevation setting. This is not entirely unexpected. We know from section 4.3.5 that the focusing that occurs at the exit of the EA-IS is dependent on the E/q of the ions, with smaller E/q corresponding to larger focusing. This focusing leads to particles missing the SSD in the TOF section. Knowing this we would expect there to be a dependence of E/q on the efficiencies in the TOF section, with the lowest E/q settings having the lowest efficiencies.

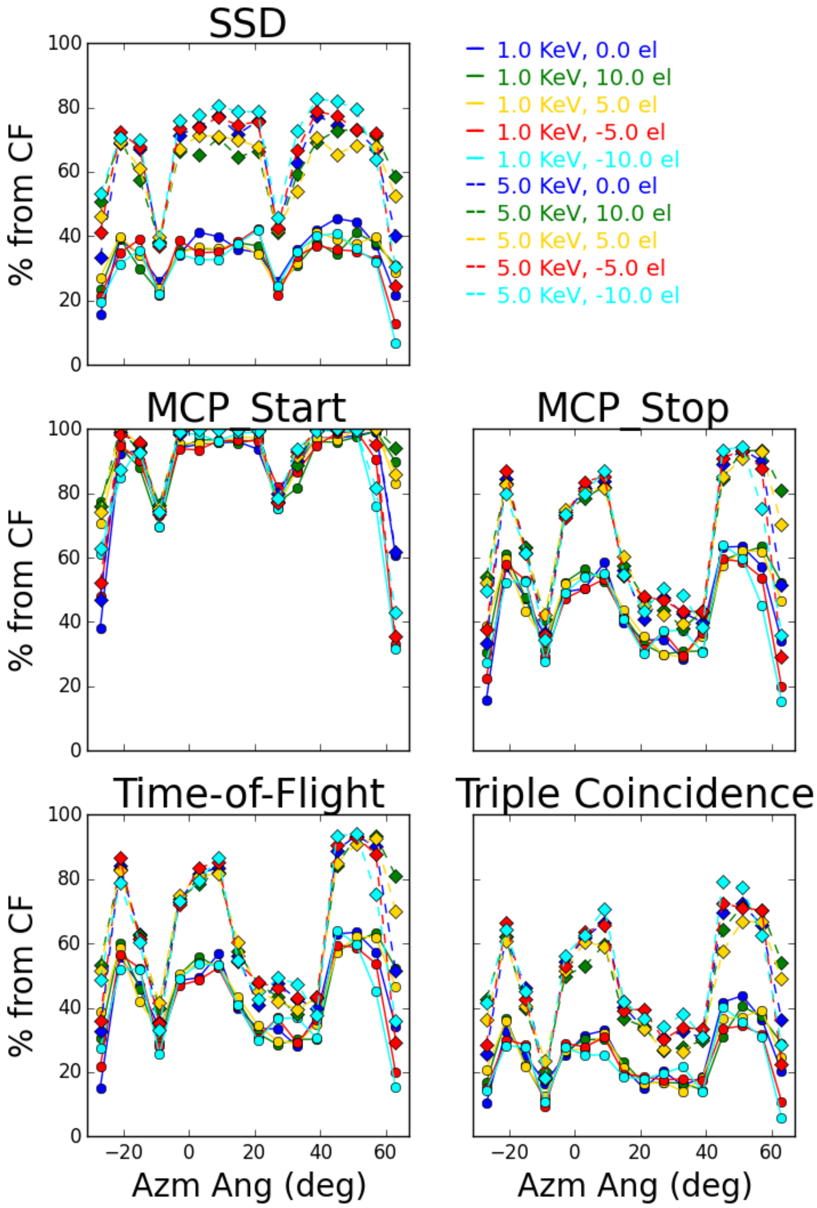

Figure 4.31: Efficiencies of the HIS instrument over several E/q and elevation steps. Two E/q settings (1 keV plotted as the solid lines with filled circles, and 5 keV plotted at the dashed lines with filled diamonds) were run over 5 elevations angles (0° - blue, 10° - green, 5° - gold, -5° - red, -10° - cyan). The SSD efficiencies are shown in the top left, the start and stop MCP efficiencies are shown in the left and right middle, respectively, and the time of flight and triple coincidence efficiencies are shown on the left and right bottom, respectively.

The second thing that we notice from figure 4.31 is that there are certain angles that see large drops in the efficiency. These angles (around 25° and -10°) encompass the locations of where the carbon foil struts are located (as discussed in section 4.3.3). Finally, this figure shows that there is an elevation angle dependence on the efficiencies, although the E/q dependence is significantly larger than the elevation dependence. This can be seen most clearly in the SSD panel in the 5 keV/e simulations. In this panel we can see that the lowest elevation angles have the highest efficiencies, with a clear trend towards lower efficiencies at higher angles. This effect is only noticeable in the SSD. In the start and stop MCP the efficiency dependence on the elevation angle is negligible.

4.6. Conclusion

The HIS instrument is tasked with answering some of the outstanding questions about the origin and heating of the solar wind. By providing full 3D velocity distribution functions at varying radii and inclinations the HIS instrument will provide us with unprecedented measurements of heavy ions in the solar wind. In order to provide the science team with the best possible data, the characterization of performance issue of the instrument was performed here. Additionally, the geometric factor and TOF efficiencies of the instrument were calculated through the use of SIMION simulations. These simulations showed that the energy resolution and elevation passband meet or exceed requirements that were set for the instrument. The efficiencies and geometric factor play an integral part in the creation of the final data products from the instrument. In this work we showed that there were various dependencies (E/q setting, elevation angle, azimuthal angle) on both the geometric factor and the efficiencies and that it will be important to fully characterize the instrument before launch. The work done in this chapter will provide the ground work for the final calibration of the instrument, saving the instrument team time and resources by providing them with an independent calculation to compare against laboratory measurements.

4.7. Future Work

The derivation and calculation of the geometric factor and efficiencies of the HIS instrument were done with preliminary voltages settings within the instrument. During initial calibration of the instrument, the final stepping voltages for both the E/q and elevation will be determined. When those settings are determined it will be necessary to re-run the geometric factor calculation and the TOF efficiencies. Both of these parameters of the instrument are highly dependent on the voltage settings in the EA-IS. During calibration the energy passband and elevation passband of the instrument will be obtained. Comparisons to the SIMION model will be done to help determine the optimal voltage settings.

One of the major causes for a decrease in the instrument efficiency in the TOF section is the focusing of particles exiting the EA-IS. Further characterization of this focusing is necessary to accurately capture the E/q efficiencies in the TOF section. Specific knowledge on the E/q setting that results in the focusing point being pushed past the carbon foil will simplify the calibration process because once the focusing point is past the carbon foil the effects on the efficiencies are eliminated. The characterization of the efficiencies vs. E/q will be done to help support the final calibration of the instrument.

Finally, in calibration it is impractical and near impossible to test every elevation and E/q step. In order to get a realistic representation of the instrument, calibration curves have to be made using the steps that are tested. Knowledge about points in the measurement that will deviate from the normal measurement characteristics is crucial to obtaining the proper correction curves. For example, measurements around the extreme azimuth angles and around the carbon foil struts have been shown here to deviate largely from the rest of the efficiencies calculated. These point in particular will have to be examined closely in calibration. Further work is needed to identify all of the simulated efficiency curves for all of the steps in order to determine which steps need to be characterized in calibration.

CHAPTER V

Summary and Conclusions

5.1. Summary

In this thesis we have addressed two of the fundamental problems of the solar wind: (1) Where is the solar wind source region? (2) What heats and accelerates the solar wind in the corona? With heavy ion data from Ulysses SWICS at mid-latitudes in the heliosphere we first showed in Chapter 2 that all of the wind faster than 500 km s^{-1} have the same kinetic properties (ion temperature ratio, differential velocity, and entropy) and elemental abundance ratios (Fe/O), but different velocities and charge state composition. These kinetic properties tell us that all of this fast solar wind bear the same signatures of wave heating. The elemental abundance ratios indicated that all of the solar wind faster than 500 km s^{-1} originated from coronal holes, regardless of velocity or charge state ratios. This provided the continuum of charge states and velocity seen in the solar wind.

The solar wind was then analyzed using heavy ion data from ACE SWICS in Chapter 3. Here we showed that the fast solar wind ($v > 500$ km s^{-1}) observed in the ecliptic by ACE was identical to the fast solar wind seen with the Ulysses spacecraft out of the ecliptic plane. We also analyzed the slow solar wind ($V < 500$ km s^{-1}) and found that the abundances (Fe/O ratio) indicate that this wind comes from different sources: (1) The high Fe/O wind most likely originates from closed magnetic loops; and (2) the low Fe/O wind originated either from coronal holes or short lived loops. From here we separated the slow solar wind using Coulomb collisional age, which is a parameter that estimates the number of coulomb collisional timescales elapsed during the wind's journey from the Sun to our instrument. Coulomb collisions tend to thermalize the solar wind, erasing difference in temperature and velocity between the different elements in the wind. With the collisional age separation we noticed that the less collisional wind showed the same signatures of wave heating (e.g. large heavy ion to proton temperature ratios, differential velocities) as the fast solar wind regardless of its Fe/O ratio and hence origin (coronal hole or magnetic loops). The more collisional wind had these signatures of heating erased by the Coulomb collisions, as expected.

Using the results from Chapter 2 and 3 we proposed a unified wind scenario:

1. ***All of the solar wind comes from two different sources***
    a. ***Magnetic loops***
    b. ***Coronal holes***
2. ***Regardless of its release mechanism it is then heated and accelerated by waves.***

The heavy ion data used to in this analysis is the best available, but lacks the measurement cadence and velocity distribution resolution to fully pin down the heating signatures. In particular it is unable to measure the temperature anisotropy of the solar wind ($T_\perp$ and $T_\parallel$). To provide these needed measurement the next generation of heavy ion instruments is being developed. This thesis provided support for one such instrument on the Solar Orbiter spacecraft, HIS, by analyzing Monte Carlo simulations of ions flown through the new mass spectrometer. From these simulations the geometric factor of the instrument and the TOF efficiencies were calculated, deepening our understanding of the inner working of the instrument and preparing the instrument team for calibration and data product creation.

5.2. Revisiting the Guiding Science Questions

5.2.1. Is the fast solar wind seen at the poles different from the fast solar wind seen in the ecliptic?

Measurements from the Ulysses spacecraft have provided us with heavy ion data at different latitudes in the solar system. In chapter 2 we analyzed 3 fast latitude passes of the solar wind during different portions of the solar cycle. With the data from these passes we were able to see that there existed a sub-set of fast solar wind, called the boundary wind, which had similar compositional properties to the fast solar wind, but charge state ratios in between that of the fast and slow solar wind. From this data we conclude that this boundary wind originates from the edge of coronal holes where it undergoes more expansion, leading to a slower wind speed, higher electron temperatures, and higher densities than the wind coming from coronal hole centers resulting in higher ionization. The boundary wind is just an extension of the fast solar wind at slow speeds due to the location of its foot points. In chapter 3 we expanded this study to the in ecliptic measurements of the ACE spacecraft. Here we found similar trends in the compositional and kinetic data from heavy ions as seen in chapter 2. This led to the conclusion that the boundary wind was present all the way down to the ecliptic plane. The fast solar wind seen at the poles and in the ecliptic showed the same type of kinetic properties that indicate that these two winds are actually undergoing the same processes. At the poles, the majority of the fast solar wind seems to emanate from the center of coronal holes where it is allowed to obtain a faster speed. In the ecliptic this pristine fast solar wind was rarely present. Instead the fast solar wind that is observed seems to be significantly slower than its counterpart at the poles. Although the difference in speed is seen between the fast solar wind at these two inclinations, the elemental composition and kinetic properties of these fast solar wind streams are the same, indicating that they do in fact originate from the same source region. ***In the end it was concluded that the differences seen between the fast solar wind at the poles and the fast solar wind in the ecliptic were only due to where in the coronal hole the wind originated.***

5.2.2. Are there multiple, separate populations of solar wind at the speeds which we use to define the slow solar wind?

The slow solar wind is generally classified as the wind slower than 500 km s^{-1}. The origin of this slow solar wind is thought to be different from the fast solar wind and many theories exist to explain where this wind comes from. In chapter 3 we analyze the slow solar wind ($v < 500$ km s^{-1}) using heavy ion data in an attempt to answer where this solar wind originates from. We split the wind by Fe/O ratio into 3 groups: low, intermediate, and high. With the low Fe/O group we found that it had similar elemental composition and ion temperatures to the fast solar wind, only with a slower velocity and higher charge states. In Chapter 2 we found boundary wind to have the same properties as this low Fe/O slow solar wind, leading us to conclude that this low Fe/O slow wind also originates from the edge of coronal holes. The high Fe/O ratio slow solar wind could only be explained by originating on loops and released by reconnection, where it is able to

FIP fractionate to a higher degree. It was concluded that the intermediate Fe/O wind likely originated from newer formed loops where the FIP effect has not yet completed its elemental fractionation. ***In the end we provided examples of solar wind with speeds less than 500 km s^{-1} with populations from different source regions.***

5.2.3. Are the mechanisms responsible for the heating and acceleration of the fast solar wind the same as those responsible for the slow solar wind?

Investigation into the slow solar wind in Chapter 3 not only showed that the boundary wind extended to speed slower than 500 km s^{-1}, but also that this wind was likely accelerated by the same mechanism as the fast solar wind. We found that there was a presence of non-negligible differential velocity and ion temperature ratios larger than unity in all parts of the slow solar wind regardless of the value of the Fe/O ratio. These differential velocity differences and temperature ratio differences were most present in the low Fe/O ratio wind which most likely originated from either short lived loops or the edge of coronal holes. The intermediate and high Fe/O ratio wind also showed some of its population to have these signatures of wave heating even though Coulomb collisions worked to erase these signatures. In the end, when separated by collisional age, all solar wind categories regardless of their Fe/O ratio, showed signatures of wave heating when collisional age was low. ***This led us to conclude that it is likely that all of the solar wind is heated by wave heating regardless of origin and that the signature of heating in the slow wind are erased by Coulomb collisions.***

References

Alfvén, H. (1950), Cosmic Electrodynamics, Oxford, Clarendon Press.

Allegrini, F., Ebert, R. W., Fuselier, S. A., Nicolaou, G., Bedworth, P., Sinton, S., Trattner, K. J. (2014), Charge State of 1 to 50 Kev Ions after Passing Through Praphene and Ultrathin Carbon Foils, SPIE, 53, 024101

Antichos, S. K., DeVore, C. R., Karpen, J. T., & Mikic Z. (2007), Structure and Dynamics of the Sun's Open Magnetic Field, The Astrophysical Journal, 671, 936-946

Antiochos, S. K., Mikic, Z., Titov, V. S., Lionello, R., & Linker, J. A. (2011), A Model for the Sources of the Slow Solar Wind, The Astrophysical Journal, 731, 112-123

Asplund, M., Grevesse, N., Sauval, A. J. & Scott, P. (2009), The Chemical Composition of the Sun, Annu. Rev. Astron. Astrophys., 47, 481-522

Axford, W. I. & McKenzie, J. F. (1992), The origin of high speed solar wind streams, Solar Wind Seven Colloquium, ed. E. Marsch & R. Schwenn (New York: Pergamon), 1

Balogh, A., Beck, T. J., Forsyth, R. J., et al. (1992), The Magnetic Field Investigations on the Ulysses Mission: Instrumentation and Preliminary Scientific Results, Astron. Astrophys. Suppl. Ser., 92, 221-236

Bame, S. J., McComas, D. J., Barraclough, B. L., et al. (1992), The Ulysses Solar Wind Plasma Experiment, Astron. Astrophys. Suppl. Ser., 92, 237-265

Belcher, J. W. & Davis, L. J. (1971), Large-amplitude Alfvén waves in the interplanetary medium, 2, Journal of Geophysical Research 76, 3534

Cranmer, S. R., van Ballegooijen, A. A., & Edgar, R. J. (2007), Self-consistent Coronal Heating and Solar Wind Acceleration from Anisotropic Magnetohydrodynamic Turbulence, The Astrophysical Journal Supplement Series, 171, 520

Berger, L., Wimmer-Schweingruber, R. F., Gloeckler, G. (2011), Systematic Measurements of Ion-Proton Differential Streaming in the Solar Wind, Physical Review Letters, 106, 151103

Biermann, L. (1951), Komentenschweife und solar Korpuskularstrahlung, Zeitschrift für Astrophysik, 29, 274-286

Burlaga, L. F. (1974), Interplanetary stream interfaces, Journal of Geophysical Research, 79, 3717

Burlaga, L. F., Mish, W. H., & Whang, Y. C. (1990), Coalescence of recurrent streams of different sizes and amplitudes, Journal of Geophysical Research, 95, 4247

Burton, M. E., Neugebauer, M., Crooker, N. U., von Steiger, R., & Smith, E. J. (1999), Identification of trailing edge solar wind stream interfaces: A comparison of Ulysses plasma and composition measurements, Journal of Geophysical Research, 104, 9925

Chandran, B.D.G, Verscharen, D., Quataert, E., Kasper, J. C., Isenberg, P. A., Bourouaine, S. (2013), Stochastic Heating, Differential Flow, and the Alpha-to-proton Temperature Ratio in the Solar Wind, The Astrophysical Journal, 776, 45

Chandran, B. D. G. (2010), Alfvén-wave Turbulence and Perpendicular Ion Temperatures in Coronal Hole, The Astrophysical Journal, 720, 548

Chapman, S. (1957), Notes on the Solar Corona and the Terrestrial Ionosphere, Smithsonian Contribution to Astrophysics, 2, 1

Collinson, G. A., et al. (2012), The geometric factor of electrostatic plasma analyzers: A case study from the Fast Plasma Investigation for the Magnetospheric Multiscale mission, Review of Scientific Insruments, 83, 033303

Cranmer (2000), Ion Cyclotron Wave Dissipation in the Solar Corona: The Summed Effect of More than 2000 Ion Species, The Astrophysical Journal, 532, 1197

Cranmer, S. R. (2010), An Efficient Approximation of the Coronal Heating Rate for use in Global Sun-Heliosphere Simulation, The Astrophysical Journal, 710, 676

Cranmer, S. R., Field, G. B., & Kohl, J. L. (1999), Spectroscopic Constraints on Models of Ion Cyclotron Resonance Heating in the Polar Solar Corona and High-Speed Solar Win, The Astrophysical Journal, 518, 937

Cranmer, S. R., Panasyuk, A. V., & Kohl, J. L. (2008), Improved Constraints on the Preferential Heating and Acceleration of Oxygen Ions in the Extended Solar Corona , The Astrophysical Journal, 678, 1480

Cranmer, S.R. et al., (2007), Self-consistent Coronal Heating and Solar Wind Acceleration from Anisotropic Magnetohydrodynamic Turbulence, The Astrophysical Journal, 171, 520.

Crooker, N. U. & McPherron, R. L. (2012), Coincidence of composition and speed boundaries of the slow solar wind, Journal of Geophysical Research, 117, A09104

Crooker, N. U., Gosling, J. T., & Kahler, S. W. (2002), Reducing heliospheric magnetic flux from coronal mass ejections without disconnection, Journal of Geophysical Research, 107, 1028

Ebert, R. W., McComas, D. J., Elliott, H. A., Forsyth, R. J., & Gosling, J. T. (2009), Bulk properties of the slow and fast solar wind and interplanetary coronal mass ejections measured by Ulysses: Three polar orbits of observations, Journal of Geophysical Research, 114, A01109

Endeve, E., Holtzer, T. E., Leer, E. (2004), Helmet Streamers Gone Unstable: Two-Fluid Magnetohydrodynamic Models of the Solar Corona, The Astrophysical Journal, 603, 307

Feldman, U. (1992), Elemental Abundances in the Upper Solar Atmosphere, Physica Scripta, 46,202-220

Feldman, U., & Laming, J. M. (2000), Element Abundances in the Upper Atmospheres of the Sun and Stars: Update of Observational Results, Physica Scripta, 61, 222

Feldman, U., Landi, E., & Schwadron, N. A. (2005), On the sources of fast and slow solar wind, Journal of Geophysical Research, 110, 7109

Fisk, L. A. and Schwadron, N. A. (2001), The Behavior of the Open Magnetic Field of the Sun, The Astrophysical Journal, 560, 425

Fisk, L. A., Schwadron, N. A., Zurbuchen, T. H. (1999), Acceleration of the fast solar wind by the emergence of new magnetic flux, Journal of Geophysical Research, 104, 19765.

Fisk, L. A., Gloeckler, G., Zurbuchen, T. H., Geiss, J., Schwadron, N. A. (2003), Acceleration of the Solar Wind as a Result of the Reconnection of Open Magnetic Flux with Coronal Loops, AIP Conf. P., 679, 287

Fisk, L. A., (1996), Motion of the footpoints of heliospheric magnetic field lines at the Sun: Implications for recurrent energetic particle events at high heliographic latitudes, Journal of Geophysical Research, 101, 15547

Fisk, L. A. (2001), On the global structure of the heliospheric magnetic field, Journal of Geophysical Research, 106, 15849

Fisk, L. A. (2003), Acceleration of the Solar Wind as a Result of the Reconnection of Open Magnetic flux with Coronal Loops, Journal of Geophysical Research, 108, 1157-1164

Geiss, J., Gloeckler, G., & von Steiger, R. (1995), Origin of the Solar Wind from Composition

Data, Space Science Review, 72, 49-60

Gloeckler, G. (1977), A versatile detector system to measure the change states, mass compositions and energy spectra of interplanetary and magnetosphere ions, 15th International Cosmic Ray Conference, 207

Gloeckler, G., Geiss, J., Balsiger, H. et al. (1992), The Solar Wind Ion Composition Spectrometer, Astron. Astrophys. Suppl. Ser., 92, 267-289

Gloeckler, G., Zurbuchen, T. H., & Geiss, J. (2003), Implications of the observed anticorrelation between solar wind speed and coronal electron temperature, Journal of Geophysical Research, 108, 1158

Gosling, J. T. (1997), Physical nature of the low-speed solar win, AIP Conf. Proc., 385, Robotic Exploration Close to the Sun: Scientific Basis, ed. S. R. Habbal (Melville, NY: AIP), 17

Gosling, J. T., Asbridge, J. R., Bame, S. J., & Feldman, W. C. (1978), Solar wind stream interfaces, Journal of Geophysical Research , 83, 1401

Grevesse, N. & Sauval, A. J. 1998, Solar Composition and Its Evolution—From Core to Corona, ed. C. Fröhlich, M. C. E. Huber, S. K. Solanki, & R. von Steiger (Dordrecht: Kluwer), 161 Hernandez, R., & Marsch, E. 1985, Journal of Geophysical Research, 90, 11062

Hollweg, J. V. (1986), Transition region, corona, and solar wind in coronal hole, Journal of Geophysical Research, 91, 4111

Hundhausen A. J., Gilbert H. E. and Bame S. J. (1968), The State of Ionization of Oxygen in the Solar Wind, The Astrophysical Journal, 152, 3

Dahl, D. A. (2000), SIMION 3D Version 7.0 User's Manual, Idaho National Engineering and Environmental Laboratory, Idaho Falls, ID.

Isenberg, P. A. & Hollweg, J. V. (1983), On the preferential acceleration and heating of solar wind heavy ions, Journal of Geophysical Research, 88, 3923

Jian L., Russell C. T., Luhmann J. G., & Skoug R. M. (2006), Properties of Stream Interactions at One AU During 1995 2004, Solar Physics, 239, 337

Kasper, J.C., Stevens, M.L., Korreck, K.E., et al. (2012), Evolution of the Relationships between Helium Abundance, Minor Ion Charge State, and Solar Wind Speed over the Solar Cycle, The Astrophysical Journal, 745, 162

Kasper, J. C., Bennett, M. A., Stevens, M. L., & Zaslavsky, A. (2013), Sensitive Test for Ion-Cyclotron Resonant Heating in the Solar Wind, Physical Review Letters, 110, 1102

Kasper, J. C., Lazarus, A. J., & Gary, S. P. (2008), Hot Solar-Wind Helium: Direct Evidence for Local Heating by Alfvén-Cyclotron Dissipation, Physical Review Letters, 101, 1103

Khabibrakhmanov, I. K., & Mullan, D. J. (1994), Gravitational damping of Alfven waves in stellar atmospheres and wind, The Astrophysical Journal, 430, 814

Ko, Y-K., Fisk, L. A., Geiss, J., Gloeckler, G., & Guhathakurta, M. (1997), An Empirical Study of the Electron Temperature and Heavy Ion Velocities in the South Polar Coronal Hole, Sol. Phys., 171, 345-361

Krieger, A. S., Timothy, A. F., & Roelof, E. C. (1973), A Coronal Hole and Its Identification as the Source of a High Velocity Solar Wind Stream, Solar Physics, 29, 505-525

Laming, J. M. (2012), Non-WKB Models of the First Ionization Potential Effect: the Role of Slow Mode Waves, The Astrophysical Journal, 744, 115-128

Laming, J. M., & Feldman, U. 2003, The Variability of the Solar Coronal Helium Abundance: Polar Coronal Holes Compared to the Quiet Sun, The Astrophysical Journal, 591, 1257

Lang, K. R. (2006), Sun, Earth and Sky, (New York: Springer Science)

Landi, E., Alexander, R. L., Gruesbeck, J. A., et al. (2012), Carbon Ionization States as a Diagnostic of the Solar Wind, The Astrophysical Journal, 744, 100-110

Lemaire, J. & Scherer, M. (1971), Kinetic models of the solar wind, Journal of Geophysical Research, 76, 7479

Lemaire, J., & Scherer, M. (1973), Kinetic models of the solar and polar winds, Rev. Geophys. Space Phys., 11, 427

Lepri, S. T., Landi, E., & Zurbuchen, T. H. (2013), Solar Wind Heavy Ions over Solar Cycle 23: ACE/SWICS Measurements, The Astrophysical Journal, 768, 94

Leroy, B. (1980), Propagation of waves in an atmosphere in the presence of a magnetic field. II - The reflection of Alfven waves , Astronomy and Astrophysics, 91, 136

Marsch, E. 1991, Physics of the Inner Heliosphere, vol. II: Particles, Waves and Turbulence, ed. by R. Schwenn, E. Marsch (Springer, Berlin, 1991), pp. 45–133

Marsch, E., Mühlhäuser, K.-H., & Rosenbauer, H. et al. (1982a), Solar wind helium ions - Observations of the HELIOS solar probes between 0.3 and 1 AU, Journal of Geophysical Research, 87, 35

Marsch, E., Mühlhäuser, K.-H., & Schwenn, R. et al. (1982b), Solar wind protons - Three-dimensional velocity distributions and derived plasma parameters measured between 0.3 and 1 AU, Journal of Geophysical Research, 87, 52

Maruca, B. A., Kasper, J. C., & Bale, S. D. (2011), What Are the Relative Roles of Heating and Cooling in Generating Solar Wind Temperature Anisotropies?, Physical Review Letters, 107, 1101

Matthaeus, W. H., Zank, G. P., Oughton, S., Mullan, D. J., & Dmitruk, P. (1999), Coronal Heating by Magnetohydrodynamic Turbulence Driven by Reflected Low-Frequency Waves, The Astrophysical Journal, 523, L93

McComas, D.J., F. Allegrini, C.J. Pollock, H.O. Funsten, S. Ritzau, and G. Gloeckler (2004), Ultrathin (10 nm) carbon foils in space instrumentation, Rev. Sci. Instrum., 75, 4863.

McComas, D. J., Elliott, H. A., Schwadron, N. A., et al. (2003), The Three-Dimensional Solar Wind

Around Solar Maximum, Geophysical Research Letters, 30, 1517-1520

McKenzie, Banaszkiewicz, and Axford (1995), Acceleration of the high speed solar wind, Astronomy and Astrophysics, 303, 45

Mikic, Z., Linker, J.A., Schnack, D.D., Lionello, R., Tarditi A. (1999), Magnetohydrodynamic modeling of the global solar corona, Physics of Plasmas, 6, 2217.

Neugebauer, M. & Snyder, C. W. (1962), Solar Plasma Experiment, Science, 138, 1095

Neugebauer, M., Goldstein, B. E., Smith, E. J., & Feldman, W. C. (1996), Ulysses observations of differential alpha-proton streaming in the solar wind, Journal of Geophysical Research, 101, 17047

Noci, G. (1973), Energy Budget in Coronal Hole, Solar Physics, 28, 403

Oran, R., Landi, E., van der Holst, B., et al. (2015), A Steady-state Picture of Solar Wind Acceleration and Charge State Composition Derived from Global Wave-Driven MHD Model, The Astrophysical Journal, 806, 55

Pagel, A. C., Crooker, N. U., Zurbuchen, T. H., & Gosling, J. T. (2004), Correlation of solar wind entropy and oxygen ion charge state ratio, Journal of Geophysical Research, 109, A01113

Parker, E. N. (1958), Dynamics of the Interplanetary Gas and Magnetic Fields, The Astrophysical Journal, 128, 664-676

Parker, E. N. (1992), The X ray corona, the coronal hole, and the heliosphere, J. Journal of Geophysical Research, 97, 4311

Parker, E. N. (2010), Kinetic and Hydrodynamic Representations of Coronal Expansion and The Solar Wind, Twelfth International Solar Wind Conference, ed. M. Maksimovic et al. (New York, NY: AIP Publishing), 1216, 3

Rappazzo, A.F., Velli, M., Einaudi, G., Dahlburg, R.B., (2005), Diamagnetic and Expansion Effects on the Observable Properties of the Slow Solar Wind in a Coronal Streamer, The Astrophysical Journal, 633, 474.

Richardson I. G. and Cane H. V. (2010), Near-Earth Interplanetary Coronal Mass Ejections During Solar Cycle 23 (1996 - 2009): Catalog and Summary of Properties, Solar Physics, 264, 189

Schwenn, R. 1990, Physics of the Inner Heliosphere, vol. I: Large-Scale Phenomena, ed. by R. Schwenn, E. Marsch (Springer, Berlin, 1990), pp. 99

Schwenn, R. (2006), Solar Wind Sources and Their Variations Over the Solar Cycle, Space Science Reviews, 124, 51

Shearer P., von Steiger R., Raines J. M., et al. (2014), The Solar Wind Neon Abundance Observed with ACE/SWICS and Ulysses/SWICS, The Astrophysical Journal, 789, 60

Siscoe, G. L. & Intriligator, D. (1993), Three views of two giant streams: Aligned observations at 1 AU, 4.6 AU, and 5.9 AU, Geophysical Research Letters, 20, 2267

Snyder, C.W. and Neugebauer M. (1962), The mission for Mariner II: Preliminary observations, solar plasma experiment, Science, 138, 1095.

Stakhiv, M., Landi, E., Lepri, S. T., Oran, R., & Zurbuchen, T. H. (2015), On the Origin of Mid-Latitude Fast Wind: Challenging the Two-State Solar Wind Paradigm, The Astrophysical Journal, 801, 100-107

Stakhiv, M., Lepri, S.T., Landi, E., Tracy, P., Zurbuchen, T.H. (2016), On Solar Wind Origin and Acceleration: Measurements from ACE, The Astrophysical Journal, 829, 117

Suess, S. T., Wang, A.-H., & Wu, S. T. (1996), Volumetric Heating in Coronal Streamers, Journal of Geophysical Research, 101, 19,957-19,966

Totten, T. L., Freeman, J. W., & Arya, S. (1995), An empirical determination of the polytropic index for the free-streaming solar wind using HELIOS 1 data, Journal of Geophysical Research, 100, 13

Tracy, P., Zurbuchen, T. H., Kasper, J. C., et al. (2015), Thermalization of Heavy Ions in the Solar Wind by Coulomb Collisions, The Astrophysical Journal, 812, 170

van der Holst, B., Sokolov, I. V., Meng, X., et al. (2014), Alfven Wave Solar Model (AWSoM): Coronal Heating, The Astrophysical Journal, 782, 81

Vauclair, S. & Meyer, J. P. (1985), Diffusion in the Chromosphere, and the Composition of the Solar Corona and Energetic Particles, 19th Intern. Comic Ray Conf., 4, 233-236

Velli, M., Grappin, R., & Mangeney, A. (1989), Turbulent cascade of incompressible unidirectional Alfven waves in the interplanetary medium, Solar Physics, 63, 1807

von Steiger, R. & Geiss, J. (1989), Supply of Fractionated Gases to the Corona, Astron. Astrophys., 225, 222-238 von Steiger, R., Geiss, J., & Gloeckler, G. (1997), Composition of the Solar Wind, in Cosmic Winds and the Heliosphere, ed. J. R. Jokipii, C. P. Sonett, & M. S. Giampapa (Tucson, AZ: Univ. Ariz. Press), 581-616

von Steiger, R., Schwadron, N. A., Fisk, L. A., et al. (2000), Composition of Quasi-Stationary Solar Wind Flows from Ulysses/Solar Wind Ion Composition Spectrometer, Journal of Geophysical Research, 105, 27,217-27,238

von Steiger, R. & Zurbuchen, T. H. (2006), Kinetic properties of heavy solar wind ions from Ulysses-SWICS, Geophysical Research Letters, 33, L09103

von Steiger, R., & Zurbuchen, T.H. (2016), Solar Metallicity Derived from in situ Solar Wind Composition, The Astrophysical Journal, 816, 13

Wang, Y.-M. & Sheeley, N.R. (1990), Solar wind speed and coronal flux-tube expansion, The Astrophysical Journal, 355, 726.

Wang, Y.-M. & Sheeley, N. R. (1991), Why Fast Solar Wind Originates from Slowly Expanding Coronal Flux Tubes, The Astrophysical Journal, 372, L45-L48

Wang, Y.-M. & Sheeley N.R., (1992), On potential field models of the solar corona, The Astrophysical Journal, 392, 310.

Wang, Y.-M., Sheeley, N. R., Walters, J. H., et al. (1998), Origin of Streamer Material in the Outer Corona, The Astrophysical Journal, 498, L165-L168

Wang, Y.-M., & Sheeley, N. R. (2006), Sources of the Solar Wind at Ulysses during 1990-2006, The Astrophysical Journal, 653, 708

Wang, Y.-M., Ko, Y.-K., & Grappin, R. (2009), Slow Solar Wind from Open Regions with Strong Low-Coronal Heating, The Astrophysical Journal, 691, 760

Weberg, M. J., Lepri, S. T., & Zurbuchen, T. H. (2015), Coronal Sources, Elemental Fractionation, and Release Mechanisms of Heavy Ion Dropouts in the Solar Wind, The Astrophysical Journal, 801, 99-107

Weberg, M. J., Zurbuchen, T. H., & Lepri, S. T. (2012), ACE/SWICS Observations of Heavy Ion Dropouts within the Solar Wind, The Astrophysical Journal, 760, 30-37

Widing, K. G. & Feldman, U. (2001), On the Rate of Abundance Modifications versus Time in Active Region Plasmas, The Astrophysical Journal, 555, 426

Wuest, M., Evans, D.S., von Steiger, R. (2007), Calibration of Particle Instruments in Space Physic, Published for the International Space Science Institute by ESA Communications, Noordwijk, The Netherlands.

Zurbuchen, T. H. & von Steiger, R. (2006), On the Solar Wind Elemental Composition: Constraints on the Origin of the Solar Wind, in SOHO-17. 10 Years of SOHO and Beyond, Proceedings of the conference, ed. H. Lacoste and L. Ouwehand, 617

Zurbuchen, T. H., & Richardson, I. G. (2006), In-Situ Solar Wind and Magnetic Field Signatures of Interplanetary Coronal Mass Ejections, Space Science Reviews, 123, 31

Zurbuchen, T. H., (2007), A New View of the Coupling of the Sun and the Heliospher, Annual Review of Astronomy & Astrophysics, 45, 297

Zurbuchen, T. H., Fisk, L. A., Gloeckler, G., & von Steiger, R. (2002), The solar wind composition throughout the solar cycle: A continuum of dynamic state, Geophysical Research Letters, 29, 1352